"Theorists conduct experiments with their brains. Experimenters have to use their hands, too. Theorists are thinkers, experimenters are craftsmen. The theorist needs no accomplice. The experimenter has to muster graduate students, cajole machinists, flatter lab assistants. The theorist operates in a pristine place free of noise, of vibration, of dirt. The experimenter develops an intimacy with matter as a sculptor does with clay, battling it, shaping it, and engaging it. The theorist invents his companions, as a naive Romeo imagined his ideal Juliet. The experimenter's lovers sweat, complain, and fart."

James Gleick, 1987, "Chaos"

University of Alberta

Wind Climate in Yukon Mountainous Terrain

By

Jean-Paul Pinard

A thesis submitted to the Faculty of Graduate Studies and Research in partial fulfillment of the requirements for the degree of Doctor of Philosophy

Department of Earth and Atmospheric Sciences

Edmonton, Alberta

Fall 2008

University of Alberta

Faculty of Graduate Studies and Research

The undersigned certify that they have read, and recommend to the Faculty of Graduate Studies and Research for acceptance, a thesis entitled WIND CLIMATE IN YUKON MOUNTAINOUS TERRAIN submitted by Jean-Paul Pinard in partial fulfillment of the requirements for the degree of Doctor of Philosophy.

John D. Wilson

Gerhard W. Reuter

Bruce R. Sutherland

Christian Masson

Peter M. Steffler

Gordon E. Swaters

This day 8 September 2008

Dedication

To Sally,

for showing me the way,

and true love.

Abstract

To quantify its wind energy potential the wind climate of the mountainous Yukon has been examined through data analysis and numerical modelling. Using many surface climate stations and radiosondes it was determined that the region's atmosphere is generally stably stratified, causing air to flow horizontally around mountain obstacles.

The mesoscale model MC2, a non-hydrostatic and compressible model, has been used to simulate the mean wind climate of the steep mountainous Yukon with the intent to produce a reliable wind energy map. Early results of full scale simulations initialized with the standard NCEP/NCAR Reanalysis provided erroneous results for wind speeds and directions when compared to measurements.

A detailed assessment of the mountainous Whitehorse Area climate provided insight into the expected flow behavior that MC2 should attain. It was clear that the atmosphere is generally stably stratified, valley inversions are common, and that the upper-level winds are often de-coupled from the valley winds. It was also found that downward momentum transfer and horizontal pressure gradients play important and varying roles that are dependent on the atmospheric stratification and valley orientation.

With the new findings the Whitehorse area was simulated, again with MC2, but using simplified boundary conditions to compare the traditional method of running MC2 with an improved one. It was shown that the method by which the Reanalysis is used produces problematic pressure gradient directions in weak stratification. The modified input climate state attempts to correct this problem without modifying the present internal settings of MC2. It was found that in MC2 the horizontal

pressure gradient terms provide the proper forcings to move air within deep valleys. However, MC2 in its present form produces excessively strong winds on lee slopes, contrary to measurements made in the Whitehorse Valley.

The MC2 model may be improved by implementing a z-coordinate system, and redefining the Reanalysis inputs, particularly those sections of the input that are below the mountaintops of the model domain. With these improvements the MC2 model should be further tested to determine whether it is reliable tool for wind energy assessment in steep mountainous terrain.

Preface

About a year into this degree work I met Dr Robert Benoit at a conference held by the Canadian Wind Energy Association (CanWEA). Dr Benoit, who was the head of RPN (Recherche en Prévision Numérique) in Dorval, had been leading the development of the Mesoscale Compressible Community model, MC2. This is a Canadian-made model that has been the foundation of the Canadian Wind Atlas. Dr Benoit's group knew that the model had some problems in the mountains of BC and Yukon but they had not yet found the resources to test and improve the model in this area. At the same time I was investigating a number of models (RAMS, ARPS, MSFD, MS-Micro) for their suitability in the mountainous terrain of Yukon. Dr Benoit invited me to participate in their effort to test *their* model in mountainous terrain. Since both RPN and I had the same goal of mapping the wind climate of Yukon, this became the focus of my thesis.

Acknowledgements

A portion of the data used in this study is owned by and copyrighted to Yukon Energy and the Yukon Development Corporation. Permission has been granted by both aforementioned owners to use these data to carry out the comparative study.

I would like to acknowledge the following: John D. Wilson, my supervisor at the University of Alberta; my supervisory and the examination committee for reviewing this document and providing insightful comments; Robert Benoit and the group RPN; the Natural Sciences and Engineering Research Council (NSERC); Environment Canada for scholarship funding towards this study and for publicly available wind climate data; the Northern Scientific Training Program (NSTP), and the Canadian Circumpolar Institute (CCI) for scholarship funding; Yukon Government (Yukon Development Corporation, Yukon Energy, Energy Solutions Centre, Community Services, and Wildland Fire Management) for the surface wind data and the research opportunities; the National Oceanic and Atmospheric Administration/National Center for Atmospheric Research Reanalysis (NCEP/NCAR), and RAOBS data center;

I would also like to Acknowledge: John F. Maissan, Leading Edge Inc., cham-

pion of the Haeckel Hill wind project and colleague; William Miller at Environment Canada, Whitehorse for all of his help with the airport station wind data; Don Green meteorologist at Community Service, Yukon Government; Michael Purves, retired meteorologist in Whitehorse; David Craig, Joan Craig, and Jack Cable with the Boreal Alternative Energy Centre; Herbert Wahl, a Yukon meteorologist who passed away recently.

This whole study is dedicated to the memory of my mentor, Doug B. Craig, my inspiring and pioneering wind prospector of the Yukon.

Contents

1 Introduction **1**

1.1 Historical overview of wind power 2

1.2 Wind prospecting in Yukon 3

1.3 Mapping the wind in Canada 5

1.4 Goals of the wind research in Yukon 6

1.5 Road map to the Thesis 6

2 Climate Data **11**

2.1 Measuring the wind 12

2.2 Wind climate stations in Yukon 13

2.3 Types of instruments and equipment 20

2.4 Measurement errors 28

a Sensors 28

b Placement of sensors 30

2.5 Data analysis and climate estimates 32

2.6 Projecting measured winds to other heights 35

3 Mountain wind climate **40**

3.1 General atmospheric circulation and the Western Cordillera 41

3.2 Mountain wind climates under stable stratification 46

3.3 Orographically enhanced flows 53

4 Modeling the wind climate **61**

4.1 Basic conservation principles in mesoscale flows 62

a Equations of motion under Boussinesq approximation . . . 62

b Scale Analysis 64

c Reynolds Averaging of the Navier-Stokes Equations 66

d Applications of the Navier-Stokes and the Reynolds equations 69

4.2 The Anemoscope toolkit 71

a The NCEP/NCAR Reanalysis 72

b MC2 in the EOLE mode 74

c Earlier studies of flow on hills/mountains using MC2 78

4.3 How MC2 is used in the balance of the thesis 80

5 A WEST Wind Climate Simulation of the Mountainous Yukon **87**

5.1 Introduction 88

5.2 Orography and wind climate of the southern Yukon 90

5.3 Wind monitoring sites in the territory 92

5.4 WEST: the wind energy simulation toolkit 101

a MC2 102

b MS-Micro 105

5.5 Inputs and settings for the southern Yukon simulation 106
a The MC2 input climate data 106
b MC2 input climate data versus Whitehorse and Yakutat radiosonde data 110
c The surface data 116
d The grid set-up and simulations 124
5.6 Results 125
5.7 Discussion 132
5.8 Conclusions 137

6 Wind Climate of the Whitehorse Area 145

6.1 Introduction 146
6.2 The monitoring stations 151
6.3 Upper-air time series and surface correlations 156
6.4 Climatological vertical profile of upper-air wind speed 160
6.5 Geostrophic wind — valley wind relationship 162
6.6 Discussion 170
6.7 Conclusions 173

7 Mesoscale wind modelling in steep mountain terrain 177

7.1 Introduction 178
7.2 AnemoScope toolkit 180
7.3 NCEP/NCAR Reanalysis extracted for driving MC2 183
7.4 Comparing Reanalysis to observations 184

7.5 Numerical simulations 193

a Climate macrostate Ω_1 194

b Climate macrostate Ω_2 201

7.6 Discussion 209

7.7 Conclusions 212

8 Discussion and Conclusions **218**

List of Figures

2.1 Map of wind climate stations in Yukon 14

2.2 Map of wind climate stations in the Whitehorse area 15

2.3 A forestry and a wind energy station 19

2.4 Wind stations in the community wind resource assessment programme 21

2.5 A three-cup anemometer and wind vane. 23

2.6 Two wind sensors at the top of a monitoring tower 25

2.7 Wind sensors under light icing 26

2.8 A severe icing event at a wind monitoring station 27

2.9 Winching a tower into the upright position 29

3.1 Long-term annual mean geopotential height of the 700 mbar surface 44

3.2 Long-term annual mean geopotential height at sea level 45

3.3 Flow impinging on an isolated mountain 49

3.4 Air approaching a long ridge in the northern hemisphere 51

3.5 Relationship between the orientation of the overhead geostrophic wind vector and of the valley wind 52

5.1 Orographic map of Yukon 91

5.2 Map of southern Yukon showing airport and wind energy stations . . 93
5.3 Variability of different period lengths of a running average to the long-term mean for the Whitehorse airport station 98
5.4 The WEST flowchart 103
5.5 Wind energy-frequency roses for the Whitehorse upper air station and the MC2 input data 108
5.6 Same wind energy-frequency roses as in the previous figure but using Yakutat and the MC input data 109
5.7 Charts comparing MC2 input, Whitehorse, and Yakutat radiosondes 114
5.8 Vertical profile comparing input potential temperature for the WEST simulation and the Whitehorse radiosondes 115
5.9 Land use map of the southern Yukon 118
5.10 DEM used for the MC2 simulation 121
5.11 Elevation map depicting the difference between the mesoscale and the microscale DEMs 122
5.12 Graphical comparison between WEST and measurements 129
5.13 Isotach map of long-term annual mean wind speed as produced by WEST for the Kluane region 130
5.14 Wind energy-frequency roses overlain on map Kluane region 134

6.1 Map of the Whitehorse area 147
6.2 Occurrence of wind speed measurements with respect to elevation . 155
6.3 Time series of annual mean wind speed 157

6.4 Monthly mean wind speeds 158
6.5 Vertical profiles of mean wind speed and temperature 162
6.6 Whitehorse map with wind roses 164
6.7 Joint wind energy-frequency roses of winds aloft and within the Whitehorse Valley 166
6.8 Joint wind energy-frequency roses of winds aloft and within the Whitehorse Valley but limited to west-northwest winds aloft 168
6.9 Relationship between the winds aloft and winds within a valley . . . 169
6.10 Elevation profiles along lines A-B, C-D in Figure 6.6 171

7.1 Vertical profiles of temperature and wind speed 186
7.2 Wind energy-frequency roses comparing the Reanalysis and the Whitehorse radiosondes 191
7.3 Map of the south-central Yukon including Whitehorse Area 192
7.4 Outcome of wind climate simulation based on driving MC2 with climate macrostate Ω_1 197
7.5 Cross-section of potential temperature and vertical velocity across the Takhini Valley in outcome of climate macrostate Ω_1 199
7.6 Same as Figure 7.4 but for climate macrostate Ω_2. 203
7.7 Same as Figure 7.5 but for climate macrostate Ω_2 and across the Whitehorse Valley 204
7.8 Wind speed profiles in cross-section of the Whitehorse Valley 207

List of Tables

2.1 List of past and current wind climate stations in the Yukon 16

4.1 Scale analysis of the horizontal momentum equations. 65

4.2 Scale analysis of the vertical momentum equation. 66

5.1 List of wind monitoring stations used for the model comparison . . 95

5.2 Roughness classes for interpreting the land use data 117

5.3 Land use data and surface roughness 120

5.4 Comparison of mean wind speeds between the model and the field measurements 127

7.1 Comparison of the Reanalysis and radiosonde measurements in the Whitehorse area 185

7.2 List of parameters in simulations of MC2. 195

7.3 Input parameters of the climate macrostate Ω_1 196

7.4 Input parameters of the climate macrostate Ω_2 in MC2 simulation . 202

List of Symbols and Abbreviations

a	Earth's radius
A	Scale factor in the Weibull distribution
b	Buoyancy term (MC2)
f	Coriolis effect due rotating earth
F	Froude number, ratio of inertial and buoyancy forces
$F_{U,V,w}$	Eddy forcing terms in sub-grid scale processes
g	Earth's gravitational acceleration
h	Height of dividing streamline, related to Froude number
H	Height of a hill or mountain
K	Eddy viscosity
k	Turbulent kinetic energy
k_v	Von Kármán constant
k_s	Shape factor in the Weibull distribution
K_e	Pseudo kinetic energy per unit mass (MC2)
L	A length scale typically for a domain size
L_o	Obukhov (also Monin-Obukhov) length
L_h	Half-length of a hill
N	Brunt-Väisälä frequency
p	Pressure departure from reference state p_o
P	Total air pressure
p_o	Constant reference state pressure
R	Pearson correlation
R_o	Rossby Number, ratio of Coriolis and inertial timescales
r	Water-vapor mixing ratio
S	Map scale (MC2)
T	Dry air temperature
TKE	Turbulent kinetic energy
T_v	Virtual temperature
U	Horizontal wind speed
u, v, w	Wind speed in the x, y, z directions respectively
u_g	Geostrophic wind component in the east direction
u_i'	Fluctuation of velocity from the mean $\bar{u}_i$
$\bar{u}(z)$	Mean horizontal wind speed as a function of z

$\bar{u_i}$	Mean velocity ($u_i = u, v, z$, where $i = x, y, z$)
v_g	Geostrophic wind component in the north direction
W_h	Half-width of a hill
x, y, z	Lengths in coordinate system, z being up
z_0	Surface roughness length
z_m	Height at which wind speed is measured
z_p	Height at which wind speed is projected or estimated
Γ_d	Dry adiabatic lapse rate
δ_{ij}	Kronecker Delta
ν	Kinematic viscosity of air
Ω_i	A climate macrostate (i=1,2) used as input for MC2 simulation
Ω	Earth's rate of rotation
ϕ	Latitude on earth's surface
ϕ_o	Reference latitude (MC2)
ρ	Air density
ρ_o	Constant air density under Boussinesq approximation
τ_{ij}	Reynold's stress or flux of momentum ($\tau_{ij} = \rho\overline{u_i u_j}$)
θ	Departure from reference θ_o
θ_o	Reference state potential temperature
AES	Atmospheric Environment Service, now MSC (see below)
AGL	Above ground level
ASL	Above sea level
BAEC	Boreal Alternative Energy Centre, based in Yukon
C	Temperature unit of Celsius
CanWEA	Canadian Wind Energy Association
CMC	Canadian Meteorological Centre
CHC	Canadian Hydraulics Centre
CPU	Computer processor unit
CWRAP	Community Wind Resource Assessment Programme
DEM	Data elevation model
DNS	Direct numerical simulation
EC	Environment Canada
EOLE	A non-NWP model, or quasi-diagnostic mode
ESC	The Energy Solutions Centre, Government of Yukon
INAC	Indian and Northern Affairs Canada
K	Temperature unit of Kelvin (273.16 ° C)
KAMM	Karlsruhe Atmospheric Mesoscale Model
km	Kilometres a unit of length
LAM	Limited area model
LES	Large eddy simulation
LLSM	Linear least squares method
m	Metres a unit of length
m s^{-1}	Metres per second, unit of speed
MAP	Mesoscale Alpine Programme
mbar	Also mb, millibar, a unit of pressure

MC2	Mesoscale Compressible Community
MM5	Fifth-Generation NCAR/Penn State Mesoscale Model
MS-Micro	Micro-scale wind model developed by Mason and Sykes (1979)
MSC	Meteorological Service of Canada
NCAR	National Center for Atmospheric Research
NCEP	National Centers for Environmental Prediction
NOAA	The National Oceanic and Atmospheric Administration
NTS	National Topographic Systems
NWP	Numerical weather prediction, a prognostic model
PBL	Planetary boundary layer
PDF	Probability density function
RANS	Reynolds-averaged Navier-Stokes
RPN	Recherche en Prévision Numérique
SGS	Sub-grid scale
SISL	Semi-implicit and semi-Lagrangian numerical integration scheme
USGS	United States Geological Survey
WAsP	Wind Atlas Analysis and Application Programme
WEST	Wind Energy Simulating Toolkit
WPPI	Wind Power Purchase Incentive, Canadian government programme
YEC	Yukon Energy Corporation
YG	Yukon Government

Chapter 1

Introduction

1.1. Historical overview of wind power

As early as 5000 BC, wind energy was being harnessed to propel sail boats along the Nile River. By 200 BC, windmills in China were pumping water, a few centuries later vertical-axis windmills with woven reed sails were grinding grain in Persia and the Middle East. Wind technology spread to Europe where by the 14th century the Dutch refined the windmill, and used it to drain lakes and marshes in the Rhine River Delta. In rural North America in the early 1800's wind turbines produced electricity, and this continued until the 1930's when extension of the electric power grid provided a cost-effective alternative to isolated generators. The oil embargoes of the 1970's, the rising price of fossil fuels, and progressive government regulations spawned the establishment of about 1.5 GW of wind farms in California.

In 1994, the first Canadian commercial wind farm was built at Cowley Ridge, near Pincher Creek (Alberta), with 52 turbines totalling 19 MW of capacity. With concern over climate change and the encouragement of the Canadian Wind Energy Association (CanWEA), in 2002 the federal government introduced the Wind Power Production Incentive (WPPI) program, providing a boost to the Canadian wind industry. At the time of writing, Canada's current installed capacity is 1.6 GW – sufficient to power over 500,000 homes – and it continues to grow.

In the Yukon two commercial scale wind turbines were installed, respectively in 1992 and 2000, as working experiments. These were rated at 150 and 660 kW respectively, and have been producing energy for 150 homes annually. From their inception these turbines have been connected to the territory's isolated hydro-electric

grid: the increased winter mountaintop winds coincide with peak energy demand periods of the winter months, thus potentially eliminating the need to run diesel generators. Electrical demand in the Yukon is steadily growing, and because of the limited availability of hydro-power and the increasing economic cost of diesel-electric generation, wind energy is becoming a viable complement to the existing hydro grid.

1.2. Wind prospecting in Yukon

Wind prospectors, like their mining counterparts, explore the countryside looking for new potential wind energy sites to develop. These prospectors often pour over contour maps and sift through wind data, looking for the mother lode of windy sites. When an area looks interesting the prospector visits the sites, usually by all-wheel-drive vehicle though sometimes on foot. In mountainous terrain there are typically very few roads to access the hills and mountaintops, and these visits require a long hike, or more expensively, a flight by helicopter. Because of this difficulty of access it becomes more expensive to explore wind energy potential in mountainous terrain. However it is generally known that the mountaintops are windier than alternative sites, so of necessity they must be explored.

By the 1980's the geological prospector Dr. Doug Craig had a suspicion from his many years of fieldwork that the mountaintops of the Yukon were perhaps windy enough for wind energy production, for he had observed that typically it was windier on the mountaintops than at lower elevations. At the time little was

known (officially and instrumentally) about mountain wind climate in Yukon (Wahl et al. 1987; Pinard 2005), because all available surface measurements were in valley bottoms. There was the Whitehorse weather balloon data however, and after analyzing those measurements (Craig and Craig 1990) the researcher-geologist was convinced that indeed the mountaintops must be windy enough for wind energy development. Leading a team of enthusiasts, he began installing wind monitoring stations on mountaintops near Whitehorse (Craig and Craig 1991, 1992, 1994, 1995, 1996) in the hope of finding a useable prototype site for the economic extraction of wind energy.

This initial wind monitoring effort inspired the territorial government to a decade long program to install more observation stations in other parts of the territory (Baker 1995). They encountered a few problems along the way, one of which was an unfortunate placement of stations in orographically sheltered areas. Another problem was winter icing of the anemometers (Maissan 2001), which hampered attempts to measure the winds properly during the winter. It was becoming apparent over the course of the observation programme that, along with the need to understand mountain meteorology as best as can be hoped, numerical modeling would be a required tool and that creating a wind map of the Yukon would greatly aid in the exploration of new wind sites.

1.3. Mapping the wind in Canada

In 2000 (the year I began this Ph.D.) the Canadian Wind Atlas (windatlas.ca) was introduced to the public domain. The atlas provides a 5 km resolution wind energy map for the country, which includes the Yukon Territory. It is known (Dr. Robert Benoit, pers. comm.) that the atlas has some weaknesses in the Western Cordillera. However, since the publication of Pinard et al. (2005) in Chapter 3 some improvements have been made to the methodology of the wind atlas.

There are presently higher resolution wind energy climate maps for Quebec, Ontario, British Columbia, Prince Edward Island, New Brunswick, and Nova Scotia. Yukon's southern neighbour, British Columbia, undertook to map the wind over its mountainous region (see BC Hydro's website, search for "BC wind map") at 1- km resolution, an activity achieved in 2000 by TrueWind Solutions. There have been no publications (known to this author) addressing the map's accuracy, however Delphi (2006) reports that the mean annual wind speed predictions from the mapping study are accurate to within approximately 10%. This is compared to 10% for the Canadian Wind Atlas which also covers BC but at a 5-km resolution.

Currently according to Delphi some of the leading sources of errors in the modern wind mapping methodologies include coarse (inadequate) grid resolution, uncertainty in land cover and surface roughness, sparse meteorological observations (in some regions), and the difficulty of simulating atmospheric flow in the conditions of strongly stable stratification that are common in the continental lower boundary layer during winter at high latitudes. The last point is the most interesting

one, it will become clear to the reader of this thesis that atmospheric stability plays a central roles in mountain wind climates.

1.4. Goals of the wind research in Yukon

The primary goal in my wind research is to map the Yukon's wind energy potential. Specifically, I seek to answer two key questions:

1. What can we learn of the Yukon wind climate through existing measurements and other studies of mountain wind climate? And,

2. How can numerical modelling aid in mapping the wind climate of mountainous terrain?

In particular, this thesis is about testing the capability of the mesoscale model MC2, by the criterion of high quality wind observations in the mountainous terrain of the southern Yukon.

1.5. Road map to the Thesis

This thesis follows a mixed paper format. Chapters 2 to 4 provide background material while Chapters 5 to 7 are stand-alone papers that were either published (Ch. 5 and 6) or submitted for publication (Ch. 7). The thesis concludes with chapter 8.

Chapter 2 lists all the known wind climate stations in Yukon, most of which are used in this thesis. A description is given of the instruments, the method of

measurement, and the errors that are associated with the measurements. This chapter also describes how the measured winds are analyzed and how the mean wind fields are estimated: projected to long-term means and to higher elevations above the ground.

Chapter 3 gives an overview of the general atmospheric circulation in northwest North America, mountain wind climates in statically stable environments, and orographically enhanced wind flows. Chapter 4 reviews the basic conservation principles in atmospheric flows. This chapter also describes how these principles are adapted to mesoscale flows using the Boussinesq approximation, scale analysis, and Reynolds averaging. A discussion ensues on how these principles are applied to numerical modelling of flows over complex terrain and how they are used in MC2. Chapter 4 ends with a synopsis of the next three chapters, which are briefly outlined here.

The next three paper-style chapters are placed chronologically. They include all of the text from the originally published (or submitted) papers, except that the abstracts and the acknowledgements have been removed. A more detailed synopsis of chapters 5 to 7 is given in section 4.3. Chapter 5 (Pinard et al. 2005) is a comparison of field measurements to a numerical simulation of the southern Yukon's wind climate using the standard settings in the WEST (now Anemoscope, see section 5.4 and 7.2) toolkit. This comparative study brought to light the need to understand the importance of atmospheric stratification and the forcing mechanisms on mountains and valley winds. Chapter 6 (Pinard 2007) attempts to answer this by analysing upper-air and surface measurements in the mountainous Whitehorse area. With the

new findings on the Whitehorse area's mountain wind climate, chapter 7 (submitted: Pinard 2008) presents a simpler, more controlled and focused MC2 wind climate simulation of the Whitehorse area. Chapter 8 summarizes the most important findings of chapters 5 to 7 in the attempt to answer the key questions of the previous section and recaps the next steps in improving the MC2 model for mountain wind climate simulations.

Bibliography

Baker, D. R., 1995: Annual report wind monitoring and analysis. Technical report, Nor'wester Energy Systems Ltd., prepared for the Yukon Energy Corporation, Box 5920, Whitehorse, Yukon, Y1A 6S7, 350 pp.

Craig, D. and D. Craig: 1994, Monitoring of icing events on fjells in Northern Canada. *BOREAS II*, 76–82.

Craig, D. B. and D. F. Craig, 1991: Wind energy potential, report no 2. Technical report, Boreal Alternate Energy Centre, Whitehorse, Yukon.

Craig, D. F. and D. B. Craig, 1990: Wind energy potential. Technical report, Boreal Alternate Energy Centre, Whitehorse, Yukon.

— 1992: Wind energy potential: Estimate of energy production from wind monitoring stations on Haeckel Hill and Mount Sumanik, report no. Technical report, Boreal Alternate Energy Centre, Whitehorse, Yukon.

— 1995: Wind energy potential, investigation of icing events on Haeckel Hill, report #4. Technical report, Boreal Alternate Energy Centre, Whitehorse, Yukon.

Craig, D. F. and D. B. Craig: 1996, Wind energy potential, investigation of icing events on Haeckel Hill, report #4. *BOREAS III*, Whitehorse, Yukon, 169–193.

Delphi, 2006: Reviewing gaps in resource mapping for renewable energy for North America. Technical report, The Commission for Environmental Cooperation, prepared by the The Delphi Group with the Instituto de Investigaciones Electricas (IIE).

Maissan, J. F., 2001: Wind power development in sub-Arctic conditions with severe rime icing. *The Northern Review*, **24**, 174–183.

Pinard, J. D. J.-P., R. Benoit, and W. Yu, 2005: A WEST wind climate simulation of the mountainous Yukon. *Atmosphere-Ocean*, **43**, 259–282.

Pinard, J.-P.: 2005, Wind climate of the mountainous Yukon. *New Northern Lights: Graduate Research on Circumpolar Studies from the University of Alberta*, Canadian Circumpolar Institute.

Pinard, J.-P., 2007: Wind climate of the Whitehorse Area. *Arctic*, **60**, 227–237.

— 2008: Mesoscale wind modelling in steep mountain terrain. *Atmosphere-Ocean*, to be published.

Wahl, H. E., D. B. Fraser, R. C. Harvey, and J. B. Maxwell, 1987: Climate of Yukon. Technical report, Environment Canada, Ottawa.

Chapter 2

Climate Data

2.1. Measuring the wind

The first step in understanding the wind climate is to measure it. In an anecdotal fashion, we feel the wind as we hike along a ridge top, we stop, symbolically lick an index finger and point it upward to scope its speed and direction. We also look around us for clues from nature. If there is a dominant direction in a strong mean wind the trees growing in this environment will sometimes develop an asymmetrical shape with smaller bent branches on the windward side. Sand or snow blasting will also smoothen the surface of bark and rocks providing further evidence. We interview locals who at times respond with "Oh it always blows here, lots of wind energy!". People are often aware when it is windy, particularly on a cold stormy winter day, but the calm periods often go unnoticed. However difficult it is to judge the wind potential from this kind of anecdotal information, a good indicator of promising wind potential is the intensity with which locals *complain* about the wind.

The wind climate is measured for several reasons. The amateur weather enthusiast often uses an inexpensive weather station typically placed on the rooftop of their home. The climate data is displayed on a small screen and the observer may pen the information to paper for a record. The record-keeping in this scenario is not often consistent and regular, and is prone to bias. Similarly, a school class keeps a weather station in the yard to train young scientists in the methods of weather observations.

From a research perspective wind data is also collected for ecosystem, agri-

cultural, and hydrological studies. The wind data in these cases are usually for determining flux of gases, water, and other aerosols affecting the study area. There are also operational reasons for collecting wind data such as air traffic navigation, highway maintenance and safety, forest fire management, and recreation such as at the local ski hill in Whitehorse (Mt. Sima). For the purpose of energy extraction the wind climate is measured, as in the other research and operations noted above but the monitoring sites are placed in locations that are thought to have the most exposure to dominant winds and hence the best wind energy potential.

2.2. Wind climate stations in Yukon

There are 87 wind climate stations shown in Figure 2.1 and 2.2 that have been used for research and operational purposes. The numbers in these figures correspond to those tabulated below. These stations have been established, past and current, in the Yukon over several decades. The wind speed estimates are all given at 10-m AGL for consistency in comparison. All of the AES/MSC[1] sites are located in the valleys, and most are at airports. Most of the forestry sites (see Fig. 2.3 upper photo) are in the valleys but there are some that are located on mountaintops (above 1000 m ASL). While most airport stations have been in operation for decades, the forestry stations have been installed within the last decade and are becoming long-term. The forestry stations are prioritized to summer forest fire monitoring, they run year-round, however, but are prone to ice contamination.

[1]The "Atmospheric Environment Service" was renamed "Meteorological Service of Canada".

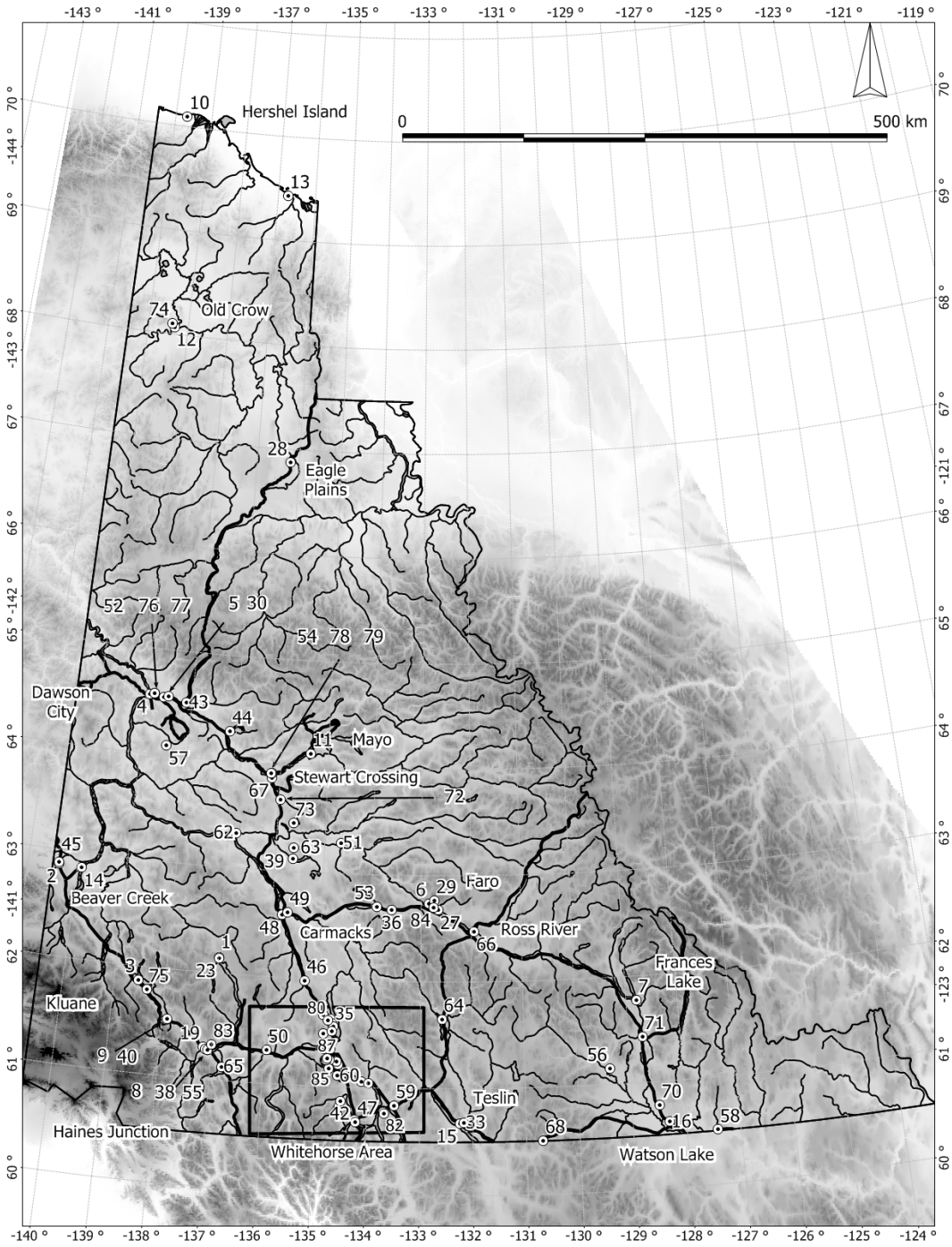

Figure 2.1: Map of past and present wind climate stations in Yukon. Refer to Table 2.1 for site description. See Fig. 2.2 for more detailed view of the Whitehorse area sites.

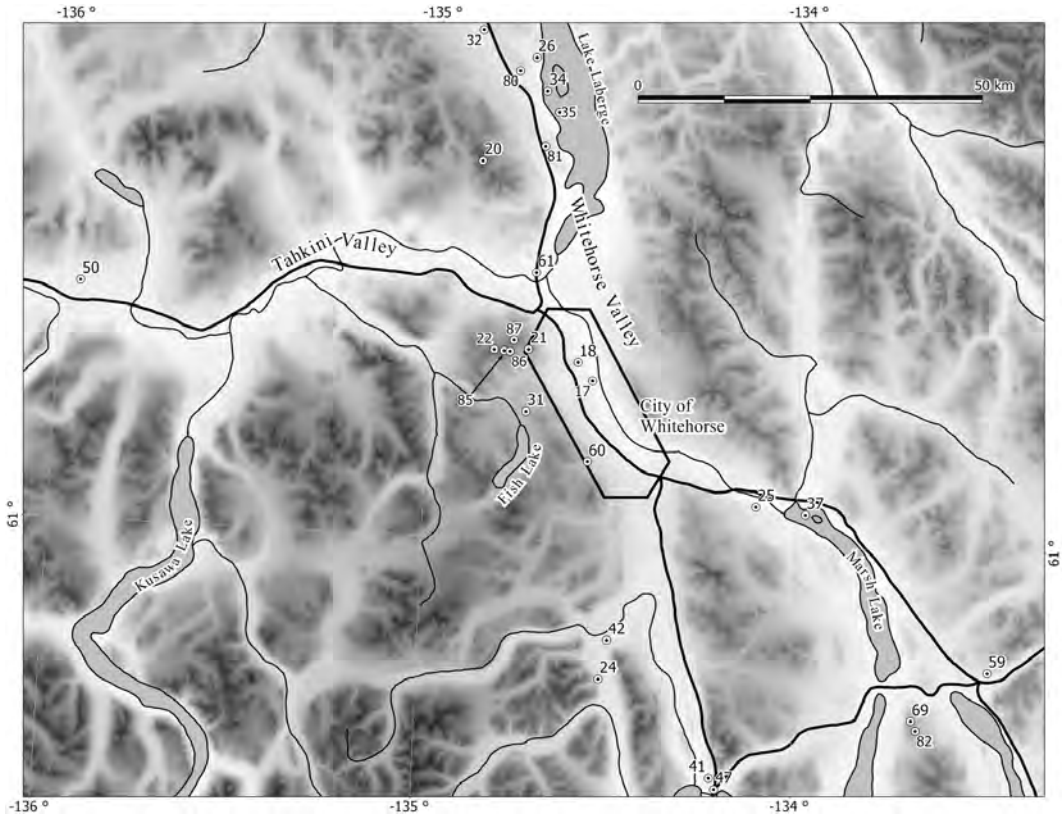

Figure 2.2: Wind climate stations in the Whitehorse area, inset from Fig. 2.1 above.

Table 2.1: List of past and current wind climate stations in the Yukon. The ID (column ID) numbers of the stations below correspond to those in Figure 2.1 and 2.2. The type refers to the owner of the project, refer to the List of Symbols and Abbreviations for the acronyms. The mean wind speeds (column U_{10}) were measured or estimated at 10 m AGL for time described in the period column. The status column indicates if the station still exists today. Most mean wind speeds were projected to long-term except for those accompanied by the symbol " * " — those were means of summer measurements only. The heights Z are the surface elevations in m ASL. The references (column Ref.) are: CCN82 – Canadian climate normals report AES (1982), KK55 – Kendrew and Kerr (1955), Wahl87 – Wahl et al. (1987), Pinard07 – Pinard (2007b), Pinard05 – Pinard et al. (2005), ESC – documents available from the Energy Solutions Centre, Government of Yukon, Forestry – data available from forestry website, Government of Yukon, Pinard05b – Pinard (2005), Baker95 – Baker (1995), and unplubl. – are reports from Yukon Energy Corporation, a public utility of the Government of Yukon.

ID	Type	Name	U_{10}	Z	Period	Status	Ref.
1	MSC	Aishihik A	2.8	966	1944-66	Ended	CCN82
2	MSC	Beaver Creek A	1.1	663	1969-80	Ongoing	CCN82
3	MSC	Burwash A	3.4	799	1966-80	Ongoing	CCN82
4	MSC	Dawson	1.8	320	1971-76?	Ended	CCN82
5	MSC	Dawson A	1.0	369	1976-80	Ongoing	CCN82
6	MSC	Faro A	2.1	694	1972-77	Ongoing	CCN82
7	MSC	Frances Lake	1.9	774	1942-47	Ended	KK55
8	MSC	Haines Junction	1.8	599	1963-80	Ongoing	CCN82
9	MSC	Kluane Lake A	2.5	786	1974-80	Ended	CCN82
10	MSC	Komakuk Beach A	5.8	13	1876-81	Ongoing	Wahl87
11	MSC	Mayo A	1.6	504	1955-80	Ongoing	CCN82
12	MSC	Old Crow A	2.2	251	1975-76	Ongoing	Wahl87
13	MSC	Shingle Point A	4.9	49	1974-81	Ongoing	Wahl87
14	MSC	Snag A	1.5	587	1944-66	Ended	CCN82
15	MSC	Teslin A	2.2	705	1955-80	Ongoing	CCN82
16	MSC	Watson Lake A	2.3	689	1953-71	Ongoing	CCN82
17	MSC	Whitehorse A	3.6	703	1963-80	Ongoing	CCN82
18	MSC	Whitehorse UA	2.6	704	2001-05	Ongoing	Pinard07
19	BAEC	Bear Creek	4.3	670	1998-00	Ended	Pinard05
20	BAEC	Flat Mtn	7.2	1930	Fall 1994	Ended	Pinard07
21	BAEC	HaeckelHill	5.9	1430	1998-01	Ended	Pinard05
22	BAEC	SumanikA	6.5	1702	Smr 2002	Ended	unpubl.
23	CWRAP	Aishihik Village	NA	966	2002-03	Ended	ESC

Continued on next page

Table 2.1 – continued from previous page

ID	Type	Name	U10	Z	Period	Status	Ref.
24	CWRAP	Annie (Campbell)	2.3	876	2000-01	Ended	ESC
25	CWRAP	Brown	1.6	687	2003-4	Ended	ESC
26	CWRAP	Campana	1.9	701	2000-01	Ended	ESC
27	CWRAP	Carreau	1.2	694	2000-01	Ended	ESC
28	CWRAP	Eagle Plains	3.3	725	2003-04	Ended	ESC
29	CWRAP	Faro Mine	4.5*	1318	2002-03	Ended	ESC
30	CWRAP	Finlay	0.7	496	2000-01	Ended	ESC
31	CWRAP	Fish (Bonhomme)	2.9	1175	2001-03	Ended	ESC
32	CWRAP	Fox Lake (Abbott)	1.2	793	2001-02	Ended	ESC
33	CWRAP	Greenwood	1.6	695	2003-04	Ended	ESC
34	CWRAP	Johnson	2.0	651	2002-03	Ended	ESC
35	CWRAP	Laberge (Lendrum)	3.8	645	2001-02	Ended	ESC
36	CWRAP	Lambkins	1.2	663	2003-04	Ended	ESC
37	CWRAP	Marsh Lake (Phillips)	2.6	656	2000-01	Ended	ESC
38	CWRAP	Pauls	2.1	621	2002-03	Ended	ESC
39	CWRAP	Tatlamun	NA	568	2004-06	Ended	ESC
40	CWRAP	Upton	2.2	806	2002-03	Ended	ESC
41	CWRAP	Watson (Luet)	2.0	702	2001-02	Ended	ESC
42	CWRAP	Wheaten (Rodden)	1.4	783	2002-03	Ended	ESC
43	Forestry	Antimony Creek	2.2	544	2005-07	Ongoing	Forestry
44	Forestry	Barlow	2.1	759	2005-07	Ongoing	Forestry
45	Forestry	Beaver Creek town	1.6	665	2005-07	Ongoing	Forestry
46	Forestry	Braeburn	2.6	725	2005-07	Ongoing	Forestry
47	Forestry	Carcross	2.5	660	2005-07	Ongoing	Forestry
48	Forestry	Carmacks	2.6	600	2005-07	Ongoing	Forestry
49	Forestry	Carmacks Airport	NA	538	2005-07	Ongoing	Forestry
50	Forestry	Champagne	2.3	732	2005-07	Ongoing	Forestry
51	Forestry	Detour	2.7	713	2005-07	Ongoing	Forestry
52	Forestry	Dome	3.2*	600	2005-07	Ongoing	Forestry
53	Forestry	Drury Creek	2.0	634	2005-07	Ongoing	Forestry
54	Forestry	Ferry Hill F	4.1*	1067	2005-07	Ongoing	Forestry
55	Forestry	Haines Junction Fire	2.0	601	2005-07	Ongoing	Forestry
56	Forestry	Hasselburg	1.6	878	2005-07	Ongoing	Forestry
57	Forestry	Henderson	3.3	1009	2005-07	Ongoing	Forestry
58	Forestry	Iron Creek	1.6	684	2005-07	Ongoing	Forestry
59	Forestry	Jakes	2.0	814	2005-07	Ongoing	Forestry
60	Forestry	Mt Sima	3.7	1180	2005-07	Ongoing	Forestry
61	Forestry	Nursery	2.2	674	2005-07	Ongoing	Forestry
62	Forestry	Pelly Farm	2.1	445	2005-07	Ongoing	Forestry
63	Forestry	Ptarmigan(1 m AGL)	3.5*	1487	2002-06	Ongoing	Forestry
64	Forestry	Quiet Lake	1.6	812	2005-07	Ongoing	Forestry
65	Forestry	Rainbow	3.2	793	2005-07	Ongoing	Forestry

Continued on next page

Table 2.1 – continued from previous page

ID	Type	Name	U10	Z	Period	Status	Ref.
66	Forestry	Ross River	1.2	680	2005-07	Ongoing	Forestry
67	Forestry	Stewart Crossing	2.4	500	2005-07	Ongoing	Forestry
68	Forestry	Swift River	1.9	878	2005-07	Ongoing	Forestry
69	Forestry	Tagish	4.3*	1200	2005-07	Ongoing	Forestry
70	Forestry	Tom Creek	2.5	938	2005-07	Ongoing	Forestry
71	Forestry	Tuchitua	1.0	731	2005-07	Ongoing	Forestry
72	Forestry	Willow Creek	2.3	800	2005-07	Ongoing	Forestry
73	INAC	McMillan Range	6.5	1345	Smr 2006	2008	unpubl.
74	YEC	Crow Mtn	4.5*	793	2002-04	Ended	Pinard05b
75	YEC	Destruction Bay	5.2	823	1995-98	Ended	Pinard05
76	YEC	East Dome	4.5	1036	1992-94	Ended	Baker95
77	YEC	East Dome 2	NA	1036	2004-06	Ended	unpubl.
78	YEC	Ferry Hill	NA	1279	2002-05	Ended	unpubl.
79	YEC	Ferry Hill 2	NA	988	2003-05	Ended	unpubl.
80	YEC	FoxRidge	4.3	937	Smr 2002	Ended	unpubl.
81	YEC	JackFish	5.3	990	Smr 2002	Ended	unpubl.
82	YEC	Jubilee Mtn	3.5	1280	1993-94	Ended	Baker95
83	YEC	Paint Mtn	4.3	1370	1992-94	Ended	Baker95
84	YEC	Sheep Look-out	3.1	795	2000-02	Ended	unpubl.
85	YEC	SumanikB	6.2	1588	Smr 2002	Ended	unpubl.
86	YEC	SumanikC	6.5	1590	Smr 2002	Ended	unpubl.
87	YEC	SumanikD	5.7	1535	Smr 2002	Ended	unpubl.

The wind data from the MSC and forestry stations have been recorded as hourly data while the BAEC, CWRAP, and YEC stations, installed specifically for wind energy monitoring, collected 10-minute means and standard deviations. These wind energy stations typically measured for at least one to two years, covering all seasons. Wherever possible the wind data from these non-permanent stations would be projected to long-term by correlating their record against nearby MSC stations (and more recently with the forestry stations). The priority with the wind energy stations has been to cover as many sites as possible, to determine the windiest locations.

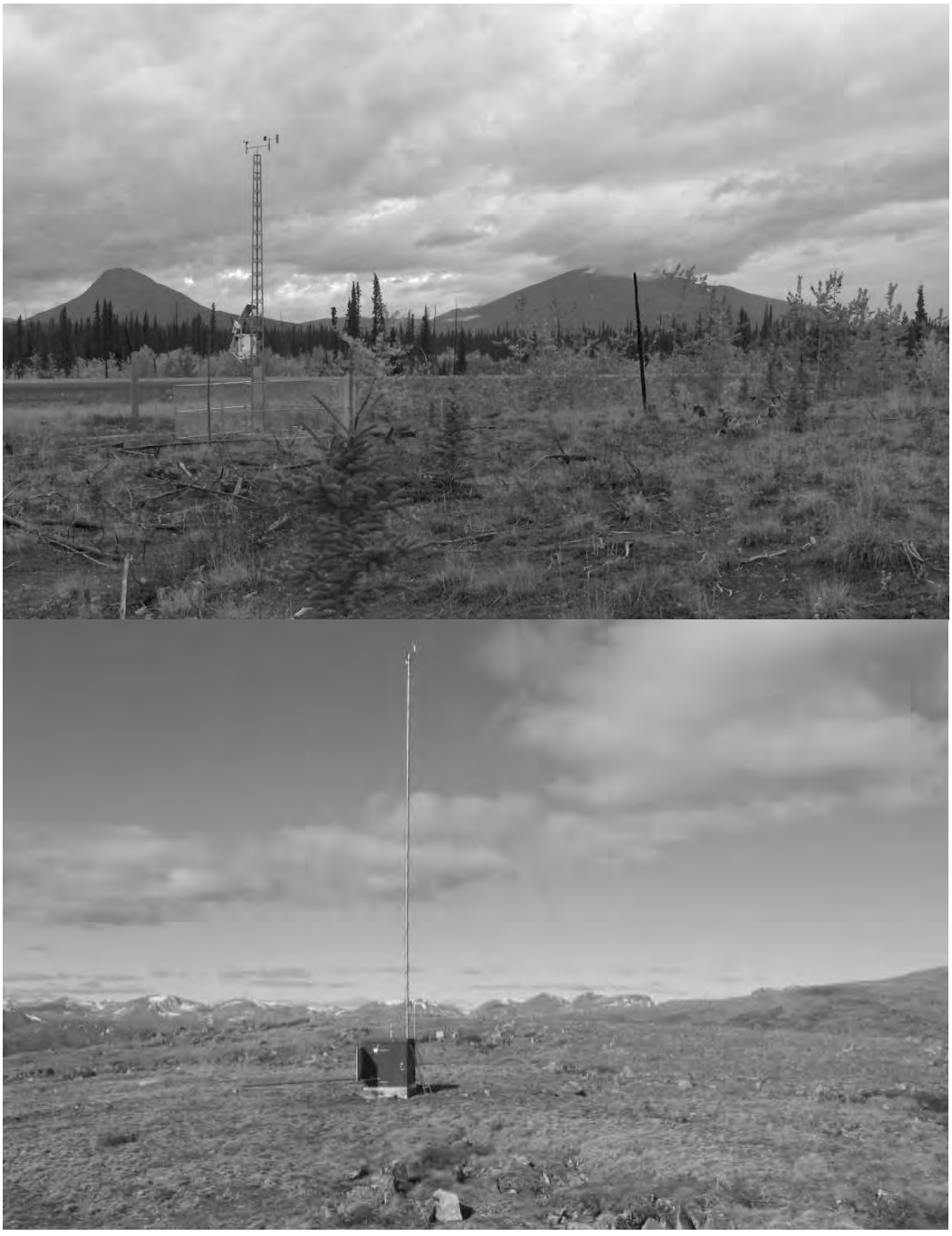

Figure 2.3: A forestry and a wind energy station. The forestry station (top image) is the Champagne station (#50) halfway between Whitehorse and Haines Junction. The wind energy station (lower image) is at Mt Sumanik (B #85).

While the BAEC and YEC (see Fig. 2.3 lower photo) stations were mostly installed on mountaintops to assess the large scale wind potential, the CWRAP stations (see Fig. 2.4) were focused on wind monitoring small-scale wind energy assessment for households and lodges. It is evident from the mean wind speeds at these stations that the wind energy potential at these valley sites is insufficient for commercially viable wind development (at 30 m the windspeed is typically 1.5 times the measured 10-m speed). This does not, however, prevent the remote household that is not connected to the grid from using a wind turbine to produce some portion of their energy needs, particularly in the summer. There is simply little wind in the winter when the electrical demand is greatest. This requires the remote home dweller to rely on fossil fuel generated electrical sources.

In Table 1 the stations whose wind speeds are accompanied by * are stations that have only measured winds during the summer months. They are also mountaintop stations where rime icing and difficult winter operation tend to shut down the data collection. Based on upper-air observations in and around the territory, at 1200 m ASL, above the inversion layer, the annual mean wind speeds are typically 20% above the summer mean. So it is conceivable that, could they be measured, annual mean winds at these surface stations might be around 1.2 times the summer mean values.

2.3. Types of instruments and equipment

A wind climate station typically consists of wind sensors on a tower connected to a datalogger at the base. The most commonly used anemometer is the cup anemome-

Figure 2.4: Two wind stations in the community wind resource assessment programme (CWRAP). The station in the top image was near Haines Junction (# 38) and the one in the lower image was at Eagle Plains (# 28).

ter, it is the simplest design and cheapest to manufacture particularly if it is a plastic body. Typically there are three cups made from either injection-molded black polycarbonate, or pressed aluminum. The cup assembly spins on a vertical shaft held by a bushing usually made of Teflon. The signal is created using either a small magnet to generate a low level AC sine wave, or an optical switch, and the resulting frequency is linearly proportional to the wind speed. The NRGSystems #40 maximum anemometer (maxi-40) is the most widely-used speed sensor in the wind industry and is shown in Figure 2.5 along with a #200P wind direction vane. The direction vane also rotates on a vertical shaft and is connected to a potentiometer.

The ultrasonic anemometer provides wind speed and direction by measuring time differences as sound travels through moving air from one transducer to another. The sensor has three (see Fig. 2.6 right side), four (in 2D horizontal plane), or six transducers (3D) that send and receive signals. The air flowing between the transducers causes a time lead/lag (compared to still air) in the signal leaving one transducer and arriving to another, this time change is used to calculate the wind speed. The ultrasonic anemometer has the advantage of no moving parts and being highly accurate and responsive to wind speed and direction fluctuations. Because of the added complexity required to process the signals, from an onboard computer, the price ranges from 10 to 20 times more than the cup anemometer and wind vane combined.

The propeller anemometer is on a horizontal shaft and is typically integrated with a wind vane. This arrangement offers some simplicity as there is only one instrument to install. Because of the vane/tail portion the propeller is always pointed

Figure 2.5: A three-cup anemometer and wind vane. (NRG #40 maximum anemometer and #200P vane by NRGSystems.)

into the wind. The propellers turn on the lifting force from the moving air along the axis of rotation. This type of anemometer uses the same principle as the cup sensor to send a signal to the datalogger. This type of sensor is rarely used in wind energy assessments although they are used at some AES stations. Other types of anemometers that are rarely used are the pressure transducer, and pressure tube. These anemometers also have no moving parts, however their limitation is in their vulnerability to dust, moisture and insects affecting the sensors.

Other characteristics of the climate that are also measured usually include temperature, and sometimes also pressure (p), relative humidity and icing events. Recording the temperature (T) is useful for deriving air density

$$\rho = \frac{p\ [\mathrm{Pa}]}{287\ T_v\ [\mathrm{K}]} \tag{2.1}$$

to estimate power output. Where the pressure is not measured, knowledge of the altitude of the site allows inference of a nominal pressure that suffices for calculating density. The pressure at the height of the station can be calculated using

$$p = p_o \, e^{(\frac{-g}{RT})z} \tag{2.2}$$

where $p_o = 1013.25$ mbar is standard sea level pressure, $g = 9.8$ m s^{-2} is the gravitational acceleration, $R = 287$ J $\cdot$ K^{-1}·kg^{-1} is the gas constant, T is the mean temperature (in units of K) at the site, and z is the height of the site above sea level (ASL). The virtual temperature $T_v = T \cdot (1 + 0.061 \cdot r)$ where r is the water-vapor mixing ratio[2]. A humidity sensor, although not very accurate in the winter, does provide clues of possible icing events. In locations where winter icing is a concern, an ice detector can measure the severity and potential effects that icing may have on wind power production.

In locations of expected icing, heated sensors are needed. A typical sensor model used in Yukon is the NRG IceFreeIII (see Fig. 2.6 left side) which is a heavier anemometer with a cast aluminum cup assembly rotating on a ball-bearing shaft. The heating elements are within the assembly, but fixed to the stationary body. The aluminum in the cup assembly transfers the heat from the interior to the outer parts of the assembly. Another heated sensor is the Vaisala (see Fig. 2.6 and 2.7) WAS425AH ultrasonic sensor, which has internal heaters covering the transducers. Vaisala also makes the WAA25, a heated cup anemometer also shown in Figure 2.7. Tammelin (2005) describes comprehensive tests of a variety of heated sensors

[2]The water-vapor mixing ratio r rarely exceeds 15 g/kg in the Canadian north, which would reduce the air density by a maximum 1%

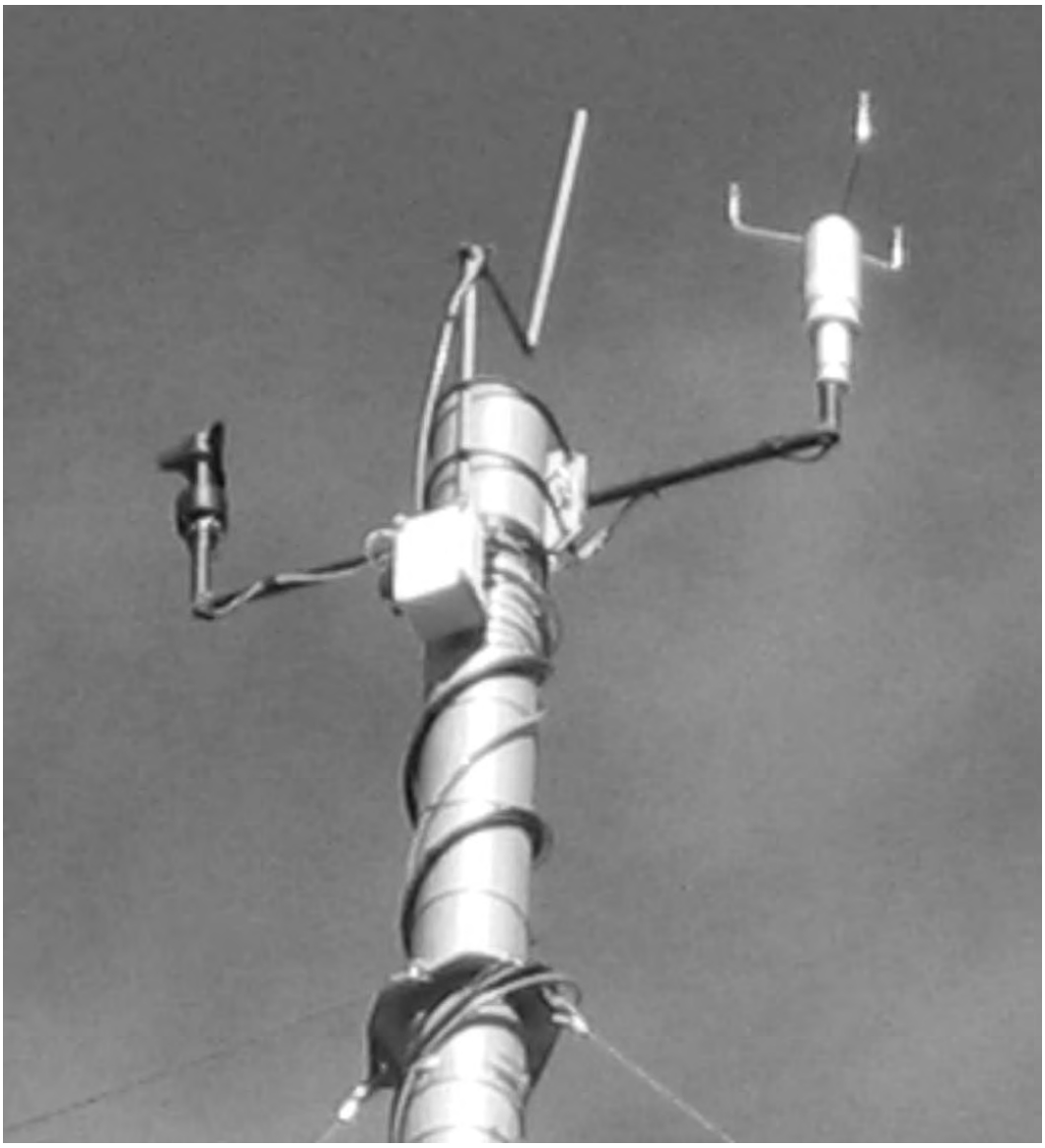

Figure 2.6: Two wind sensors at the top of a monitoring tower. Both are heated sensors. The ultrasonic anemometer on the right is equipped with an internal heater, it is a model 425AH by Vaisala. The three-cup anemometer on the left is an IceFreeIII by NRGSystems.

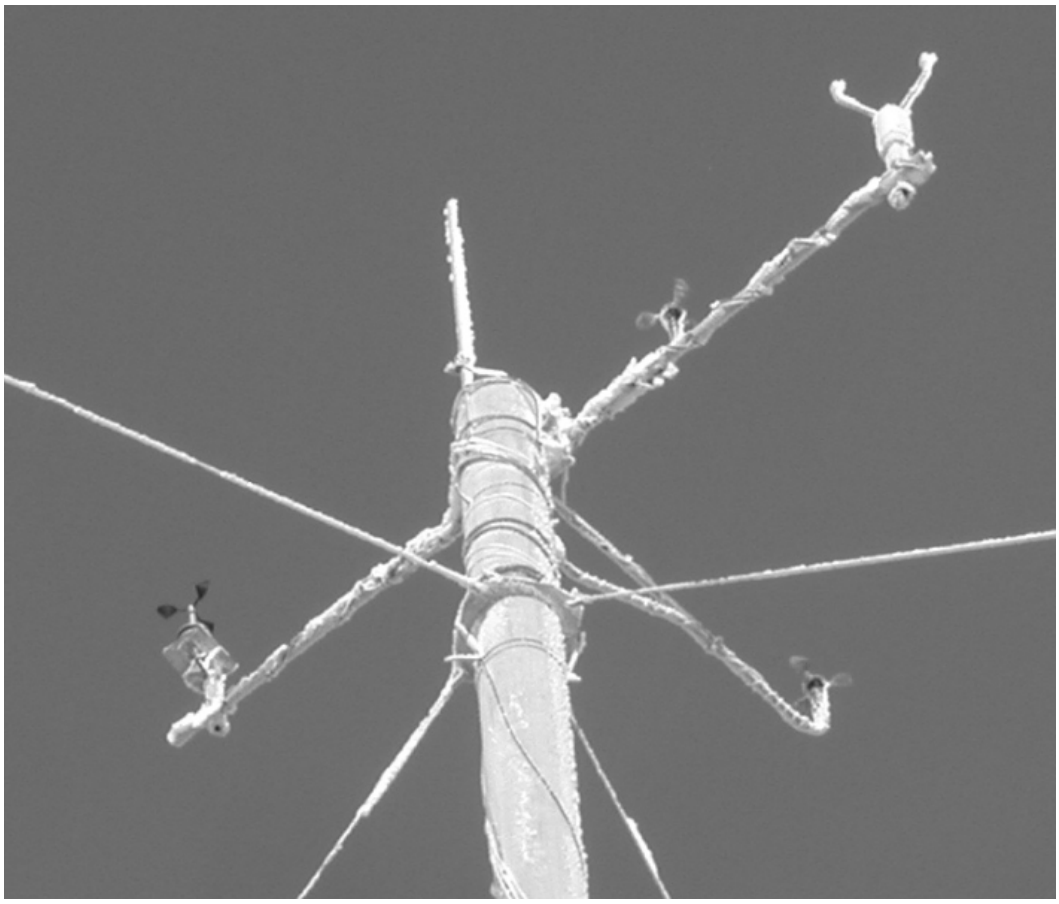

Figure 2.7: Wind sensors under a light icing environment. The two three-cup anemometers that are similar are maxi-40s and they are unheated. The ultrasonic anemometer (WAS425AH) on the right was equipped with an internal heater on the transducer, however ice would build up on the rest of the arm below the transducer. The sensor on the left is a heated Vaisala WAA25.

including those noted here.

The IceFreeIII has been the most reliable to date, but the heaters require a significant amount of power (50 to 250 watts). The WAS425AH uses less power (25 watts) for heating but has been prone to failure under heavy icing. In a remote site it is very difficult to keep the heated instruments powered continuously as there is typically no electrical grid connection to the site. A renewable energy

Figure 2.8: A severe icing event at a wind monitoring station. Note that the station has an instrument hut with an array of 8 PV solar panels and a wind turbine. The severity of the icing prevented the ability of the energy system to provide power to the heated sensors at the tower top (see Fig. 2.7) which were also covered in rime ice. Also note the rather large cylinders ($\sim$ 10 cm dia.) of ice built onto the guys of the tower.

system (solar, wind, and battery) is used, however it is very expensive to install and difficult to maintain (see Fig. 2.8). A solution to this problem is to install nearby a wind monitoring station that *is* connected to the electrical grid, and correlate the primary remote station to it in order to "fill the gaps" during periods hampered by icing. The two stations must be at similar altitudes (and have similar exposure to dominant winds), because the winter inversion may otherwise bias the correlation.

Data loggers are essentially small weather-rugged computers that receive the signals from the sensors, process the data and store them in memory until retrieval. The data can be retrieved either by a site visit when the local personnel exchanges a memory card or by wireless communications (cell phone, satellite, or radio). The

typical sampling interval of the sensors is one or two seconds (sampling frequency $f_s \sim 0.5 - 1$ Hz). The mean and standard deviation are calculated over 10-minute intervals – this is the wind industry standard for collecting wind data.

The towers used for supporting the wind sensors are usually tubular and are raised by tilting them from the ground using a ginpole and portable winch system (see Fig. 2.9). These tubular towers do not require heavy machinery to install. In the past they have been typically 10, 20, or 30 m tall; however the new standards are 50, 60 m and in some cases 80 m to measure at hub heights of the new larger wind turbines. The 10-m towers are still the norm for other types of climate stations. In the north, the smaller scale wind turbines are still about 30 m tall, however there is a push for taller towers to capture more wind energy.

2.4. Measurement errors

a. *Sensors*

The art of wind climate observations involves reducing the difference between the true wind characteristics and the measurements that instruments make. Sensors are calibrated and typically respond in a quasi-linear fashion to the wind speed in the lab. The specifications and reports provide a slope and offset with the accompanying anemometer. Although re-calibration is not typically necessary on the maxi-40s, after ten years the anemometer would likely be taken out of service. With a model like the maxi-40 the accuracy is typically within 0.1 m s^{-1} in the range of 5 to 25 m s^{-1} (the datalogger measures with 0.1% resolution).

Figure 2.9: Winching a tower into the upright position. This is a 30-m tubular tower being installed at Aishihik Lake (Site # 23). Taller towers require high-power portable electric winches.

In the open environment however, other factors will affect the accuracy of the instruments (see Wyngaard 1981, for further discussion). In the cup anemometer for example, particularly the heavier models, the cup assembly accelerates quickly with wind gusts but because of residual rotational momentum they freewheel as the wind speed drops, thus measuring an overspeed. This lag is quantified as a distance constant, which is the length of air flow past the sensor required to cause it to respond to 63.2% of a step change in speed. An acceptable range for distance constant is 2 to 5 m, for the maxi-40 it is 3 m while for the IceFreeIII it is 7.6 m. In gusty wind condition the error can be as much as 5-13 % of the mean wind (see

Linacre 1992; Busch and Kristensen 1977), which translates to an error of 0.3 to 0.8 m s^{-1} for a mean wind speed of 6 m s^{-1}.

Another source for error is in the vertical component of the wind that can cause a slight speed-up of the anemometer. This is a concern if the station is on the edge of a steep-sloped mountaintop where upslope winds meet the sensors. In Pedersen and Paulsen (1999) (also see Pedersen et al. 2006; Papadopoulos et al. 2001) a comparison of 5 common cup-anemometers shows differing responses to vertical angling of wind direction. While the maxi-40 has errors within 5% for a tilt angle range of $\pm$ 20 $^\circ$ some models can have serious overspeeding due to air-lifting effects (see Tammelin et al. 1996). For the propeller anemometer the response to deviation in the direction of the wind from the propeller axis follows the cosine law. Under normal operations of low turbulence and nearly horizontal winds, the accuracy for the anemometers discussed here is typically within 2%.

b. *Placement of sensors*

Other sensor errors are also associated with nearby obstacles. The tower can cause turbulence and a reduction of the wind speed if it is upstream of the anemometer. To avoid this situation the anemometer should not be downstream of the tower to the dominant wind directions (IEC 2005). The anemometer should also be at least 10 diameters away from the tower. This can necessitate long booms which can create other problems such as boom vibration and a larger, more vulnerable ice-loading surface. It is safer to use a shorter boom (typically 1.5 m long) and to orient the

boom strategically on the tower so that it is well exposed to the dominant wind directions. In mountainous terrain there are typically two dominant directions that are nearly opposite to each other. The sensor boom is oriented perpendicular to those directions. For added insurance a redundant anemometer, usually at the tower top, is placed on the opposite side of the tower. An anemometer that is placed above the tower top (Perrin et al. 2006) must be at least 5 diameters beyond the top, otherwise it will experience a speed-up from the tube below. At this height the speed-up error will not be larger than 1%.

On mountaintops this is rarely a problem, but for the valley stations such as at airport, highway, and forestry stations, the monitoring towers in some cases are located near buildings, forest and small hills. These obstacles obviously cause a local speed perturbation, usually a reduction, such that wind statistics measured at the station are not necessarily representative of the larger region. Local wind perturbations also invalidate (or at least, compromise) the practise of establishing a correlation of the wind speed with that measured at other sites: in this scenario one may have to correlate by wind direction, to account for the nearby obstacles.

As indicated above, winter icing is a common cause of error causing a reduction in the measured wind speed. To detect periods of icing one looks for clues including:

- temperature below freezing and high relative humidity
- abnormal spikes in the standard deviations of wind speed and direction
- standard deviation of wind speed below the normal value for that wind speed

and site. Cause: ice-buildup increases moment of inertia, resulting in sluggish response to wind speed fluctuations

- no change in direction and/or speed, i.e. standard deviation is zero. Cause: vane assembly ice-bridged to base

- on the same tower the correlation between two or more anemometers deteriorates. The severity of icing can vary between different elevations on a tower.

2.5. Data analysis and climate estimates

Wind measurement analysis is a step (eg. see Pinard 2007a) between obtaining the data and applying it to quantify the economics of a wind farm. In the initial stage we estimate the annual mean wind speed to verify that the site passes the first test of economic viability – that it meets the minimum annual mean wind speed requirement. Typically the baseline annual mean wind speed is 6 m s^{-1}, but this limit goes up to 7 m s^{-1} if the site is near a large electric grid in Southern Canada were electricity is relatively cheap. The limit can be lowered to 5 m s^{-1} in a more remote location, where diesel-electric generation carries a much higher cost.

Wind energy monitoring stations typically have a lifetime ranging from 6 to 24 months (in some cases with gaps in the data). Because of the relatively short period of measurement, wind statistics from these stations tend to deviate from the long-term mean. By correlating the wind monitoring station to a longer term data set (eg. airport) we can reduce this sampling error (or increase the confidence level). There are usually over a decade of wind data available from nearby airport

stations or radiosondes. On the mountaintops of the Yukon the upper-air data is an important source for making correlation and long-term predictions for a site of interest. Although the measurements are made only every 12 hours, the correlation of monthly (and daily) means between the mountaintop surface and the upper-air measurements (at similar heights) can be quite good ($R^2 > 0.75$) for a surface station that is O(100) km away.

The long-term mean at a site of interest is determined by comparing it to a nearby long-term station. If the correlation between the two sites for the same period of measurement is good then, by simplest method, a ratio of mean wind speeds of the long- and short-term measurements of the long-term station is made and multiplied to the short-term mean wind speed of the site. A more elaborate and well known technique of projecting to long-term is called measure-correlate-predict (MCP, Burton et al. 2001). In this technique the relationship between the two data sets (the site of interest and the nearby long-term station) over the same period is defined using a linear regression in the form of:

$$U_{site} = a + bU_{long-term} \tag{2.3}$$

where a and b are the offset and slope. More accuracy is gained by calculating the coefficients in, say, 12 direction sectors of 30 $^\circ$ each. With a and b known, a long-term projection of say ten years at the site of interest is calculated by substituting the ten-year mean wind speed of the long-term station into $U_{long-term}$.

The nearby long-term measurements are also used to estimate the long-term monthly mean wind speed at the site of interest. This helps to determine the sea-

sonal fit between the potential wind energy production and local energy load. Using the measured temperature and the estimated (or sometimes measured) mean pressure we can also determine the mean air density which is used to calculate monthly wind energy production. It is also useful to calculate the daily variation of wind speed during different seasons of the year. This is helpful in determining a match between wind energy production and peak daily loads on a small local grid.

The wind energy-frequency rose helps determine where the most energetic winds are from at the site of interest. Knowing these important dominant wind directions provides clues for finding other nearby sites that may have better wind potential and also provides guidance for placing wind turbines at the site of interest. The wind energy-frequency by direction is calculated as the frequency of occurrence of the wind in a given direction sector multiplied by the cube of the mean wind speed in the same direction. Typically there are 16 direction sectors and each sector is 22.5 degrees wide. The given wind energy in each direction is a fraction of the total energy for all directions. The more traditional wind rose which is a wind frequency distribution by direction can sometimes be misleading, showing a commonly occurring wind direction that is not significant for wind energy production.

The wind speed distribution consists of a frequency of occurrence of 10-minute means in, typically, 1 m s^{-1} bins. That frequency bin is multiplied by the power curve of a select turbine to estimate monthly and annual wind energy production. In some cases the data set is not sufficient and so requires a curve fitting exercises. The wind speed distribution can be modelled with the Weibull curve (after Stull

2000):

$$f(U) = \frac{k_s \, \Delta U \, U^{k_s - 1}}{A^{k_s}} \, \exp\left[- \left(\frac{U}{A} \right)^{k_s} \right] \tag{2.4}$$

Here k_s is the Weibull shape factor, A is the scale factor (and is proportional to the mean wind speed), ΔU is the width (or resolution) of the bin, and $f(U)$ is the probability that the wind speed will be $U \pm \frac{\Delta U}{2}$.

2.6. Projecting measured winds to other heights

When the monitoring tower height is shorter than the intended wind turbine hub height, the measured mean wind speed needs to be projected upwards to estimate the wind speed at the new height. On relatively flat terrain that vertical projection can be made by fitting a logarithmic wind speed profile to the measurements at the different elevations. More specifically, one employ's the classic mean wind profile:

$$u(z) = \frac{u_*}{k_v} \ln \left(\frac{z}{z_o} \right) \tag{2.5}$$

where u_* is the friction velocity, k_v is von Kármán's constant (it is typically assumed that $k_v = 0.4$), and z_o is the surface roughness length. If the wind speed is known at two or more heights then z_o can be easily determined from a curve fitting exercise using:

$$u_2 = u_1 \frac{\ln(z_2/z_o)}{\ln(z_1/z_o)} \tag{2.6}$$

where u_1 is the known wind speed at elevation z_1 (usually 10 m AGL), and is projected to u_2 at the height z_2. A rule of thumb is that z_o is 1/10 the height of the forest or grass surrounding the tower (note: in case of a forest, it is advisable to work with the displacement length d, typically taken as about 2/3 of the forest

height: where height z appears in the wind equation, it is replaced by $z - d$ such that in effect, the forest is regarded as shifting the coordinate origin upwards).

The log law equation is valid in a neutral (i.e. unstratified) atmosphere, but a diabatic correction is straightforward if one has access to measurements that would determine the Obukhov length L_o: for example in stable stratification:

$$u(z) = \frac{u_*}{k_v}\left(\ln\frac{z}{z_o} + 6\frac{z - z_o}{L_o}\right) \tag{2.7}$$

The "stability parameter" L_o is sometimes called the "height of the substrate of dynamic turbulence", it is positive in stable stratification, negative in unstable stratification, and infinite (+ or -) under neutral stratification. The Obukhov length L_o is, however, a function of the surface heat flux, which it is not possible to infer from the typically available data of a wind energy station.

The power law wind equation, sometimes known as Archibald's Law, is a useful alternative to the log law:

$$u_2 = u_1\left(\frac{z_2}{z_1}\right)^{\alpha} \tag{2.8}$$

Evidently the parameter α must be a function of stability, surface roughness and the height range over which the wind speeds are determined. It can be determined from two levels of data using:

$$\alpha = \frac{\ln(u_2) - \ln(u_1)}{\ln(z_2) - \ln(z_1)} \tag{2.9}$$

In most cases the power law wind profile can be conformed to the same curve derived by Equations 2.4 and 2.7 above. In complex terrain the changing surface roughness combined with orography requires calculations through microscale numerical modelling such as described in section 3.3.

Bibliography

2005: IEC 61400-12-1 ed.1: Wind turbines - part 12-1: Power performance measurements of electricity producing wind turbines. Technical report, International Electrotechnical Commission.

AES, 1982: *Canadian Climate Normals Vol. 5 1951-1980*. Environment Canada, 283 pp.

Baker, D. R., 1995: Annual report wind monitoring and analysis. Technical report, Nor'wester Energy Systems Ltd., prepared for the Yukon Energy Corporation, Box 5920, Whitehorse, Yukon, Y1A 6S7, 350 pp.

Burton, T., D. Sharpe, N. Jenkins, and E. Bossanyi, 2001: *Wind Energy Handbook*. John Wiley and Sons, Ltd.

Busch, N. and L. Kristensen, 1977: Cup anemometer overspeeding. *J. Applied Meteorol.*, **15**, 1328–.

Kendrew, W. G. and D. Kerr, 1955: *The Climate of British Columbia and the Yukon Territory*. Edmond Cloutier, Queen's Printerb, Ottawa.

Linacre, E., 1992: *Climate Data and Resources: A Reference and Guide*. Routledge.

Papadopoulos, K., N. Stefanatos, U. Paulsen, and E. Morfiadakis, 2001: Effects of turbulence and flow inclination on the performance of cup anemometers in the field. *Bound. Layer Meteorol.*, **101**, 77–107.

Pedersen, T., J.-Å. Dahlberg, and P. Busche, 2006: ACCUWIND -classification of five cup anemometers according to IEC61400-12-1. Technical report, RISO.

Pedersen, T. F. and U. S. Paulsen: 1999, Classification of operational characteristics of commercial cup-anemometers. *Wind Energy for the Next Millennium. Proceedings. 1999 European Wind Energy Conference (EWEC '99).*

Perrin, D., N. McMahon, M. Crane, H. J. Ruskin, L. Crane, and B. Hurley, 2006: The effect of a meteorological tower on its top-mounted anemometer. *Applied Energy*, 413–424.

Pinard, J. D. J.-P., R. Benoit, and W. Yu, 2005: A WEST wind climate simulation of the mountainous Yukon. *Atmosphere-Ocean*, **43**, 259–282.

Pinard, J.-P.: 2005, Wind climate of the mountainous Yukon. *New Northern Lights: Graduate Research on Circumpolar Studies from the University of Alberta*, Canadian Circumpolar Institute.

Pinard, J.-P., 2007a: Executive progress report for wind energy monitoring in six communities in the NWT. Technical report, Aurora Research Institute, Inuvik, NWT, Canada, http://www.nwtresearch.com/publications.aspx.

— 2007b: Wind climate of the Whitehorse Area. *Arctic*, **60**, 227–237.

Stull, R. B., 2000: *Meteorology for Scientists and Engineers*. Brooks/Cole, second edition edition.

Tammelin, B.: 2005, Ice-free wind sensors. *BOREAS VII Proceedings*.

Tammelin, B., R. Hyvonen, and A. Peltomaa: 1996, The accuracy of wind measurements in hilly regions. *BOREAS III*, 232–244.

Wahl, H. E., D. B. Fraser, R. C. Harvey, and J. B. Maxwell, 1987: Climate of Yukon. Technical report, Environment Canada, Ottawa.

Wyngaard, J., 1981: Cup, propellor, vane and sonic anemometers in turbulence research. *Ann. Rev. Fluid Mech.*, **13**, 399–423.

Chapter 3

Mountain wind climate

3.1. General atmospheric circulation and the Western Cordillera

About 75% of the mass in the earth's atmosphere lies within the troposphere, whose depth at mid-latitudes is about 11 km. At the equator, owing to its higher temperature and (consequently) lower density, the tropospheric depth averages about 15 km and can reach 20 km. Conversely at the poles the tropospheric depth can vary from roughly 7 km in the summer to a only few hundred metres in winter. The upper portion of the troposphere is the "free atmosphere," where in general the wind is nearly in geostrophic balance, i.e. blows parallel to isobars (or height contours) and at a speed inversely proportional to the contour spacing (i.e. in direct proportion to the strength of the pressure gradient). The lower portion of the troposphere that is influenced by surface friction and orographic disturbances is known as the planetary boundary layer (PBL). In this layer the wind is affected by turbulence, whose origin lies in wind shear that (in turn) is a result of surface or orographic drag (in summer, daytime buoyancy enhances the turbulence). The turbulence gives rise to a vertical flow of mean momentum, whose divergence is the "friction force" and results in a component of the wind across the isobars towards lower pressure (an *ageostrophic* force balance). In mid- to upper-latitudes the PBL depth can vary from as low as a few hundred metres to a few kilometres — depending on topography, time of day, season, and strength of the upper winds.

On a synoptic scale[1] it is well understood that the uneven heating of the earth

[1]When meteorologists describe the atmosphere on the 'synoptic scale', implicitly they are referring to properties of the atmosphere that have been averaged on horizontal planes over an area of

creates circulation cells that drive warmer equatorial air upward and then poleward, while cool polar air descends at high latitude and moves equatorward. These circulations take place within the troposphere which, with its depth of order 10 km, is very thin relative to the 10,000-km distance from the equator to the north pole. The ascent of warmer air and subsidence of cooler air creates pressure gradients that in turn drive the horizontal winds. The earth's rotation causes the upper free-atmospheric winds to flow nearly parallel to the pressure contours (i.e. perpendicular to the pressure gradient). In the northern hemisphere at the mid- and high-latitudes the mid-tropospheric winds are generally westerly, blowing along the contours of pressure with high pressure (generally) toward the equator. The orientation of this generally westerly current is diverted by the continents and the mountain ranges.

In North America the Western Cordillera — well over 2000 km long, and extending northwest-southeast from Alaska down to the western United States — is such a barrier to these westerlies. In Figure 3.1 the pressure pattern is represented by the field of geopotential height (i.e. height of a constant pressure surface, a representation that is more convenient than charting the pressure field on a constant height surface) and at 700 mbar the contours[2] can represent streamlines of the upper-air flow at approximately 3000 m ASL. Over the North Pacific Ocean as the airstream approaches the Canadian coast air is diverted northward, climbs the Western Cordillera and then returns southward to resume its westerly flow (over

order 100 km $\times$ 100 km in a domain that is typically 2000 $\times$ 2000 km.

[2]These contours are derived from the NCEP/NCAR (National Centers for Environmental Prediction/National Center for Atmospheric Research) Reanalysis web site.

Ontario). The Cordillera within Canada creates a ridge of high pressure, pushing the isobars northward over the mountains. While this is an annual mean representation of pressure gradient, the steepness of the gradient in winter is nearly double that of the summertime.

Wind energy-frequency roses extracted from radiosondes at 3000 m ASL are shown in Figure 3.1, and indicate the general alignment of the wind at this height with the contours of geopotential height at 700 mbar. The measured wind speeds at this elevation also double during the winter months, which is the corollary of the steepened height gradient (due to a stronger latitudinal temperature contrast). The three stations along the BC coast and the Alaska panhandle are at a greater angle to the contours than the others. This could be attributed to two factors: first, the sparse number of stations in this region create a rather coarse interpretation of the contours; second, the orographic friction on the flow reduces the Coriolis influence and these winds respond more directly to pressure gradient instead.

Within the PBL, closer to the earth's surface a somewhat different picture emerges in regard to the relation between measured flow and the sea-level pressure gradients. In Figure 3.2 an annual mean sea-level low pressure centre resides over the Aleutian Islands in Alaska, while a mean high (sea level) pressure centre sits on the mainland Northwest Territories. The measured winds near the surface show a general trend of southerly to southeasterly winds along the west coast and the interior of BC, and northwesterly winds on the lee (eastern side) of the Cordillera. We can easily deduce that the near-surface winds are more markedly affected by local orography and other local factors than by sea-level pressure. In the southern Yukon for exam-

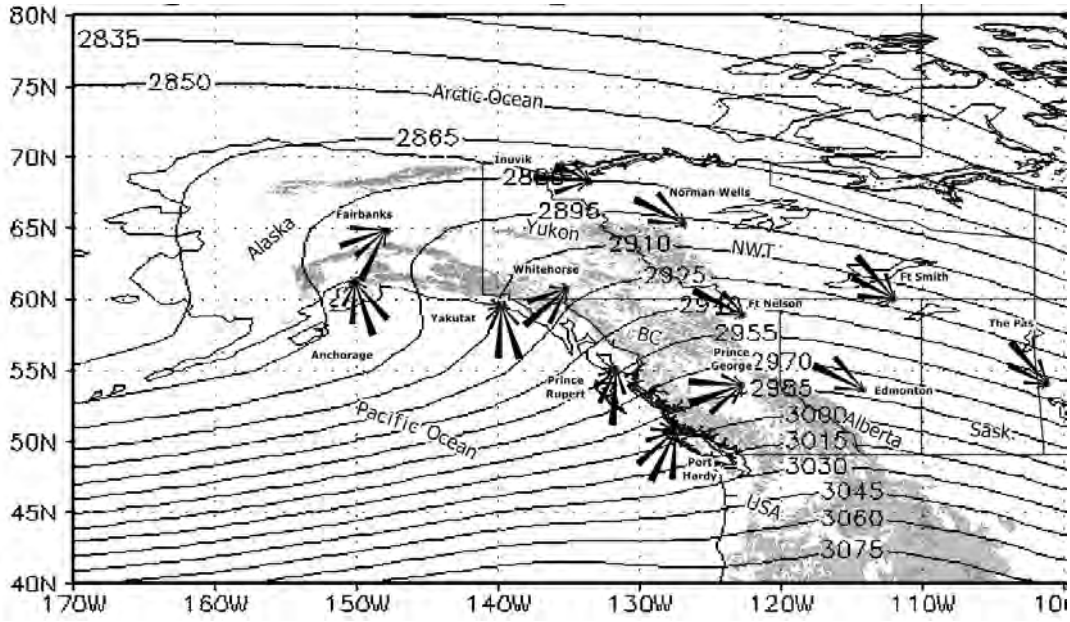

Figure 3.1: Long-term annual mean geopotential height of the 700 mbar surface derived from NCEP/NCAR Reanalysis. The contour interval is 15 m. The wind roses are from select radiosondes on both sides and within the western cordillera. The wind roses from the radiosonde observations are at 3000 m ASL.

ple, the south-southeasterly wind follows the orientation of the valley within which the radiosonde station is located. The surface station here is however over 700 m ASL so it is not likely influenced by sea level pressure gradient. Another example is the bi-model distribution of wind direction in Norman Wells, due to the weekly movement of the passing pressure systems — but the orientation of the near-surface wind is confined by the surrounding valley.

Like the pressure gradient aloft, the sea-level pressure gradient also (roughly speaking) doubles in winter, but mostly along the Pacific coast. Although observed mountaintop and coastal winds increase in the winter, typically, the surface winds within the valleys decrease (Pinard 2005). This is a consequence of the frequent

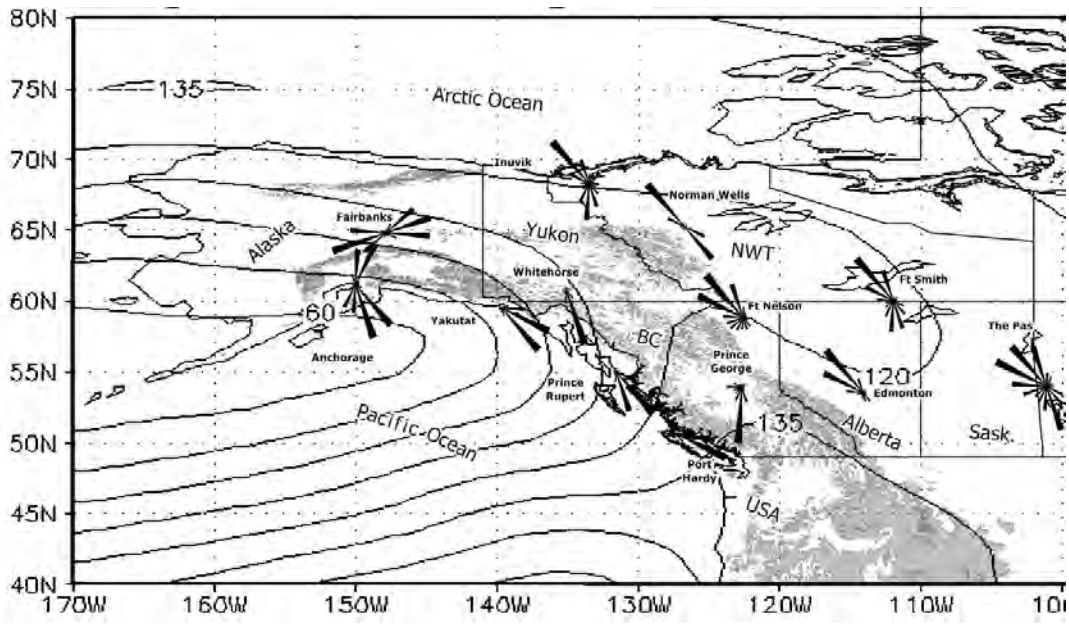

Figure 3.2: Long-term annual mean geopotential height at sea level derived from NCEP/NCAR Reanalysis. The contour interval is 15 m. The wind roses are from select radiosondes on both sides and within the western cordillera. The wind roses from the radiosonde observations are at 100-200 m AGL.

occurrence of intense winter inversions, which play an important role in mountain wind climates. The inversion forms during periods when the net radiation at the ground surface is negative. The small (or even non-existent) daily solar insolation in high latitude winter ensures the formation of an inversion, which may be sufficiently strong as to inhibit or prevent convective mixing along the vertical — with the result that the free winds aloft are effectively decoupled from the surface air, permitting strong winds aloft over a layer of cold, dense, and stationary or slowly moving surface air. Thus despite the generally stronger winter winds aloft, with a few exceptions surface valley winds are weaker in winter than in summer.

3.2. Mountain wind climates under stable stratification

Several observational campaigns have focussed on mountain wind climates. An important project was the Mesoscale Alpine Programme (MAP) study that started in the mid-1990's. During this study period there were investigations of the turbulence structure within the valleys, studies of gap winds and föhn winds. An overview can be found in Rotach and Zardi (2007). Other regions where mountain wind flows have been systematically observed include the valley of Lake Torneträsk in northern Sweden (Smedman and Bergström 1995), the Tennessee Valley (Whiteman and Doran 1993), the Grand Canyon (Whiteman et al. 1999), Shelikof Strait (Alaska) (Lackmann and Overland 1989), and the Strait of Juan de Fuca (Overland and Walter 1981). Most of these studies have focused principally on the relationship between the valley winds and those aloft and the role that atmospheric stability plays in that relationship.

In the PBL over mountainous terrain there are two important sets of characteristics that affect air motion: first the height, width, length, and spacing between successive mountain ridges; and second, properties of the flow itself — the wind direction relative to the orographic barrier, the vertical profile of the wind speed, and the temperature lapse rate (see Barry 2001, for further discussion). Concerning the dimensionality of the mountain barrier, an air mass will likely flow over a small hill of slight slope whereas it may be forced around a rather tall, steep, isolated mountain. If the mountain is wide enough the air could either flow over the ridge, be

deflected around, some combination of both, and/or be completely blocked at low elevations. In the case of successive ridges, the flow approaching a downstream ridge has been disturbed by the prior ridge and so the air mass within the valley may become completely decoupled from the air aloft.

The flow characteristic is dominated by the static stability of the atmosphere within which an air parcel moves. In northern latitudes the PBL is usually stably stratified. In this situation an air parcel is resistant to being displaced vertically from its resting position. This has implications on how a flow behaves as it approaches an orographic obstacle. The static stability defines a buoyancy frequency N (also known as the Brunt-Väisälä frequency), formulated as

$$N = \sqrt{\frac{g}{T_v}\left(\frac{\partial T_v}{\partial z} + \Gamma_d\right)} \tag{3.1}$$

The buoyancy frequency is determined by the virtual temperature lapse rate $\partial T_v/\partial z$ (in relatively dry air, $T_v \simeq T$), or more specifically, by its deviation from the dry adiabatic lapse rate $\Gamma_d = 9.8\,\mathrm{K\,km^{-1}}$. In the southern Yukon the in-valley buoyancy frequency is typically $N_{summer} \simeq 0.01$ and $N_{winter} \simeq 0.02 - 0.03$. Above the mountaintops $N \simeq 0.01$ year round although the temperature profile will shift by -15°C from summer to winter.

In combination with the buoyancy frequency N, the horizontal wind speed U also plays an important role in the behaviour of an air parcel that impinges on a mountain obstacle. For simplicity, if we choose one of the dimensions of the mountain, the height H, we can also use the Froude number (Arya 2001) to characterize

the tendency for an air parcel to flow around or over a mountain obstacle[3]. The Froude number, giving the ratio of inertial to buoyancy forces in the flow, can be defined as:

$$F = \frac{U}{NH} \tag{3.2}$$

We can refer to Figure 3.3 (c) to show that for an undisturbed oncoming flow where $F \geq 1.0$, an air parcel near the base of a mountain will have enough inertia to overcome the loss of energy entailed in ascending against the downward buoyancy force, and will climb over the mountain. In the mountains of Southern Yukon however, particularly in the Whitehorse Valley we would expect:

$$F_{summer} \simeq \frac{5\ \mathrm{m\,s^{-1}}}{0.01\ \mathrm{s^{-1}} \times 1000\ \mathrm{m}} = 0.45 \tag{3.3}$$

$$F_{winter} \simeq \frac{8\ \mathrm{m\,s^{-1}}}{0.02\ \mathrm{s^{-1}} \times 1000\ \mathrm{m}} = 0.35 \tag{3.4}$$

For $F < 1.0$ there is a dividing streamline height h below which the air (theoretically) flows horizontally around the barrier, and above which the air flows over the mountain (see Fig. 3.3 (b)). Imagine h as the depth of a "river": the colder, denser valley air mass, that moves horizontally around mountains and through valley systems. In a stably stratified atmosphere where $F < 1.0$ we can use the relation $h/H = 1 - F$ (introduced by Hunt and Snyder 1980) to estimate the depth h of the air mass that flows within the valley, decoupled or separated from the winds aloft (also see Barry 2001, for further discussion). As the wind speed decreases and the

[3]We can also replace H with a streamwise length L of a hill. In mountainous terrain such as around Whitehorse the length L is typically of the order 10 km. This is much larger than H, so this further reduces the value of the Froude Number F.

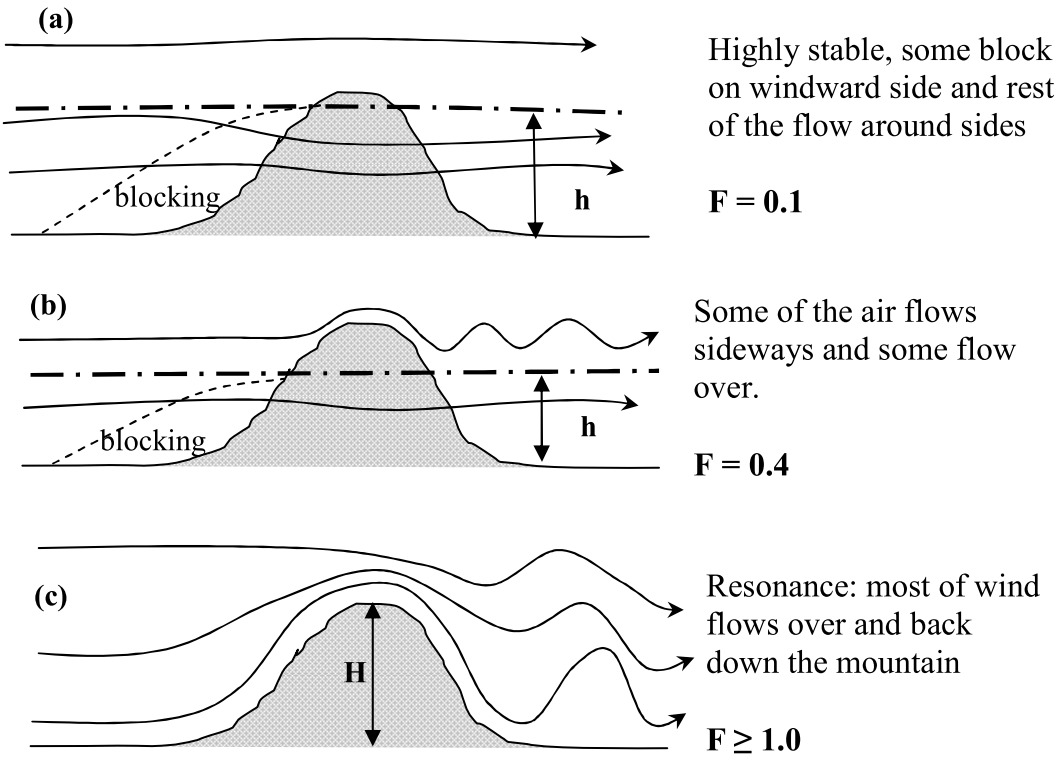

Figure 3.3: Flow impinging on an isolated mountain, under different Froude number conditions. After Stull (1988).

stability increases the depth h of the dividing streamline increases. In the Whitehorse Valley then, we might expect $h_{summer} \simeq 550\ m$ and $h_{winter} \simeq 650\ m$ above the valley floor (assuming a valley depth of 1000 m).

In the northern hemisphere when a statically stable atmospheric layer impinges upon a ridge it will tend to deflect cyclonically (i.e. toward the left, facing downwind). According to Smith (1982) as air approaches a mountain obstacle it decelerates as it encounters an orographically disturbed high pressure region (see Fig. 3.4). As the flow decelerates the Coriolis influence decreases and the air turns left because the background pressure gradient acts from the right of the oncoming flow. The Coriolis effect can be related to the Rossby number, the ratio of Coriolis (f^{-1})

and inertial (L/U) timescales,

$$R_o = \frac{U}{fL} \tag{3.5}$$

According to Carruthers and Hunt (1990), Coriolis effects are significant in motion for which $R_o \leq 1$ with the consequence that the air flows parallel to the isobars. For a wind $U = 10\mathrm{m\,s^{-1}}$ crossing a mid-latitude domain of streamwise length scale (say) $L = 100$ km the Rossby number becomes

$$R_o = \frac{10\ \mathrm{m\,s^{-1}}}{10^{-4}\ \mathrm{s^{-1}} 100\ \mathrm{km}} = 1 \tag{3.6}$$

Taking a smaller-scale domain, e.g. flow over a hill with a domain length of $L = 10\ \mathrm{km}$, a larger Rossby number $R_o = 10$ results, and rotational effects become insignificant and the flow becomes largely driven by pressure only.

Within valleys the air tends to flow along the valley axis, confined by the surrounding ridges. The valley flow responds to several kinds of forcings, not exclusive of each other. Whiteman and Doran (1993) introduces four mechanisms that drive winds within a valley, illustrated by Figure 3.5. Here the valley is oriented in a southwest-northeast direction and the graphs show the relationship between the wind flowing within the valley and the geostrophic wind flowing directly above the mountaintops. Pressure driven channeling is a valley air flow that responds to the (along-valley component of) background pressure gradient, but is forced along the valley axis. In the scenario shown in Figure 3.5 the valley wind flows either southwest or northeast and depends solely on the along-valley component of the background pressure gradient along which the geostrophic wind flows. Forced channeling arises when the winds aloft drive the valley winds below through di-

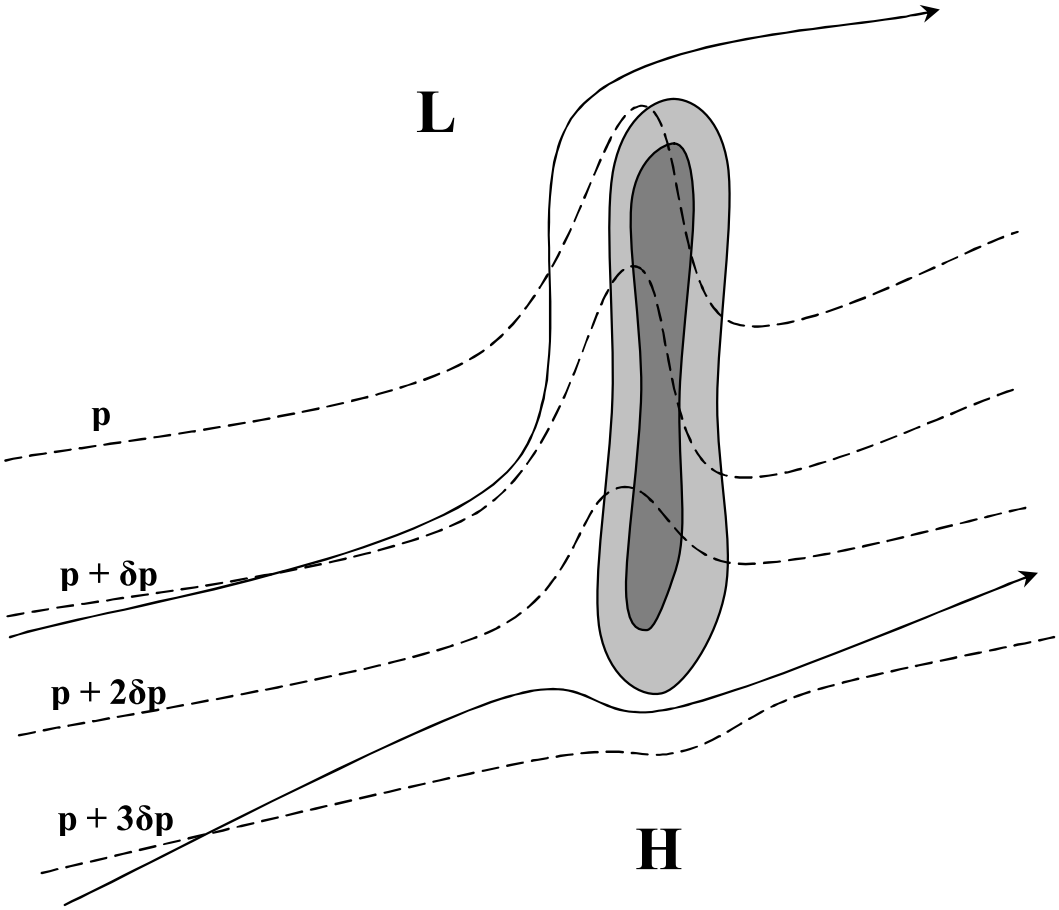

Figure 3.4: Air approaching a long ridge in the northern hemisphere. The pressure contours (i.e. isobars or height contours) are indicated by dashed lines, and streamlines by solid lines. Adapted from Smith (1982).

rect downward momentum transport, however the lower winds are still channelled along the valley axis. If this channeling effect is weak or absent (weak stratification, or a wide, shallow valley) the valley flow simply follows the driving winds aloft.

Thermally driven valley flow differs from the regimes described above in that the winds aloft exert negligible influence, being effectively decoupled from the valley flow (of course, this is the extreme case; in general, other mechanisms will play some role, and the rigorous perspective is that given by consideration of the

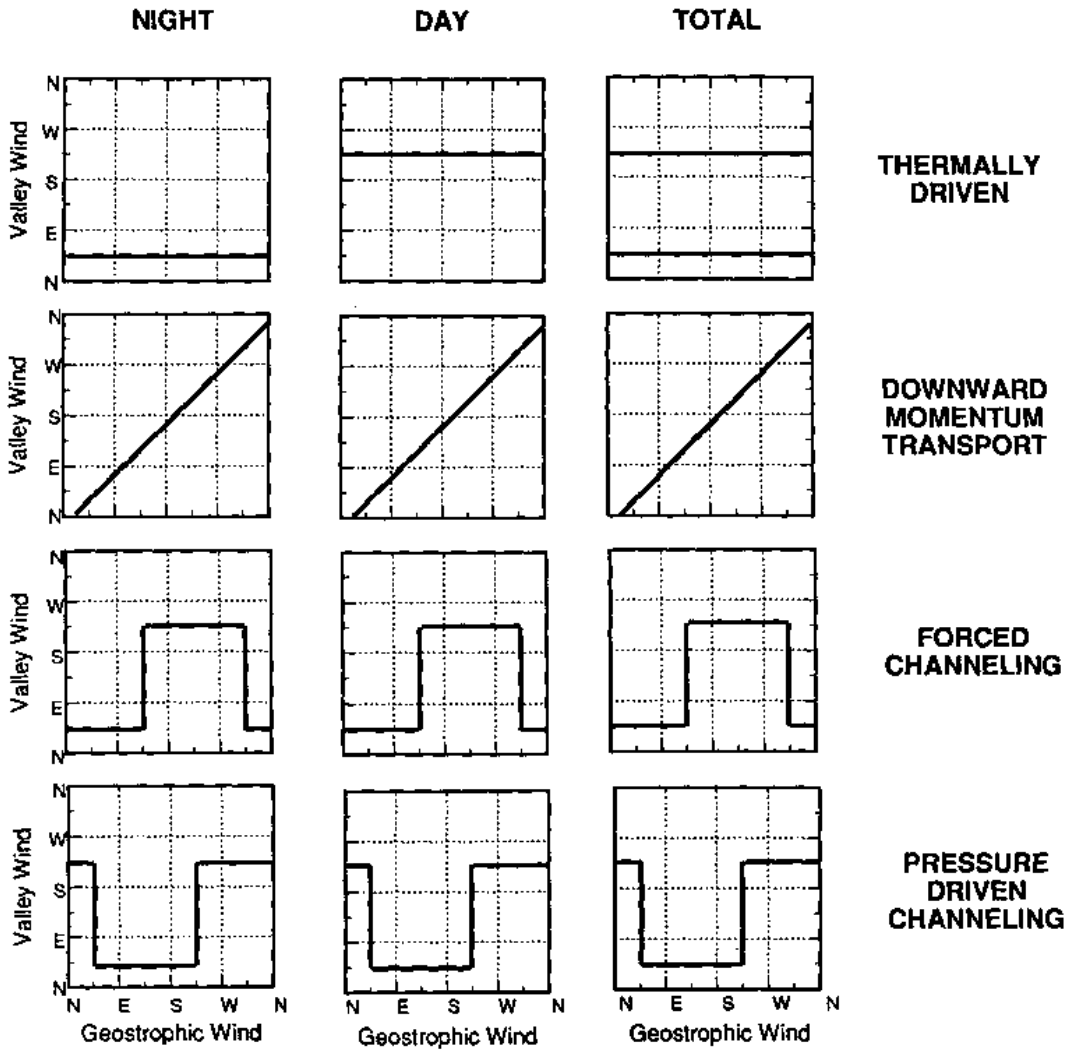

Figure 3.5: Relationship between the orientation of the overhead geostrophic wind vector and of the valley wind. The valley axis is oriented SW-NE. After Whiteman and Doran (1993).

complete force balance, these named paradigms having the danger of being a little simplistic). Examples include the downslope valley wind ('katabatic' flow, whose converse is the 'anabatic' or upslope flow), which in some situations can be very strong (Barr and Orgill 1989). A locale where the katabatic wind (modulated by other mechanisms) dominates wind climate is the mouth of the Alsek Valley (Pinard 2001), on the perimeter of the world's largest non-polar ice fields of Kluane. Here the strong summer winds are caused by a combination of katabatic winds from the valley glaciers, enhanced by forced channeling from the southwest winds aloft. The strength of the winds at the mouth of the Alsek Valley is also enhanced orographically by the constrictive gap that the valley cuts through the guarding Front Range of the ice field. In the winter the winds here become almost completely suppressed, under the strong winter inversion.

3.3. Orographically enhanced flows

The gap wind noted above is an orographic enhancement in which, from Bernoulli's Principle and the Venturi effect (see Overland and Walter 1981; Smedman and Bergström 1995), a constriction of the cross-sectional area of a pressure-driven airflow causes the wind to speed-up. A hill also causes a speed-up of the wind flowing over it as the cross-sectional area of the flow is also reduced at the hilltop. The hills that are typically studied and modelled in the context of modern boundary-layer meteorology are (only) of order 100 m high and several hundred metres in half-length (i.e. streamwise extent to the half-height point). At this scale, a flow around a hill is more sensitive to surface roughness, mean shear, turbulence, and

local stratification. As noted above the Rossby number becomes large ($\gg 1.0$) and Coriolis effect becomes less important. However the speedup that is identified in these studies is certainly a feature, too, of flow over topography on the larger scale.

At the top of a hill the speed-up zone is defined relative to the upstream undisturbed wind speed profile (which in idealized studies, is well defined; it may be as simple as a deep log layer). Troen and Petersen (1989) gives general rules regarding the speed-up zone, and shows they compare well with the observations of case studies such as Askervein Hill in the Hebrides (Taylor and Teunissen 1987; Salmon et al. 1987). Restricting (for the moment) to neutral conditions, the hilltop wind speed depends on the upstream wind speed (u_1), and the height (H), half-length (L_h) and width of the hill. Approximate expressions (Jensen et al. 1984) for the fractional increase in speed over the surface of a long ridge are

$$\Delta S = \frac{u_2 - u_1}{u_1} \simeq 2\frac{H}{L_h} \tag{3.7}$$

where the hillcrest windspeed u_2 and the upstream windspeed u_1 are specified at the same height (10 m AGL typical) above local ground level. According to Jensen et al. (1984) the maximum increase ΔS_{max} occurs at a height l determined by

$$l \simeq 0.3 \cdot z_o \left(\frac{L_h}{z_o}\right)^{0.67} \tag{3.8}$$

In the case of Askervein, the half-width W_h of the hill perpendicular to the dominant flow is larger than the length. As $W_h \gg L_h$ the ridge becomes two-dimensional and the formula above becomes more accurate.

Estimating the hilltop wind speed-up under stable stratification is much more complicated, and we must often resort to modeling. This is particularly the case

when the site of interest is located in a mountainous area such that the *upstream* (i.e. approaching) flow is affected by the nearby orography. A mountaintop above an inversion however, could effectively be treated as a hill standing above a flat plain defined by the upper boundary of a static layer of dense and strongly stratified air. Information about the upstream wind speed profile would be required, and could be derived from nearby radiosondes or from wind output of a larger (meso-) scale model.

In the context of exploration for wind energy sites, hill or mountain tops that feature steep ridges and cliffs are generally avoided, as such bluff topography is expected frequently to induce strong turbulence. A steep cliff, for example, generally cause flow to separate at the leading edge of the cliff, creating a highly turbulent zone downstream on the cliff top. This is not typically an ideal location for wind farms, as turbulence will reduce the life expectancy of the wind turbine generators.

Many observations have been made of flow over hills, and a historical review is given by Wood (2000). Some of the earliest observation campaigns directly concerning wind energy were made by Putnam (1948) in the mountains of Vermont, where attempts were made to relate hill shapes to wind speed predictions. In Israel, Frenkiel (1962) measured wind speed profiles and related them to hill shapes, noting that these were made in neutral atmospheric conditions. The first modern observations were made on Brent Knoll in Somerset (Mason and Sykes 1979). This was a roughly circular hill of moderate slope that stood 130 m above a surrounding flat plain. Measurements were intended to be made under neutral stratification to test them against the linearized flow paradigm initially developed by Jackson and

Hunt (1975), that had been extended (from 2D) to 3D flow. Many other measurement campaigns followed, including Kettles Hill (Salmon et al. 1988) (in Alberta) and Askervein (Taylor and Teunissen 1987) (in the New Hebrides). In these studies sites were chosen such that the approach flow was well defined. The exclusive focus on neutral flow was relaxed, and increasing attention was given to stable stratification; indeed a number of studies specifically focused on stably-stratified flow over hills (eg. Bradley 1983; Mason 1987; Coppin et al. 1994).

The hill flow model of Jackson and Hunt (1975) was a ground-breaking advance that served to focus research in this field. These authors adopted a highly simplified set of governing equations, deduced by a careful scale analysis and expansion in small parameters leading to a linearized (and therefore tractable) mathematical problem for the perturbation on the mean upstream wind profile induced by flow over a hill of low to moderate slope. Many hill flow studies were framed around this theory and practical applications were developed (eg. Walmsley et al. 1986; Troen and Petersen 1989). Although the linear model was numerically very efficient, it was limited to hills of moderate slope, and to a relatively small domain size, and could not handle flow separation. The evolution of faster computers allowed for the adoption of the fully non-linear equations of motion, however the turbulence closure problem remains a fundamental problem and the ultimate obstacle to the attainment of perfect predictive accuracy.

Bibliography

Arya, S. P., 2001: *Introduction to Micrometeorology*, volume 79 of *International Geophysics Series*. Academic Press, 2nd edition edition.

Barr, S. and M. M. Orgill, 1989: Influence of external meteorology on nocturnal valley drainage winds. *Journal of Applied Meteorology*, **28**, 497–517.

Barry, R. G., 2001: *Mountain Weather and Climate*. Routledge, New York, 2nd edition, 313 pp.

Bradley, E. F., 1983: The influence of thermal stability and angle of attack on the acceleration of wind up a slope. *J. Wind Eng. Indust. Aerodyn.*, **15**, 231–242.

Carruthers, D. J. and J. C. R. Hunt: 1990, *Fluid Mechanics of Airflow over Hills*, American Meteorological Society, chapter 7. 83–103.

Coppin, P. A., E. F. Bradley, and J. J. Finnigan, 1994: Measurements of flow over an elongated ridge and its thermal stability dependence: The mean field. *Boundary-Layer Meteorology*, **69**, 173–199.

Frenkiel, J., 1962: Wind profiles overhills (in relation to wind-power utilization). *Quart. J. R. Meteor. Soc.*, 156–169.

Hunt, J. and W. Snyder, 1980: Experiments on stably and neutrally stratified flow over a model three-dimensional hill. *Journal of Fluid Mechanics*, **96**, 671–704.

Jackson, P. S. and J. C. R. Hunt, 1975: Turbulent wind flow over a low hill. *Quart. J. R. Meteor. Soc.*, **101**, 929–955.

Jensen, N. O., E. L. Petersen, and I. Troen, 1984: *Extrapolation of Mean Wind Statistics with Special Regard to Wind Energy Applications.*. World Meteorological Organization Report WCP-86, WMO/TD-No. 15. WMO, Geneva.

Lackmann, G. M. and J. E. Overland, 1989: Amospheric structure and momentum balance during a gap-wind event in Shelikof Strait, Alaska. *Monthly Weather Review*, 1817–1833.

Mason, P., 1987: Diurnal variations in flow over a succession of ridges and valleys. *Quart. J. R. Meteor. Soc.*, **113**, 1117–1140.

Mason, P. J. and R. I. Sykes, 1979: Flow over an isolated hill of moderate slope. *Quart. J. R. Meteor. Soc.*, **105**, 383–395.

Overland, J. E. and B. A. Walter, 1981: Gap winds in the strait of Juan de Fuca. *Monthly Weather Review*, **109**, 2221–2233.

Pinard, J. D. J., 2001: Yukon wind energy potential, Bear Creek wind monitoring study. Technical report, Boreal Alternate Energy Centre, prepared for the Community Development Fund, Yukon Territorial Government, 16p.

Pinard, J.-P.: 2005, Wind climate of the mountainous Yukon. *New Northern Lights:*

Graduate Research on Circumpolar Studies from the University of Alberta, Canadian Circumpolar Institute.

Putnam, P. C., 1948: *Power from the Wind*. Van Nostrand, New York.

Rotach, M. W. and D. Zardi, 2007: On the boundary-layer structure over highly complex terrain: Key findings from MAP. *Q. J. R. Meteorol. Soc.*, **2007**, 937–948.

Salmon, J., H. Teunissen, R. Mickle, and P. Taylor, 1988: The Kettles Hill project: Field observations, wind-tunnel simulations and numerical model predictions for flow over a low hill. *Boundary-Layer Meteorology*, **43**, 309–343.

Salmon, J. R., A. J. Bowen, A. M. Hoff, R. Johnson, R. E. Mickle, P. A. Taylor, G. Tetzlaff, and J. L. Walmsley, 1987: The Askervein Hill project: Mean wind variations at fixed heights above ground. *Boundary-Layer Meteorolgy*, **43**, 247–271.

Smedman, A.-S. and H. Bergström, 1995: An experimental study of stably stratified flow in the lee of high mountains. *Monthly Weather Review*, 2319–2333.

Smith, R. B., 1982: Synoptic observations and theory of orographically disturbed wind and pressure. *Journal of the Atmospheric Sciences*, **39**, 60–70.

Stull, R. B., 1988: *An introduction to Boundary Layer Meteorology*. Kluwer Academic Publishers, Dordrecht, The Netherlands.

Taylor, P. and H. Teunissen, 1987: The Askervein Hill project: Overview and background data. *Boundary-Layer Meteorology*, **39**, 15–39.

Troen, I. and E. L. Petersen, 1989: *European Wind Atlas*. Riso National Laboratory, Roskilde, Denmark, 656 pp., for the Commission of the European Communities ISBN 87-550-1482-8.

Walmsley, J., P. Taylor, and T. Keith, 1986: A simple model of neutrally stratified boundary-layer flow over complex terrain with surface roughness modulations (MS3DJH/3R). *Boundary-Layer Meteorology*, **36**, 157–186.

Whiteman, C. D. and J. C. Doran, 1993: The relationship between overlying synoptic-scale flows and winds within a valley. *J. Appl. Meteor.*, **32**, 1669–1682.

Whiteman, C. D., S. Zhong, and X. Bian, 1999: Wintertime boundary layer structure in the Grand Canyon. *J. Appl. Meteor.*, **38**, 1084–1102.

Wood, N., 2000: Wind flow over complex terrain: A historical perspective and the prospect for large-eddy modelling. *Boundary-Layer Meteorology*, **96**, 11–32.

Chapter 4

Modeling the wind climate

4.1. Basic conservation principles in mesoscale flows

The foundation of any causally-based wind model is the set of conservation principles. Atmospheric flow is governed by five or more such principles, these being conservation of: the three components of momentum, air mass, and thermodynamic energy (of course, we add further conservation equations to deal with transported species such as gases and aerosols, and more importantly for water vapour and water in the liquid and ice phases; however from the perspective of wind energy climate modelling in the PBL, these laws are not needed).

a. *Equations of motion under Boussinesq approximation*

The basic state density in the lowest kilometre of the PBL varies by only about 10%, and its fluctuating component varies by only a few percent. The Boussinesq approximation assumes that the variations in the density affect the buoyancy term, but may be neglected in the inertial terms of the momentum equations. For the small amplitude vertical displacements that are expected in flow over hills, the Boussinesq approximation is always valid (Kaimal and Finnigan 1994). Naming the three Cartesian velocity components (u, v, w) for the (x, y, z) coordinates[1] respectively, the momentum equations are (from Holton 1992):

[1]These are actually expanded in a spherical coordinate system so that surface of the earth corresponds to a coordinate surface. As will be shown later, curvature terms arising out of this are insignificant for midlatitude mesoscale motions.

$$\frac{du}{dt} = -\frac{1}{\rho_o}\frac{\partial p}{\partial x} + (2\Omega v \sin\phi - 2\Omega w \cos\phi) + \frac{uv\tan\phi}{a} - \frac{uw}{a} + \nu\nabla^2 u \quad (4.1)$$

$$\frac{dv}{dt} = -\frac{1}{\rho_o}\frac{\partial p}{\partial y} - 2\Omega u \sin\phi - \frac{u^2\tan\phi}{a} - \frac{vw}{a} + \nu\nabla^2 v \quad (4.2)$$

$$\frac{dw}{dt} = -\frac{1}{\rho_o}\frac{\partial p}{\partial z} + 2\Omega u \cos\phi + g\frac{\theta}{\theta_o} + \frac{u^2+v^2}{a} + \nu\nabla^2 w \quad (4.3)$$

In these equations the operator d/dt occurring on the left side is the Lagrangian (also known as 'total' or 'material') derivative, and can be expanded

$$\frac{d}{dt} = \frac{\partial}{\partial t} + u\,\frac{\partial}{\partial x} + v\,\frac{\partial}{\partial y} + w\,\frac{\partial}{\partial z} \quad (4.4)$$

into the sum of the local tendency in time and the advective terms. The first term on right side of each equation is the pressure gradient, and courtesy of the Boussinesq approximation entails a constant density ρ_o; p is not the total pressure, but the pressure *departure* from the hydrostatic and adiabatic reference state. Terms involving Ω (earth's rate of rotation) are Coriolis terms (ϕ is the latitude). The influence of buoyancy is felt only in the w-momentum Equation (4.3), where g is gravity and θ is the departure of potential temperature from the reference state (θ_o is in principle the mean value for the layer). Terms involving $1/a$ are curvature terms accounting for the earth's spherical surface, and finally terms with ν represent the friction arising from the divergence of viscous momentum fluxes.

The exact statement of conservation of air mass (the "continuity equation") is:

$$\frac{\partial\rho}{\partial t} + \frac{\partial\rho u}{\partial x} + \frac{\partial\rho v}{\partial y} + \frac{\partial\rho w}{\partial z} = 0 \quad (4.5)$$

However under the Boussinesq approximation the velocity field is non-divergent

and the continuity equation simplifies to

$$\nabla \cdot \vec{u} \equiv \frac{\partial u}{\partial x} + \frac{\partial v}{\partial y} + \frac{\partial w}{\partial z} = 0 \tag{4.6}$$

b. *Scale Analysis*

The Froude and Rossby numbers that were defined earlier are dimensionless scale factors that appear in the governing equations when these are re-expressed in dimensionless form: the specific values (or ranges) of the Froude and Rossby numbers delineate parameter (or flow) regimes in which differing force balances dictate the flow. Generally speaking, the appearance in the momentum equations of these scale factors provides an invitation to a 'scale analysis' which may allow us (provisionally) to eliminate certain terms, thereby simplifying the equations of motion pertaining to a specific orographic flow (or class of flows) of particular interest. In mountain flows, we define the following characteristic scales of the flow field, based on observed values in the flow *well above* Southern Yukon mountains.

- $U \sim 10\ \mathrm{m\,s^{-1}}$, horizontal velocity scale
- $W \sim 0.1\ \mathrm{m\,s^{-1}}$, vertical velocity scale (note: this is untrue on the local scale, very close to the mountains)
- $H \sim 1000$ m, depth scale
- $L \sim 100\ \mathrm{km} = 10^5$ m, length scale
- $f \sim 10^{-4}\ \mathrm{s^{-1}}$, Coriolis parameter

- $\nu \sim 10^{-5}\ \mathrm{m^2\,s^{-1}}$, kinematic viscosity
- $\delta P/\rho_o \sim 10^{3}\ \mathrm{m^2\,s^{-2}}$, horizontal pressure fluctuation scale
- $a \sim 10^{7}$ m, earth radius

The horizontal pressure fluctuation δP is normalized by the density ρ_o in order to estimate a scale valid within the PBL. Following Holton (1992) it is equal to the magnitude of the fluctuation of the geopotential of an isobaric surface. Table 4.1 shows the characteristic magnitude of each term in Equation (4.1) and Equation (4.2), based on the above scalings.

Table 4.1: Scale analysis of the horizontal momentum equations.

	accel.	pres.	Coriolis	Coriolis	curv.	curv.	fric.
x-Eq.	$\frac{du}{dt}$	$= -\frac{1}{\rho_o}\frac{\partial p}{\partial x}$	$+2\Omega v \sin\phi$	$-2\Omega w \cos\phi$	$+\frac{uv\tan\phi}{a}$	$-\frac{uw}{a}$	$+\nu\nabla^2 u$
y-Eq.	$\frac{dv}{dt}$	$= -\frac{1}{\rho_o}\frac{\partial p}{\partial y}$	$-2\Omega u \sin\phi$		$-\frac{u^2\tan\phi}{a}$	$-\frac{vw}{a}$	$+\nu\nabla^2 v$
Scales	$\frac{U^2}{L}$	$\frac{\delta P}{\rho_o L}$	fU	fW	$\frac{U^2}{a}$	$\frac{UW}{a}$	$\frac{\nu U}{H^2}$
$\mathrm{m\,s^{-1}}$	10^{-3}	10^{-2}	10^{-3}	10^{-5}	10^{-5}	10^{-7}	10^{-10}

Retaining only the terms that are of order 10^{-3} or larger, the horizontal equations reduce to:

$$\frac{du}{dt} \approx -\frac{1}{\rho_o}\frac{\partial p}{\partial x} + fv\ ,\ \frac{dv}{dt} \approx -\frac{1}{\rho_o}\frac{\partial p}{\partial y} - fu \tag{4.7}$$

where the Coriolis parameter $f = 2\Omega\sin\phi$. Note that as the length scale L decreases the local and advective acceleration and pressure terms increase in significance, such that the Coriolis term becomes less significant.

For the vertical component of momentum (Eq. 4.3) we can perform a similar scale analysis, as shown in Table 4.2.

Table 4.2: Scale analysis of the vertical momentum equation.

	accel.	pres.	Coriolis	gravity	curv.	fric.
z-Eq.	$\frac{dw}{dt}$	$= -\frac{1}{\rho_o}\frac{\partial p}{\partial z}$	$-2\Omega u \cos\phi$	$g\frac{\theta}{\theta_o}$	$+\frac{u^2+v^2}{a}$	$+\nu\nabla^2 w$
Scales	$\frac{UW}{L}$	$\frac{P_o}{\rho_o H}$	fU	g	$\frac{U^2}{a}$	$\frac{\nu W}{H^2}$
$\mathrm{m\,s^{-1}}$	10^{-3}	10	10^{-5}	10	10^{-5}	10^{-12}

The vertical momentum equation reduces to:

$$\frac{1}{\rho_o}\frac{\partial p}{\partial z} = g\frac{\theta}{\theta_o} \tag{4.8}$$

As noted earlier p is the pressure *departure* from the hydrostatic and adiabatic reference state. As the length scale L decreases the acceleration term in Table 4.2 becomes more important, particularly near orographic slopes where W increases.

c. *Reynolds Averaging of the Navier-Stokes Equations*

The atmosphere is a continuum, in motion on a vast range of length scales. We will never have a clear knowledge of state of motion at every point and at every instant in time. So it becomes necessary to explicitly define what are the "resolved" and "unresolved" scales of motion, and to approximate the influence of the unresolved scales on the resolved. Most naturally, we may choose to define the resolved flow in terms of space- and/or time-averaged flow variables, e.g. the resolved synoptic-

scale vertical velocity might be defined

$$\overline{w}(x,y,z,t) = \frac{1}{L^2}\int_{x-L/2}^{x+L/2}\int_{y-L/2}^{y+L/2} w(x',y',z,t)\,dx'\,dy' \tag{4.9}$$

and (since we have elected $L \sim 100$ km) is a far 'smoother' function of position and time than the 'raw' vertical velocity.

Now without further elaboration of the averaging operation (whose specifics are irrelevant), let's consider that all flow variables can be decomposed into the sum of their average and a local deviation from the average. For example the velocity u_i decomposes into its mean $\bar{u}_i$ and the deviation u_i' from the average, i.e. $u_i = \bar{u}_i + u_i'$. (Terminology: the mean or average $\bar{u}_i$ is the "resolved velocity" and the deviation or fluctuation u_i' is the unresolved velocity).

Although it may be tempting to regard the unresolved velocity field as merely a local detail, in general this is untrue: far from being unimportant, the unresolved field may play (and generally near terrain *does* play) an important role in the time-space evolution of the resolved fields. Unfortunately, while (as we see below) it is possible to write a formal statement of this influence, we arrive at an unclosed system of equations and it becomes necessary to introduce a "parameterisation" of the influence of unresolved scales, a so-called "turbulence closure model", which is formulated in terms of statistics of u_i'. In the first order closure, the influence of the unresolved turbulence eddies is treated as equivalent to an increased effective viscosity of the fluid. In contrast, a higher order closure consists of a set of differential equations for statistics of the unresolved motion, these being derived from the Navier-Stokes equation themselves.

The averaged form of the conservation Equations (4.7) and (4.8)[2] is obtained by substituting $u_i = \bar{u}_i + u_i'$ and averaging[3]. The resulting equations are:

$$\frac{d\bar{u}}{dt} = -\frac{1}{\rho_o}\frac{\partial \bar{p}}{\partial x} + f\bar{v} - \left[\frac{\partial \overline{u'u'}}{\partial x} + \frac{\partial \overline{u'v'}}{\partial y} + \frac{\partial \overline{u'w'}}{\partial z}\right] \tag{4.10}$$

$$\frac{d\bar{v}}{dt} = -\frac{1}{\rho_o}\frac{\partial \bar{p}}{\partial y} - f\bar{u} - \left[\frac{\partial \overline{v'u'}}{\partial x} + \frac{\partial \overline{v'v'}}{\partial y} + \frac{\partial \overline{v'w'}}{\partial z}\right] \tag{4.11}$$

$$\frac{d\bar{w}}{dt} = -\frac{1}{\rho_o}\frac{\partial \bar{p}}{\partial z} + g\frac{\bar{\theta}}{\theta_o} - \left[\frac{\partial \overline{w'u'}}{\partial x} + \frac{\partial \overline{w'v'}}{\partial y} + \frac{\partial \overline{w'w'}}{\partial z}\right] \tag{4.12}$$

and

$$\frac{\partial \bar{u}}{\partial x} + \frac{\partial \bar{v}}{\partial y} + \frac{\partial \bar{w}}{\partial z} = 0 \tag{4.13}$$

Equations 4.10 to 4.12 retain the local tendency $\partial/\partial t$ – these are sometimes referred to as unsteady Reynolds-averaged Navier-Stokes equations (URANS), but here denoted RANS. The terms in the square brackets represent the divergences of turbulent fluxes of momentum, and state explicitly and specifically the influence of the unresolved scales on the resolved flow ($\bar{u}_i$). They may legitimately be termed "turbulent friction" (and in the crudest and least physical of parameterizations, are replaced by 'Rayleigh friction' terms, e.g. $d\bar{u}/dt = ... - \alpha_u \bar{u}$). Mathematically they have the form of spatial gradients of various turbulent velocity variances and covariances. Collectively, these variances and covariances define the Reynolds stress tensor $R_{ij} = \overline{u_i' u_j'} = -\tau_{ij}/\rho$, a matrix (or rank-2 tensor) composed of the shear stresses (off-diagonal components) and normal stresses (diagonal components). In the PBL, ordinarily the magnitudes of the turbulent flux divergence terms are of the same order as the other terms in Equations (4.10) - (4.12), and so

[2]including the vertical acceleration

[3]The rules for Reynolds averaging are well-known, and are given (for example) by Kaimal and Finnigan (1994).

these terms cannot be neglected.

The effects of the unresolved scales, i.e. the unknown terms in brackets, need to be accounted for by some approximation - which will constitute a "turbulence closure scheme." One such scheme[4] is "K-theory" in which turbulent fluxes are taken to be "driven" by the gradient (spatial inhomogeneity) in a relevant mean property: for example the Boussinesq closure for the Reynolds stress tensor is

$$\overline{u_i' u_j'} = -K \left(\frac{\partial \overline{u_i}}{\partial x_j} + \frac{\partial \overline{u_j}}{\partial x_i} \right) + \frac{2}{3} k \, \delta_{ij} \tag{4.14}$$

where k is the turbulent kinetic energy (TKE), defined

$$k = \frac{1}{2} \left(\overline{u'^2} + \overline{v'^2} + \overline{w'^2} \right), \tag{4.15}$$

and where $K \gg \nu \, [\mathrm{m}^2 \, \mathrm{s}^{-1}]$ is the eddy viscosity. For the most important component of the shear stress, this states

$$\overline{u'w'} = -K \left(\frac{\partial \bar{u}}{\partial z} + \frac{\partial \bar{w}}{\partial x} \right) \tag{4.16}$$

Note that K-theory represents turbulent convection by the unresolved scales as if it were a *diffusion* process, although generally the eddy viscosity/diffusivity is treated as depending on both position, and on the scale and intensity of turbulence: unlike the almost infinitely smaller natural viscosity, it is *not* a simple property of the fluid.

d. *Applications of the Navier-Stokes and the Reynolds equations*

In principle the Navier-Stokes equations could be numerically solved without need of any turbulence model, provided the entire spectral range of spatial and temporal

[4]The original enunciation of K-theory lies in the work of Boussinesq, St. Venant, Prandtl and Taylor.

scales of the turbulence were resolved. This approach is known as direct numerical simulation (DNS), but typically cannot be used to simulate PBL flows because it would necessitate a prohibitively fine grid and time step, demanding excessive computing capacity: DNS can only be used for relatively low Reynolds-number flows (where inertial forcings are small relative to viscous forcings).

An alternative to this approach is to invoke the (unsteady) Reynolds-averaged Navier-Stokes (RANS) equations, i.e. suitably averaged equations of motion for turbulent fluid flow supplemented by a turbulence closure. The RANS model parameterizes the turbulent fluxes such that the model is formulated in terms of mean fields.

The Large Eddy Simulation (LES) approach sits in between the DNS and the RANS models: it calculates explicitly the instantaneous large scale motions, while parameterizing the influence of all those motions that are smaller than the mesh resolution. It is also known as spatially filtered Navier-Stokes equations with a 'sub-grid scale (SGS)' modelling of turbulence. LES is in principle more accurate than RANS, given sufficient resolution, but requires that a time-varying velocity field be provided/imposed at inflow boundaries of the flow domain (See Bechmann et al. 2007, for further discussion). This is a considerable complication (often overcome by the device of using periodic boundary conditions, which are not appropriate in the context of flow in mountainous terrain). A second major issue prohibiting practical application of LES is its large memory and computing time requirements.

In addition to these computational difficulties, while in principle LES simulations should be more accurate than RANS, accuracy is lesser near solid sur-

faces, where an increasing fraction of the TKE is unresolved (loosely speaking, this is because, as the wall is approached, eddy size approaches zero even when the Reynolds number is not small). This renders pure LES of high Reynolds number wall-bounded flows difficult or impossible (Franke et al. 2007). It is, however, possible to adopt a hybrid approach, using RANS at the surface coupled with LES away from the wall.

4.2. The Anemoscope toolkit

Anemoscope is based on a statistical-dynamical downscaling approach (Frey-Buness et al. 1995; Frank and Landberg 1997; Frank et al. 2001). This approach involves using a mesoscale model in RANS mode with a given large-scale climate and the regional topography to calculate a distribution of climatological fields. The basic assumption is that the regional climate is associated with a specific frequency distribution of basic large-scale weather situations (or classes). In Anemoscope the downscaling procedure consists of four major steps that begin with the classification of a global climate database (eg. NCEP/NCAR Reanalysis) into a basic set of weather situations. Each class (weather situation) is used to initialize and set the boundary conditions for a mesoscale model (eg. MC2). The simulation results are weighted by the frequency of occurrence of each class and are also categorised into a frequency distribution of wind by direction and speed intervals. This new database can be used then to run microscale (eg. MSMicro) simulations that compute local wind deviations due to local terrain forms (ie. hills) and surface roughness. The final statistical results are interpreted for evaluating wind energy systems.

The study detailed in Chapter 5 uses all four steps in an attempt to simulate the wind climate in a steep mountainous terrain. In Chapter 6 however, it is evident that it is the mesoscale phenomenon that requires focus with regard to wind flow simulation in complex terrain. In Chapter 7 it is first two steps in Anemoscope that are given most importance: the NCEP/NCAR Reanalysis and the MC2 mesoscale model. These are described in some detail in the following subsections.

a. *The NCEP/NCAR Reanalysis*

Within the last decade global climate databases such as those by ECMWF (European Centre for Medium-range Weather Forecasting) (Gibson et al. 1997) and NCEP/NCAR (National Centers for Environmental Prediction/National Center for Atmospheric Research)(Kalnay et al. 1996) have appeared. These databases, which contain climate information such as wind, temperature, and humidity, are the result of huge reanalysis efforts carried out by their respective institutions. The global long-term dataset used as input and boundary conditions for MC2 is the NCEP/NCAR Reanalysis. NCEP/NCAR Reanalysis (called Reanalysis hereafter) is chosen due to its global coverage, its relatively uniform quality both in space and time (Landberg et al. 2003), and its free public access. The Reanalysis data used in the MC2 input is from a 43-year period (1958-2000) at a resolution of 2.5 degrees of latitude-longitude grid spacing and 17 pressure levels in vertical (from 1000 to 10 mb).

At mid-latitudes the near-surface wind is mainly influenced by the pressure

gradient, thermal stratification, terrain shape (elevation and orientation), and surface roughness. The geostrophic wind is a useful paradigm for the wind outside the boundary layer: it is linked to the large-scale pressure gradient through the geostrophic balance and its vertical variation is related to the horizontal variation of potential temperature.

The pressure fields from the Reanalysis are converted (by RPN) to (equivalent) geostrophic winds using an interpolation of pressure, temperature, and humidity. The method works as follows: since only the near-surface wind is of interest to wind energy calculations, the nominated pressure levels are 1000, 850, 700 and 500 mb, which correspond nominally to 0, 1500, 3000, and 5500 m ASL as used in the model. The meteorological parameters in the Reanalysis are interpolated to these four nominated pressure levels. At each nominated height the pressure is interpolated using a hydrostatic approximation. And at each nominated pressure the temperature and humidity are interpolated to the pressure values obtained from the hydrostatic approximation. The geostrophic wind is then calculated using the interpolated pressure, temperature and humidity at the 4 nominated heights. The geostrophic wind is calculated using the following relations:

$$f\ \mathbf{V}_g = \mathbf{k} \times \frac{1}{\rho}\ \nabla p \tag{4.17}$$

and $p = \rho R_d T_v$ where T_v is the virtual temperature $T_v = T \cdot (1 + 0.61 \cdot r)$ with r being the water-vapor mixing ratio so that:

$$f\ \mathbf{V}_g = \mathbf{k} \times \frac{R_d T_v}{p}\ \nabla p \tag{4.18}$$

The weather situations (classes) are classified according to the geostrophic wind

direction and speed at 0 m ASL, and the vertical shear of wind-speed between 0 and 1500 m ASL. The geostrophic wind direction is classified into 16 sectors, and each sector is divided into 14 speed classes (with class limits as: 2, 4, 6, 8, 10, 12, 14, 16, 18, 22, 26, 30, and $>$ 34 m/s). Each class of a sector and speed interval is then divided into two classes according to the sign (positive or negative) of vertical shear, except for the smallest wind-speed interval. There is a maximum of 432 possible classes. These classes can also be further subdivided into four seasonal variations and these (seasonally sub-divided) classes have recently been included with the Anemoscope toolkit, but they greatly increase computation requirements.

The winds (from each Reanalysis profile) are initially treated as geostrophic and used to set the horizontal pressure gradient at all levels in the entire MC2 model domain, a procedure that is described below.

b. *MC2 in the EOLE mode*

The numerical formulation of the MC2 (Mesoscale Compressible Community) dynamical kernel was first developed by Robert (1969). MC2 in its fullest capacity is a limited area model (LAM) based on the compressible, non-hydrostatic Navier-Stokes equations solved with a semi-implicit and semi-Lagrangian (SISL) numerical integration scheme. The atmospheric variables are discretized on an Arakawa C-type staggered grid on a polar-stereographic projection in the horizontal and on Gal-Chen (Gal-Chen and Somerville, 1975) terrain-following scaled height coordinate in the vertical. The SISL scheme allows longer time steps (at least by a factor

of 3) compared with other non SISL at the same spatial resolution. A description of MC2 is found in Bergeron et al. (1994) and Laprise et al. (1995).

For wind climate modelling (within the Anemoscope toolkit) pertaining to the present thesis, MC2 is used in a diagnostic mode with simplified model physics ("EOLE" mode, also see Yu et al. 2006, for complete description), i.e. all or most of the supplementary computations that would be required for weather forecasting (e.g. solar and atmospheric radiation, budgets of water in all its phases) are suppressed. The time-dependent term (e.g. $\partial\bar{u}/\partial t$, where in EOLE mode $\bar{u}$ represents the long time/large volume mean velocity, all turbulent scales of motion having been eliminated by the averaging) is still included: however the model is run to steady state before the output variables are analyzed. Neglecting microphysical (and other thermodynamic) processes allows fast convergence to this steady state, however the obvious penalty is that the diurnal cycle cannot be simulated — and nor, evidently, can such effects as the sea/lake breeze and mountain/valley (kata- and anabatic) circulation be accommodated.

In the MC2-EOLE mode the vertical profile from each Reanalysis class described in the previous subsection is set at the centre of the model domain as an initial condition. For the balance of the grid points the initial condition is obtained (starting without topography) from a hydrostatic and geostrophic initial state. The

equations take the form (see Yu et al. 2006, for development):

$$(1+\frac{b}{g})\frac{\partial P}{\partial X} = fV - K_e\frac{\partial S}{\partial X} \quad (4.19)$$

$$(1+\frac{b}{g})\frac{\partial P}{\partial Y} = -fU - K_e\frac{\partial S}{\partial Y} \quad (4.20)$$

$$(1+\frac{b}{g})\frac{\partial P}{\partial z} = b \quad (4.21)$$

These equations are projected on a sphere with no topography, with conformal coordinates X and Y. Details of this coordinate system are found in Tanguay et al. (1990). The buoyancy $b = gT'/T^*$ and the generalized pressure $P = RT^*(\ln p)'$. The perturbation components of temperature and pressure from basic state are $T' = T - T^*$, $(\ln p)' = \ln(p/p^*)$. The basic states $T^*(z)$ and $p^*(z)$ are hydrostatically related through $\partial \ln p^*/\partial z = -g/RT^*$ (Girard et al. 2005). The expression K_e is a pseudo kinetic energy per unit mass $K_e = (U^2 + V^2)/2$, and the term it occurs in arises from curvature terms in the conversion from the Cartesian to the conformal coordinate system. The variable S is a map scale where $\sqrt{S} = (1 + \sin\phi_o)/(1 + \sin\phi)$ and ϕ_o is a reference latitude for the polar stereographic conformal transformation. The components (U, V) are wind images in projected (X, Y) coordinates.

To initialise the model, at the centre of the domain the temperatures and geostrophic winds at the four heights 0, 1500, 3000, 5500 m ASL, are cubically interpolated to the model levels (28 levels) up to 5500 m ASL. Above this height, up to 20 km, the profiles are kept constant.

Using the temperature (buoyancy b) profile at the centre of the domain, a generalized pressure P profile is calculated by numerically integrating Equation 4.21

in the vertical. The full horizontal distribution of pressure is then determined by numerically integrating Equations 4.19 and 4.20 between the domain centre and its edges. Horizontal uniformity of the geostrophic wind is maintained throughout. The temperature profiles away from the central profile are obtained through iteration, using Equation 4.21 again. Away from the centre the temperature profiles are slightly different from the one at the centre, but they satisfy the geostrophic balance in the model.

The model starts with this initial condition and with the lateral boundary conditions kept constant in time.

For the model simulation Equations 4.19 to 4.21 above are embellished with more terms, because in the planetary boundary layer (PBL) the effects from orography (to be grown as simulation time proceeds) and surface friction induce an ageostrophic component of flow. Suitably generalized equations of motion are:

$$\frac{dU}{dt} + (1+\frac{b}{g})\frac{\partial P}{\partial X} = fV - K_e\frac{\partial S}{\partial X} + F_U \tag{4.22}$$

$$\frac{dV}{dt} + (1+\frac{b}{g})\frac{\partial P}{\partial Y} = -fU - K_e\frac{\partial S}{\partial Y} + F_V \tag{4.23}$$

$$\frac{dw}{dt} + (1+\frac{b}{g})\frac{\partial P}{\partial z} = b + F_w \tag{4.24}$$

The local tendency and advective terms are now included and in the transformed coordinate system the total derivative is interpreted as:

$$\frac{d}{dt} \equiv \frac{\partial}{\partial t} + S\left(U\frac{\partial}{\partial X} + V\frac{\partial}{\partial Y}\right) + w\frac{\partial}{\partial z} \tag{4.25}$$

The expressions $F_{U,V,w}$ are the eddy forcing terms due to subgrid-scale physical processes that are unresolvable by the model dynamics. Included in the physics

(see Mailhot et al. 1998, for greater details on the full physics package) are the turbulent kinetic energy equation, whose solution k forms the basis for specifying an eddy viscosity/diffusivity used to compute the vertical "eddy diffusion" of momentum (Benoit et al. 1989), and surface layer exchanges (Georgelin et al. 1994). The surface temperature is kept constant (in time) and tied to the temperature profile, i.e. the elevated surface has the same temperature as the air temperature at the given elevation. Hence there is no surface heat exchange.

c. *Earlier studies of flow on hills/mountains using MC2*

MC2 has been used in several studies of complex topography, ranging from an idealized hill to observed mountainous terrain flows. Some of these earlier studies will be briefly described here.

The MC2 model has been tested on simple 2D mountains (Pinty et al. 1995) of various shapes under different atmospheric conditions. Of particular interest was its testing in an isothermal reference state to create a statically stable flow over a steep-sloped (semi-cylindrical) mountain. The Froude number in the test case was $F = 0.8$, no flow separation was evident (2D flow), and lee side downslope velocities that exceeded twice the approach wind speed resulted from the simulations. In their conclusions these authors noted their intention to investigate low-Froude number flows around isolated 3D obstacles. However no follow-up MC2 studies by these authors (Pinty et al. 1995) have been found to date (also confirmed by Benoit, pers. comm.).

The west shores of Cape Breton experience downslope wind storms similar to those occurring on the lee of the Rockies, and other mountain ridges around the world. The Cape Breton Highlands rise about 500 m above the surrounding sea, and are elongated in a southwest-northeast fashion at the north end of Nova Scotia. MC2 has been used to simulate the downslope wind storm that results from the "suete" (Benoit et al. 1997), an Acadian term for a strong southeasterly wind. The suete occurs when a low pressure system is in place over the northeastern United States. The MC2 model was successful in simulating the downslope wind storm on the lee of the Highlands. The Froude number for this simulation was $F = 2$, and the atmosphere was weakly stable with $N = 0.015$.

MC2-EOLE has been tested in the Gaspé region, as part of the toolkit WEST (Wind Energy Simulation Toolkit; now called Anemoscope) Yu et al. (2006). It was run at 5-km resolution and the results from MC2-EOLE were used in the microscale portion MS-Micro (see next chapter for description) which was run at 200-m resolution. Much of the Gaspé region is below 600 m ASL, with one peak at over 1000 m in the northwest central portion of the peninsula. Computed windspeeds were compared with observations from 29 meteorological stations, with tower heights of 40 m AGL: the average measured wind speed was 6.6 $\mathrm{m\,s^{-1}}$. The winds in this region were simulated with reasonable success, there being an overall underestimation of windspeed by about 0.5 $\mathrm{m\,s^{-1}}$. The mean absolute difference was 0.83 $\mathrm{m\,s^{-1}}$. The authors of the study noted that the model resolution was rather coarse relative to the complexity of the region's terrain, and that implementation with a finer spatial resolution should improve the model outcome.

The MC2 has also been used in real-time NWP mode to test against measurements made during the Mesoscale Alpine Programme (MAP) in the Alps (Benoit et al. 2002). One particularly interesting study was in the Wipptal Valley, where gap winds occur. MC2 was able to simulate a measured gap wind event, even though the valley was only three grid points across (with a 3-km horizontal resolution). The measured and modelled maximum wind speeds in the gap were comparable, at 12 $\mathrm{m\,s^{-1}}$, and the height of occurrence of the maximum windspeed was at mid-valley elevation. MC2 also simulated a strong horizontal wind on a downwind and downslope portion of this valley. No information was given about the atmospheric (stability) condition during this gap wind occurrence.

4.3. How MC2 is used in the balance of the thesis

In Chapter 5 (Pinard et al. 2005) the MC2-EOLE model was used as part of the Anemoscope toolkit[5] to compare wind climate simulations to measurements in the southern Yukon. A total of 162 separate simulations (based on NCEP/NCAR Reanalysis) accounting for each wind climate condition were made at the RPN laboratory in Montreal. Most of the standard settings, including the Reanalysis input, that were used to develop the Canadian Wind Atlas were also used to simulate the mesoscale winds in this case study. At this stage the MC2 model did not reduce or rotate the sea level boundary winds, in contrast with the later practise case when it was used in Chapter 7. The resulting outputs were assimilated into a single set of (joint) mean wind speed - mean wind direction distributions (a set for each of the

[5]Called WEST at the time of the study; both the meso- and microscale output were produced.

meso- and microscale outputs) and were sent to me to analyze and compare with my measurements. In this study the Reanalysis was compared to the measurements to identify that there are some interesting discrepancies. In concluding this study it was evident that further detailed analysis of the MC2 input and output was necessary, however, this also required a more in-depth study of the wind climate of the Whitehorse area.

Chapter 6 (Pinard 2007) explores the phenomenon of wind climate in mountainous terrain by reviewing related valley wind studies and analysing the measurements available in a smaller, more focused Whitehorse area. A detailed analysis was made of the Whitehorse radiosondes to extract: long-term trends in wind speed and temperature; seasonal variations; and profiles of the wind speed, direction and temperature in and above the valley. Wind measurements from several surface stations on mountaintops and valley bottoms were also used to confirm the observations by the radiosondes. This chapter identifies the important forcing mechanisms that control the mountain wind climate of the Whitehorse area. It also emphasizes the importance of stratification and its effect on the wind climate. This provides the necessary knowledge that is applied to the next MC2 study, outlined in Chapter 7.

Chapter 7 (in press at time of submission of this thesis: Pinard 2008) focuses on identifying how the MC2-EOLE model behaves in a steep mountainous terrain using only single climate input profiles as opposed to the 287 (presently available for Whitehorse region) wind climate classes derived from the Reanalysis. Two input wind climate profiles are proposed for this study: one represents a summary of the 287 Reanalysis wind climates; the other represents a wind climate that has wind

speed and direction and temperature profile based on the Whitehorse radiosondes. For this study I received permission to use the model in-house. This allowed much greater control in simulating individual wind climate inputs to test the MC2 model sensitivity. The inputs into MC2 were greatly simplified by running a single profile of mean wind in order to allow a critical analysis of the output. This provided further insight into the MC2's behavior that had not been explored in Chapter 5.

Bibliography

Bechmann, A., N. N. Sørensen, and J. Johansen, 2007: Atmospheric flow over terrain using hybrid RANS/LES. Technical report, Risø National Lab., Roskilde, Denmark.

Benoit, R., J. Cote, and J. Mailhot, 1989: Inclusion of a TKE boundary layer parameterization in the Canadian regional finite-element model. *Mon. Wea. Rev.*, **117**, 1726–1750.

Benoit, R., M. Desgagne, P. Pellerin, S. Pellerin, Y. Chartier, and S. Desjardins, 1997: The Canadian MC2: A semi-lagrangian, semi-implicit wideband atmospheric model suited for finescale process studies and simulation. *Mon. Wea. Rev.*, **125**, 2382–2415.

Benoit, R., C. Schär, P. Binder, S. Chamberland, H. C. Davies, M. Desgagné, C. Girard, C. Keil, N. Kouwen, D. Lüthi, E. M. D. Maric, P. Pellerin, J. Schmidli, F. Schubiger, C. Schwierz, M. Sprenger, A. Walser, S. Willemse, W. Yu, and E. Zala, 2002: The real-time ultrafinescale forecast support during the special observing period of the MAP. *Bull. Amer. Meteor. Soc.*, **83**, 85–109.

Bergeron, G., L. Laprise, and D. Caya, 1994: Formulation of the mesoscale com-

pressible community (MC2) model. Technical report, Cooperative Centre for Research in Mesometeorology, 550 Sherbrooke West Montreal H3A 1B9, internal Report.

Frank, H., O. Rathmann, N. Mortensen, and L. Landberg, 2001: The numerical wind atlas - the KAMM/WAsP method. Technical Report Risø-R-1252(EN), Risø National Laboratory, Roskilde, Denmark.

Frank, H. P. and L. Landberg, 1997: Modelling the wind climate of Ireland. *Boundary Layer Meteorology*, **85**, 359–378.

Franke, J., A. Hellsten, H. Schlünzen, and B. Carissimo, 2007: Best practice guideline for the CFD simulation of flows in the urban environment. Technical report, Meteorological Institute Centre for Marine and Atmospheric Sciences.

Frey-Buness, A., D. Heimann, and R. Sausen, 1995: A statistical-dynamical downscaling procedure for global climate simulation. *Thoer. Appl. Climatol.*, **50**, 117–131.

Georgelin, M., E. Richard, M. Petitdidier, and A. Druilhet, 1994: Impact of subgrid-scale orography parameterization on the simulation of orographic flows. *Mon. Wea. Rev.*, **122**, 1509–1522.

Gibson, R., P. Kallberg, and S. Uppala, 1997: The ECMWF re-analysis (ERA) project. *ECSN Newsletter*, **5**, 11–21.

Girard, C., R. Benoit, and M. Desgagné, 2005: Finescale topography and the MC2 dynamics kernel. *Mon. Wea. Rev.*, **133**, 1463–1477.

Holton, J. R., 1992: *An Introduction to Dynamic Meteorology*. Academic Press, third edition edition.

Kaimal, J. C. and J. J. Finnigan, 1994: *Atmospheric Boundary Layer Flows: Their structure and measurement*. Oxford University Press, New York.

Kalnay, E., M. Kanamitsu, R. Kistler, W. Collins, D. Deaven, L. Gandin, M. Iredell, S. Saha, G. White, J. Woollen, Y. Zhu, A. Leetmaa, R. Reynolds, M. Chelliah, W. Ebisuzaki, W. Higgins, J. Janowiak, K. C. Mo, C. Ropelewski, J. Wang, R. Jenne, and D. Joseph, 1996: The NCEP/NCAR 40-year Reanalysis project. *BAMS*, **77**, 437–471.

Landberg, L., L. Myllerup, O. Rathmann, E. L. Petersen, B. H. Jorgensen, J. Badger, and N. G. Mortensen, 2003: Wind resource estimation – an overview. *Wind Energy*, **6**, 261–271.

Laprise, R., D. Caya, G. Bergeron, and M. Giguère, 1995: The formulation of the André Robert MC2 (Mesoscale Compressible Community) model. *Atmos.-Ocean*, **35**, 195–220.

Mailhot, J., S. Bélair, R. Benoit, B. Bilodeau, Y. Delage, L. Fillion, L. Garand, C. Girard, and A. Tremblay, 1998: Scientific description of RPN physics library - version 3.6. Technical report, Recherce en Prévision Numérique, Atmospheric Environment Service, 197 pp.

Pinard, J. D. J.-P., R. Benoit, and W. Yu, 2005: A WEST wind climate simulation of the mountainous Yukon. *Atmosphere-Ocean*, **43**, 259–282.

Pinard, J.-P., 2007: Wind climate of the Whitehorse Area. *Arctic*, **60**, 227–237.

— 2008: Mesoscale wind modelling in steep mountain terrain. *Atmosphere-Ocean*, to be published.

Pinty, J.-P., R. Benoit, E. Richard, and R. Laprise, 1995: Simple tests of a semi-implicit semi-lagrangian model on 2D mountain wave problems. *Mon. Wea. Rev.*, **123**, 3042–3058.

Robert, A. J.: 1969, The integration of a spectral model of the atmosphere by the implicit method. *Proc. WMO/IUGG Symp. On Numerical Weather Prediction, Tokyo, Japan Meteorological Agency*.

Tanguay, M., A. Robert, and R. Laprise, 1990: A semi-implicit semi-lagrangian fully compressible regional forecast model. *Mon. Wea. Rev.*, **118**, 1970–1980.

Yu, W., R. Benoit, C. Girard, A. Glazer, D. Lemarquis, J. R. Salmon, and J.-P. Pinard, 2006: Wind energy simulation toolkit (WEST): A wind mapping system for use by the wind-energy industry. *Wind Engineering*, **30**, 15–33.

Chapter 5

A WEST Wind Climate Simulation of the Mountainous Yukon

[1]

[1] A version of this chapter has been published. Pinard Et Al. 2005. Atmosphere-Ocean. **43**: 259-282.

5.1. Introduction

Wind farms are the fastest growing energy sector in the world today. With this new development has come the need for greater accuracy in mapping the wind climate near the ground in order to allow wind farm developers to identify areas of high wind energy potential.

Wind maps have been produced for Europe (Troen and Petersen 1989), the United States (Elliott and Schwartz 1993), and other parts of the world. In Canada, Walmsley and Morris (1992) made the first attempt at defining the country's wind climate. Their map was an interpolation based on wind data from 144 weather observation sites across the country, four of which were in the valleys of the Yukon. The map provided some clues to windy areas but failed to show realistic winds in the mountainous regions of British Columbia and the Yukon Territory. The next Canadian wind mapping attempt was by Benoit et al. (2001) (Vincent and Fick 2001; NG 2002) who used Canadian Meteorological Centre (CMC) operational forecasts computed with grid spacing of 24 km and averaged over five years (1996-2000). This map was still relatively coarse, especially from an orographic perspective, and indicated that the Yukon wind regime was still not adequate for cost-effective power production even though independent observations showed otherwise. Subsequent model runs, however, by Benoit et al. (2001) at a grid spacing of 5 km compared better with field measurements for the Gaspé region than those from the 24-km forecasts, presumably due to better resolution of terrain.

New modelling techniques have recently been employed with some degree of

success in simulating the wind climate using a combined mesoscale-microscale model. Frank et al. (1999) experimented with the Karlsruhe Atmospheric Mesoscale Model (Adrian and Fiedler 1991) and the microscale Wind Atlas Analysis and Application Program (WAsP) (Mortensen et al. 1993) in Finland. Brower et al. (2004) used the Fifth-Generation NCAR/Penn State Mesoscale Model (MM5) and a mass consistent model for the microscale in a number of different climatic regions.

The Wind Energy Simulating Toolkit (WEST) uses the Mesoscale Compressible Community (MC2) model (Benoit et al. 1997) and the linearized microscale model MS-Micro/3 (Mason and Sykes (1979b) version of the Jackson and Hunt (1975) model version for microcomputers/3-dimensional; MS-Micro hereafter) (Walmsley et al. 1990) to produce wind maps of large regions. The WEST has been successfully used to simulate the wind energy potential for several regions across Canada and other parts of the world and it is also being applied to compute a unified wind atlas (see www.windatlas.ca) for the entire country. Whereas most of Canada has relatively low relief terrain, the British Columbia-Yukon region is very mountainous and presents a challenge to models whose grid spacing is relatively coarse compared to the spatial variation of the mountainous terrain of the Yukon. In this region many mountain ridges are too narrow to be completely resolved in a 5-km model grid. WEST, with the inclusion of MS-Micro, provides modelling capabilities to grid sizes of a few hundred metres.

In this paper we use WEST to simulate the wind climate of the southern Yukon and compare its output to field measurements. We describe the orography and wind climate of the territory in Section 5.2. The field measurements, their surrounding

land use, and the variability and vertical projection errors are discussed in Section 5.3. The toolkit structure is described in Section 5.4. The simulation domain with the climate and surface inputs are described in Section 5.5. Although the purpose of WEST is to make use of MS-Micro to refine the MC2 output of wind values near complex surfaces, the outputs of both models are examined and compared in Section 5.6 and a discussion follows in Section 5.7.

5.2. Orography and wind climate of the southern Yukon

A map of the Yukon is given in Figure 5.1 and shows the major mountainous features in and around the territory. Most of the communities in the territory are below 1000 m (heights are given above sea level (ASL) unless otherwise stated). The thicker 2000-m contour lines indicate some of the higher mountainous regions in the territory. It can be observed that the Wrangell-St. Elias Mountains are rather extensive and dominate the south-west Yukon with several peaks above 3000 m. This range also contains Canada's highest peak, Mount Logan, with a height of 5959 m.

To the north-east of the St. Elias Mountains is the Yukon Plateau, which makes up the southern two-thirds of the territory. The name "plateau" is a misnomer, since this area, which ranges from about 300 m to about 2000 m, is not particularly flat. The plateau is bordered to the north-east by the Mackenzie Mountains and to the north by the Ogilvie Mountains. The valleys and ridges are generally oriented in a south-east to north-west direction. This region is home to more than 95% of the territory's population, and includes Whitehorse, Watson Lake, Dawson City, Haines Junction and a number of smaller communities.

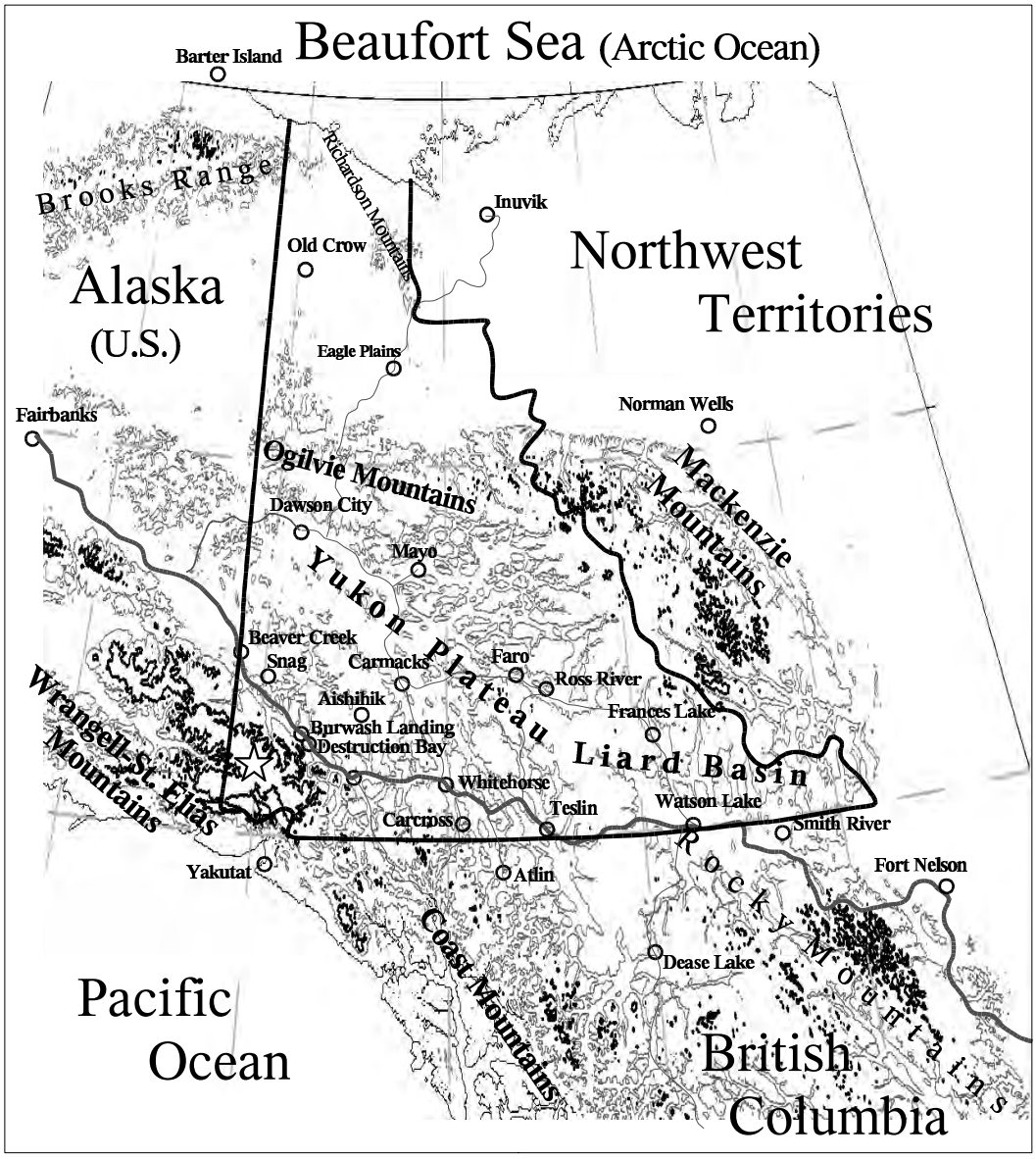

Figure 5.1: This map shows orographic features in and around Yukon. The thin contour line is at 1000 m ASL and the thicker contour is at 2000 m ASL. The Wrangell-St. Elias Mountains are shown to be the largest and highest mountain range in the Yukon Territory. Its highest peak is Mt. Logan at 5959 m ASL (star symbol in south-west Yukon).

The territory's wind climate is highly influenced by its mountainous terrain. Whitehorse, for example, is located in a north-north-west to south-south-east oriented valley about 200 km north of the Pacific Coast. Analysis of upper air and surface wind data shows that the prevailing wind in the Whitehorse valley is mostly from the south-south-east, restricted by the valley orientation. Above the nearby mountaintops, the prevailing wind direction is less constrained and tends to be from the south-west to west. Similar low level conditions are found in the Kluane Lake region (Shakwak Trench; see Fig. 5.2) and Faro (Tintina Trench) where prevailing winds are from the south-east and follow the valleys. Mountaintop winds are stronger in the winter than in the summer, whereas in the valleys the opposite is generally true; the summer valley winds are stronger than those in winter. The upper winds in winter seem to have less influence on the colder, slower-moving air masses in the valleys. Data from the Whitehorse radiosonde station show that a much stronger vertical wind shear exists during the winter than during the summer. This seasonal variation in the vertical wind shear presents difficulties in correlating mean annual winds between wind stations at different elevations.

5.3. Wind monitoring sites in the territory

The locations of the wind monitoring stations used in this study are shown in Fig. 5.2. The stations are listed in Table 5.1 and are classified as an "airport" station or a "wind energy" station. There are seven airport stations, indicated with an "A" in the figure, that were established for airport weather monitoring. The compiled wind data for the airport stations originate from the Atmospheric Environment Service

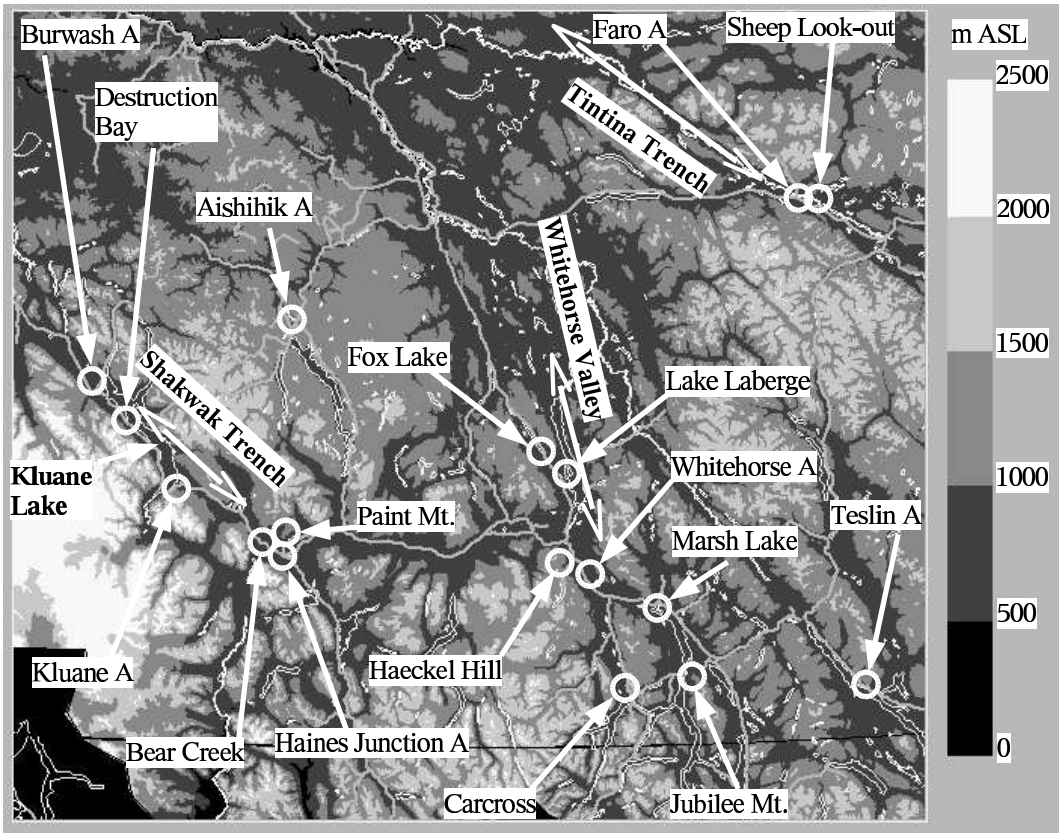

Figure 5.2: Map of the southern Yukon showing the airport and the wind energy stations overlaid on the microscale map used for the MS-Micro simulations. The values in the legend are elevations in metres ASL. The white lines are major rivers and lakes and the thicker grey lines are highways and secondary roads. Note that most of the stations are in the valleys; the three exceptions are Paint Mountain, Jubilee Mountain and Haeckel Hill.

(AES now MSC) (AES 1982) and span five years or more (columns 4 and 5, Table 5.1). The wind sensors were mounted at approximately 10 m above ground level (AGL) (column 3, Table 5.1) and most of the stations were located near airports. Aishihik, Teslin, Haines Junction, and Whitehorse were 24-hour observation sites, whereas Faro and Burwash were daytime hourly. The frequency of wind observations at Kluane was not known. The method of recording wind information has been by human observation of a dial for both the wind speed and direction, subjec-

tively averaged over two minutes. More detailed information can be found in WSD (1977) and (AES 1976).

The Teslin, Faro, and Burwash stations were located in open fields within a few hundred metres of their respective terminal buildings. The Haines Junction station was in an open pasture in a low-lying depression surrounded by small forested hills. It is possible that buildings and nearby trees may have had diminishing effects on the wind speed at these wind stations. The Kluane and the Aishihik stations were dismantled and their exact locations and the surrounding surface roughness conditions are uncertain. The Whitehorse weather station is the most exposed of the airport group. It is located in a short-grass field on a high bank above the city of Whitehorse and clearly open to both the occasional north-northwest wind and the dominant south-south-east wind. The station is about 500 m east of the airport buildings. Observed and best estimates of surface roughness for all these stations are listed in column 7 of Table 5.1 and also in Table 5.3, which is discussed in Section 5.5c.

The "wind energy" group consisted of ten wind stations with sensors at heights ranging from 10 to 30 m AGL (column 3, Table 5.1). For each station, the wind fields were sampled every one or two seconds and the mean statistics were recorded every 10 minutes. The following stations ran for one year: Fox Lake (Cottrell-Tribes 2002a), Carcross (Cottrell-Tribes 2002c), Lake Laberge (Cottrell-Tribes 2002b), Marsh Lake (Cottrell-Tribes 2001), and Jubilee Mountain (Baker 1995). Sheep Look-out (Cottrell-Tribes 2003), Haeckel Hill (Cottrell-Tribes 2000b), Bear Creek (Pinard 2001) and Paint Mountain (Baker 1995) operated for two years. Destruction

Table 5.1: **List of the wind stations used for the model comparison. The heights of the station surfaces and the sensor towers are shown in columns (2) and (3). The period of monitoring and duration are in columns (4) and (5) and the mean wind speeds for the period are in column (6). The surface roughness used to project the wind speeds from their measured heights to 30 m are listed in column (7) and are also referred to in Table 5.3. The projection of the wind speeds from the measured heights to 30 m are listed in columns (8) and (9) and are calculated using Equation (5.1) and the roughness lengths (column 7) for each station. This projection implies possible errors which are shown in columns (10) to (13). There are also errors due to the possible variability of a short monitoring period length to long-term mean in which these stations measured. These errors are shown in columns (14) and (15). Columns (16) and (17) are the total errors that may exist in the measurements. The values in columns (9), (16) and (17) are emboldened; they are compared to the WEST simulation and are also shown graphically in Figure 5.12 along with the model results. Other possible errors used here are sensor and data logger errors which are apparently small enough to be insignificant in this analysis.**

Column (1)	(2)	(3)	(4)	(5)	(6)	(7)	(8)	(9)	(10)	(11)	(12)	(13)	(14)	(15)	(16)	(17)
	Heights		Monitoring				Projection		Projection Error to 30 m				Period Error		Total errors	
	ASL	Tower AGL	Period	Duration	Mean wind speed	surface Roughness length	Ratio to 30 m	Speed at 30 m	Ratio	Below mean	Ratio	Above mean	Error	30-m Speed	Below mean	Above mean
	(m)	(m)	(year)	(years)	(m s^{-1})	(m)		(m s^{-1})	Min	(m s^{-1})	Max	(m s^{-1})	(%)	(m s^{-1})	(m s^{-1})	(m s^{-1})
Airport Aishihik A	966	10	1944-66	12	2.8	0.05	1.21	**3.3**	1.14	-0.2	1.35	0.4	0.06	± 0.2	**-0.4**	**0.6**
Burwash A	799	10	1966-80	14	3.4	0.10	1.24	**4.2**	1.14	-0.3	1.35	0.4	0.06	± 0.3	**-0.6**	**0.6**
Faro A	694	10	1972-77	5	2.1	0.10	1.24	**2.7**	1.14	-0.2	1.35	0.2	0.06	± 0.2	**-0.4**	**0.4**
Haines Junction A	599	10	1963-80	15	1.8	0.20	1.28	**2.3**	1.14	-0.3	1.35	0.1	0.06	± 0.1	**-0.4**	**0.3**
Kluane Lake A	786	10	1974-80	5	2.5	0.05	1.21	**3.0**	1.14	-0.2	1.35	0.4	0.06	± 0.2	**-0.3**	**0.5**
Teslin A	705	10	1955-80	20	2.2	0.20	1.28	**2.8**	1.14	-0.3	1.35	0.2	0.06	± 0.2	**- 0.5**	**0.3**
Whitehorse A	703	10	1955-80	26	3.6	0.02	1.18	**4.2**	1.14	-0.1	1.35	0.6	0.06	± 0.3	**-0.4**	**0.9**
Wind Energy																
Sheep Look-out, Faro	795	30	2000-02	2	4.6	1.00	1.00	**4.6**	1.00	0.0	1.00	0.0	0.12	± 0.6	**-0.6**	**0.6**
Haeckel Hill	1440	30	1998-01	2	7.1	0.01	1.00	**7.1**	1.00	0.0	1.00	0.0	0.06	± 0.4	**-0.4**	**0.4**
Destruction Bay	823	30	1995-98	3	6.0	0.05	1.00	**6.0**	1.00	0.0	1.00	0.0	0.06	± 0.4	**-0.4**	**0.4**
Bear Creek	670	26	1998-00	2	4.9	0.01	1.02	**5.0**	1.00	-0.1	1.06	0.2	0.06	± 0.3	**-0.4**	**0.5**
Fox Lake	793	20	2001-02	1	2.2	3.85	1.25	**2.7**	1.05	-0.4	1.31	0.1	0.14	± 0.4	**-0.8**	**0.5**
Carcross	702	20	2001-02	1	3.3	3.55	1.23	**4.1**	1.05	-0.6	1.30	0.2	0.14	± 0.6	**-1.2**	**0.8**
Lake Laberge	645	10	2001-02	1	3.8	0.01	1.16	**4.5**	1.14	-0.1	1.35	0.7	0.14	± 0.6	**-0.7**	**1.4**
Marsh Lake	656	10	2000-01	1	2.6	0.01	1.16	**3.0**	1.14	-0.1	1.35	0.5	0.14	± 0.4	**-0.5**	**0.9**
Paint Mountain	1370	10	1992-94	2	4.4	0.05	1.21	**5.3**	1.14	-0.3	1.35	0.6	0.12	± 0.6	**-0.9**	**1.3**
Jubilee Mountain	1280	10	1993-94	1	3.5	0.05	1.21	**4.3**	1.14	-0.2	1.35	0.5	0.14	± 0.6	**-0.8**	**1.1**

Bay (Cottrell-Tribes 2000a) operated for three years.

The sites for wind energy stations were normally chosen in order to have maximum exposure to the prevailing winds. The stations at Haeckel Hill (30 m AGL), Paint Mountain (10 m AGL), and Jubilee Mountain (10 m AGL) were located on mountaintops with surfaces of bare rock and low shrubs. Sheep Look-out (30 m AGL) was in an approximately 8-m tall poplar forest on a small hill in the valley of the Tintina Trench open to the south-east winds. The Lake Laberge (10 m AGL) site was on a small smooth-rocked hill by the lake shore which was exposed to dominant south-east winds. Destruction Bay (30 m AGL) was located on a grassy bank along the Kluane Lake shoreline and open to the prevailing south-east winds. Bear Creek (26 m AGL) was also on a short-grassed bank and open to frequent winds of the Alsek Valley to the south-east. The Carcross station (20 m AGL) was in a 6-m tall poplar forest on a hill exposed to winds from Bennett Lake to the south-west. The Marsh Lake station (10 m AGL) was on a sandy beach and open to the lake to the south and south-east. Fox Lake (20 m AGL) station was located in an area of heavily wooded spruce trees approximately 15 m high in a north-northwest to south-southeast valley. More details on their surface roughnesses can be found in Table 5.3.

In order to project the short monitoring periods of a wind energy station to long-term means, correlations of monthly mean wind speeds have been computed between three of the stations and nearby airport stations. Destruction Bay was shown (Cottrell-Tribes 2000a) to have a correlation of R = 0.91 with the Burwash airport station, its mean speed was projected to a 30-year long-term mean and is noted

in column 6 of Table 5.1. The Bear Creek station had a correlation of about 0.85 with the nearby Haines Junction station, its mean wind was projected to 12 years. Haeckel Hill had a correlation coefficient of 0.93 to the nearby upper air data interpolated at 1400 m and was projected to nine years. Errors due to the variability from the long-term mean at these stations are addressed in the next paragraph.

The other stations correlated poorly with their nearest long-term neighbour, and as a result, the possible error due to the variability in the shorter monitoring periods is examined by analysing long-term data available for the Whitehorse and Haines Junction airport stations. These two stations had very similar results. The Whitehorse station, which has the longer period of record, is shown in Figure 5.3. The data used here are monthly mean wind speeds from a 10-m tower for the period 1990 to 2004. Figure 5.3 shows the minimum, maximum, and the standard deviations of the mean wind speed for five different running average periods over the long-term monthly mean of the dataset. The values in the figure show that the mean wind speed for a wind monitoring period of less than one year will likely vary more than $\pm 14\%$ from the long-term mean. For a two-year monitoring period we would expect the mean to vary less than $\pm 12\%$ from the long-term mean. The variability diminishes further for the three- and five-year means to $\pm 9\%$ and $\pm 6\%$ respectively. This analysis suggests that the mean wind speeds for all of the airport stations should not vary by more than 6% from the long-term mean since their record lengths are five years and longer. The variations for these stations are shown in columns 14 and 15 of Table 5.1. Using the above argument, we assume that those wind energy stations that correlated with the long-term stations probably

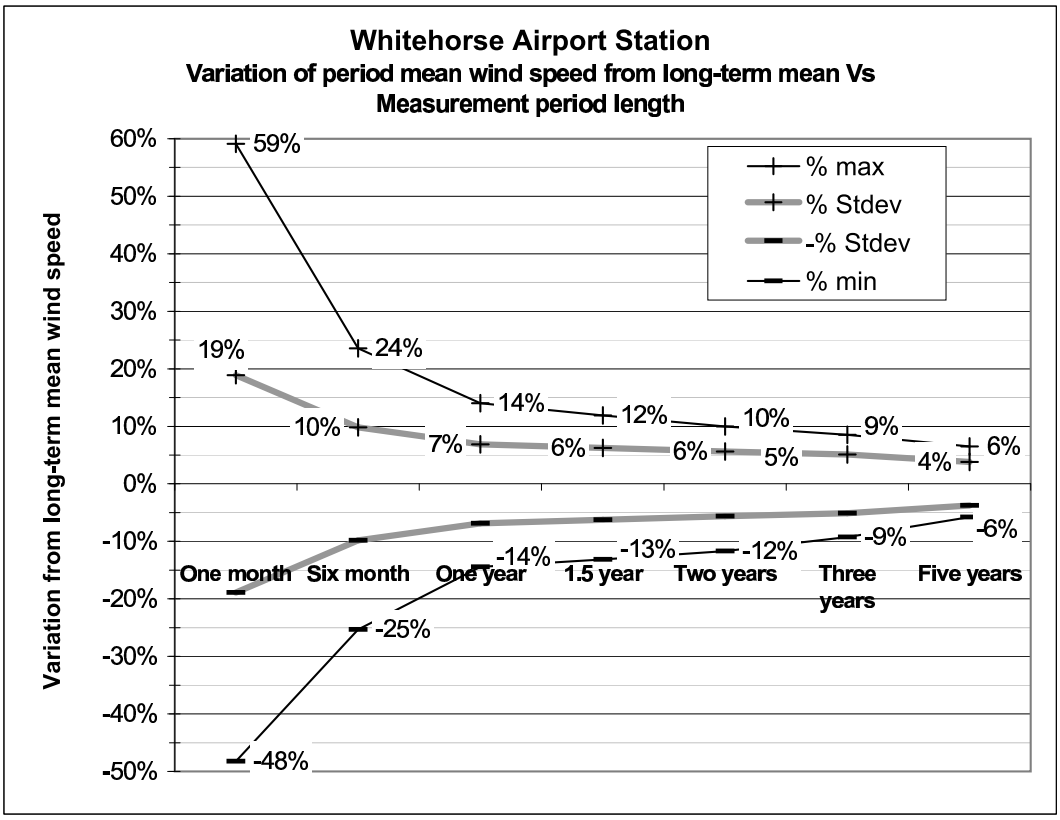

Figure 5.3: This graph compares the variability of different period lengths of a running average to the long-term mean for the Whitehorse airport station. The analysis is from monthly mean wind speeds (at 10 m ASL) for the years 1990 to 2004. The standard deviations, minima, and maxima of running means for different period lengths are displayed. The minimum and maximum percentage values are used in the analysis, the standard deviations are for comparative purposes only.

had maximum variability errors of about 6%. One could argue that the error might be closer to 12% because these stations collected data for two years or more and that the correlation might not be representative. Consequently, this translates to a wind speed error, say for a 6-m s^{-1} wind speed, of 0.7 m s^{-1} at 12% and 0.4 m s^{-1} at 6% error.

All comparisons in this study were made at a height of 30 m AGL, a typical hub height for community scale wind turbines. (MS-Micro is capable of producing

results at any specified height, but only 30 m was chosen for this study.) The measured wind speeds below 30 m AGL and the MC2 wind speed at 65 m AGL were projected vertically to 30 m AGL using a simple logarithmic profile that makes use of the surface roughness z_0 for each site, namely

$$\bar{u}(z_p) = \bar{u}(z_m)\frac{\ln(z_p/z_o)}{\ln(z_m/z_o)} \tag{5.1}$$

where the wind speed $\bar{u}(z_m)$ measured (or modelled) at height z_m is projected vertically to a new speed $\bar{u}(z_p)$ and height z_p.

This logarithmic projection was performed instead of obtaining the wind speeds directly from the model for the exact heights at which the measurements were taken. At the time the modelling was done, results could not be obtained for 10 m or 20 m. For MC2, because of model instability at finer vertical resolution and limited computer resources, it has been problematic to use a near-surface grid spacing finer than 65 m in the vertical.

The vertical projections may seem to impair the purpose of this model-to-measurement comparison. The simple logarithmic projection of wind speed may not be accurate in complex terrain with varying surface heights and roughnesses. This relation also assumes neutral stratification which will reduce the differences between the projected wind speeds between two heights. However, at this relatively early stage of the WEST model development it may not be critical considering that a 65-m high point in the MC2 model represents a 5-km square area. It will become more evident in Section 5.6 that the errors in the vertical projection will not significantly impede the model-to-measurement comparison. The more important analysis and

discussion will be in the bias between the model and the measurements that are likely more related to the model terrain. In a future study MS-Micro will be configured to produce wind speeds at 10-m heights in order to avoid the problem of vertical projections.

Using Equation (5.1) the vertical projection ratios were calculated for each station and are shown in column 8 of Table 5.1 with their corresponding new wind speeds at 30 m AGL in column 9. Taking into account that projecting wind speeds vertically also results in errors, a calculation of possible minimum and maximum projection ratios was made. The smallest wind speed increase from, say 10 m to a height of 30 m could be computed from Equation (5.1) using the smoothest surface that could exist at a site, that is, a value of z_o = 0.003 m, for the surface roughness of a flat short-grass field. At the 30-m height this results in a speed increase of 1.14 times the 10-m speed value and is correspondingly smaller for the 20-m heights. The Bear Creek station at 26 m was chosen to have no increase as a low estimate. These values are listed in column 10 and the wind speed differences between the calculated mean and the minimum (negative signs) are shown in column 11 of Table 5.1. The maximum possible increase for the 10- to 30-m heights is inferred from a compilation of mean wind speed profiles from various 30-m stations in the territory and particularly from analysis of the Whitehorse upper air station. These profiles show that, for the normally stable atmosphere and typical surface roughness in Yukon valleys, the maximum increase in speed from 10 to 30 m is about 1.35 times. The speed projections from the other heights, 20 m and 26 m, are made using a logarithmic interpolation scheme that fits the vertical profiles of the

measurements. These projection values, along with the mean to maximum speed differences at 30 m, are listed in columns 12 and 13 of Table 5.1.

The total wind speed projection errors due to the vertical projections and the variability in the temporal means are listed in columns 16 and 17 of Table 5.1. Other possible sources of error are the sensors and the data recording devices. These errors are assumed to be small and are not considered in the analysis.

5.4. WEST: the wind energy simulation toolkit

This section briefly describes the toolkit and the MC2 and MS-Micro models. WEST combines the mesoscale model MC2 (Benoit et al. 1997) and the microscale model MS-Micro (Walmsley et al. 1990) to produce a wind map of a large complex region of interest. The reason for the two-model combination in WEST is that the formulation of MS-Micro is much simpler (Jackson and Hunt 1975) than that of MC2. The problem with reducing the MC2 grid spacing to, say below 1 km (horizontal), is that it requires greatly increased computer resources to deal with the increased number of grid points. MS-Micro helps to reduce the final grid spacing to several tens of metres without significantly increasing processor time. With MS-Micro, only the target heights (say, a wind turbine hub height of 30 m AGL) need to be computed, resulting in an efficient two-dimensional microscale flow model.

The structure of the toolkit is shown in Figure 5.4. For initialization, WEST includes a dataset of wind climate statistics (described in Section 5.5a) generated through a classification scheme that is available in a meteorological database. The digital elevation model (DEM) and the surface roughness (land use; described in

Section 5.5c) are also taken into account using a surface property generator. These are available in a terrain database for use by both MC2 and MS-Micro. Through the initialization scheme, these databases are used by MC2. The output of MC2 is post-processed with a statistics module and stored in a mesoscale wind database. This database is useful for analysing mesoscale wind fields and has been used for Environment Canada's wind atlas (see www.windatlas.ca). In WEST, the mesoscale wind database is used by the microscale model, MS-Micro, along with the terrain data generated from a higher resolution terrain database with the same algorithm used for MC2. There is a mesoscale-microscale coupling scheme that consists of multiple microscale domains centred on each mesoscale grid point (or every third point in WEST, more details are given in Section 5.5d). The microscale domains overlap each other and a blending scheme is applied to combine each domain into one single large grid covering the entire mesoscale domain. There can be one to ten thousand such microscale domains executed in a single mesoscale domain. The statistics module is applied to the MS-Micro output and the data are stored in a microscale wind database. Both the mesoscale and the microscale data can be sent to a post-analysis graphical package for viewing and analysis.

a. *MC2*

The MC2 model has been developed over several years by the Recherche en Prévision Numérique (RPN) group in Dorval, Québec. MC2 is a limited area model with a terrain-following vertical coordinate system, open boundaries, and self-nesting

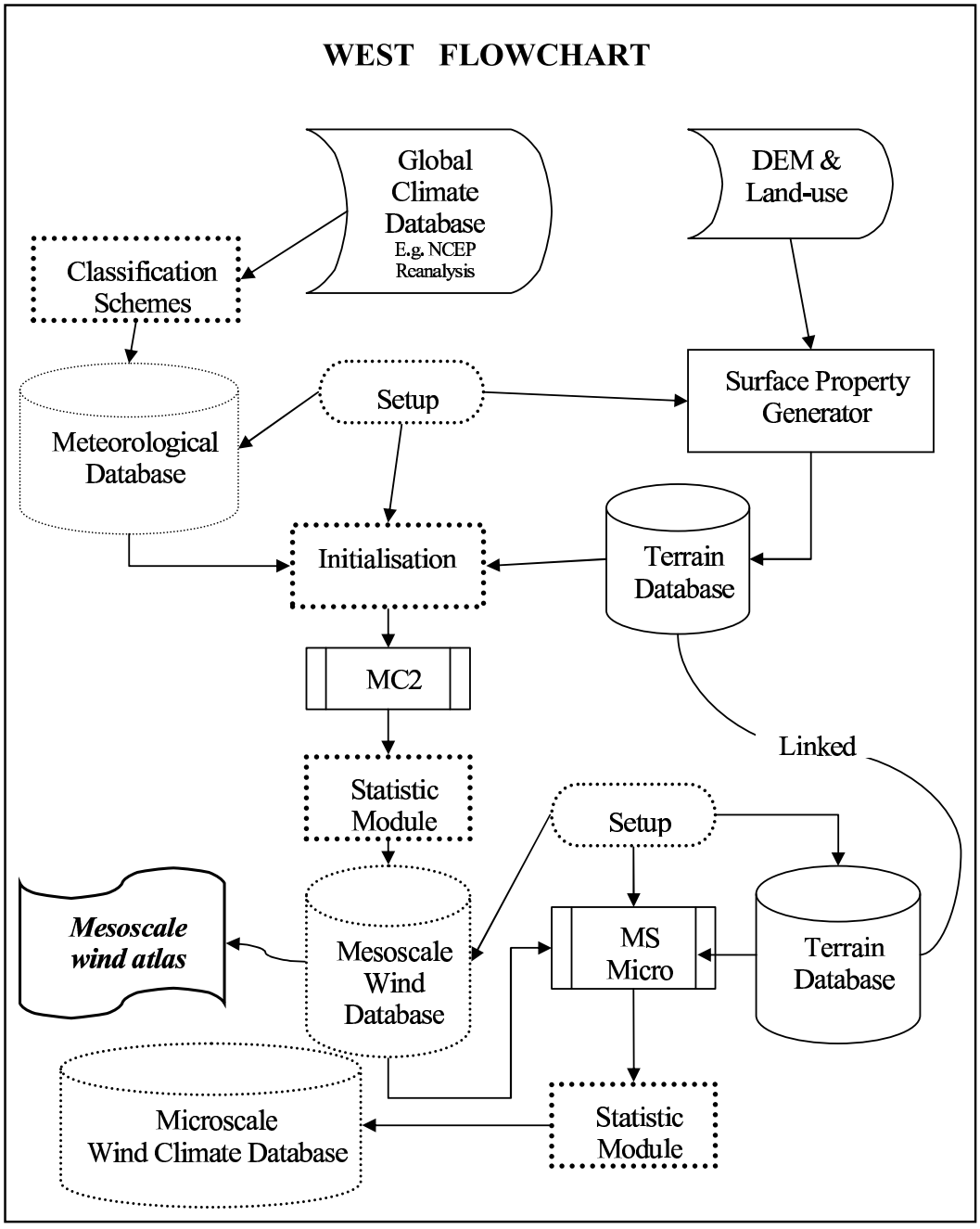

Figure 5.4: The WEST flowchart includes four important modules: a classification scheme for the climate data, the MC2 mesoscale modelling engine, a statistics module, and a microscale modelling engine. The meteorological database is derived from the NCEP/NCAR reanalysis. The DEM and land use data are from the USGS database.

capabilities. It is non-hydrostatic, three-dimensional, time dependent, with fully compressible Navier-Stokes equations. The model has a semi-implicit formulation with a stationary isothermal hydrostatic basic state, and a three-dimensional semi-Langrangian advection. The complete formulation of the model dynamics can be found in Tanguay et al. (1990) and Benoit et al. (1997).

MC2 can be run in two configurations, one being a weather forecast mode where time is critically important and all of the "physics" in the model are used. The second mode, which is used in the present study, is time independent and is more of a boundary-layer type flow where the lower 5 km AGL are most important. Here most of the "physics" are not used (ie. the model neglects surface-air energy fluxes, latent heating, clouds, etc.), the initial state is simplified, that is, the isobars are straight at all levels, and the model is allowed to achieve pseudo-equilibrium. The only physics component invoked is the adiabatic turbulent boundary layer.

The turbulence closure scheme used for this model is described in Mailhot et al. (1998). It is based on a vertical diffusivity formulated as the product of the square root of the turbulent kinetic energy and a length scale that is proportional to height. The product of these two terms is divided by a static stability function dependant on the Richardson number. The vertical diffusion coefficient, consequently, is variable throughout the model layers and should reflect the intensity of the turbulent exchanges near the surface. At the surface, the turbulent fluxes are continuous with surface energy exchanges computed from Monin-Obukhov similarity theory. At the upper boundary, the flux vanishes.

b. *MS-Micro*

Jackson and Hunt (1975) developed a linearized dynamical model for turbulent flow over a shallow two-dimensional hill. Mason and Sykes (1979a) took their two-dimensional formulation and extended it to three dimensions. This development led to the creation of MS-Micro and of WAsP (Troen and Petersen 1989).

MS-Micro (Walmsley et al. 1990, 1982; Taylor and Teunissen 1983; Walmsley et al. 1986) consists of a vertical coordinate system that follows the terrain of a gently sloped hill whose shape and size define scaling parameters and are, in principle, compatible with the linearization of equations of motion.

The model assumes a neutrally stratified atmosphere that consists of an inner and an outer layer. The outer layer is represented by pressure gradients determined by an inviscid and irrotational potential flow. The outer solution provides the perturbation pressure fields that force the elevation-induced flow perturbations within the inner layer.

The momentum budget of the inner layer is a balance between advective, pressure-gradient, and turbulent-viscous forces in the form of linearized perturbation momentum equations. The turbulent transfers are parametrized by a simple mixing length closure scheme. The velocity perturbations of governing equations are solved analytically with the use of Finite Fourier Transforms. These transforms impose limitations on the model circumstances and may reduce the accuracy of the solutions. The most important of these limitations is that neutral stratification is assumed, others are that the slopes must be less than 25%, and the Coriolis force

is neglected. The suggested size of the model is to be no more than 10 km (size of the "island", see Section 5.5d) and that the vertical solution levels are within 1 to 150 m AGL.

5.5. Inputs and settings for the southern Yukon simulation

A model simulating a real life situation is only as good as the data that are available to it. In this section we attempt to ensure that the input data represent the reality that is being simulated. In Section 5.5a we describe the climate data that are used in the mesoscale model MC2. In Section 5.5b we compare the input climate data with the upper air data from Whitehorse and to some extent, Yakutat. In Section 5.5c the land use data and the DEM are also examined and compared to observations at the monitoring sites. Section 5.5d provides a description of the model configuration and some of the methods which were used when the combined simulations in WEST were carried out for the southern Yukon case.

a. *The MC2 input climate data*

Meteorological centres, such as the Canadian Meteorological Centre, the National Centers for Environmental Prediction (NCEP), and the European Centre for Medium-range Weather Forecasts collect and analyse data from surface stations, radiosondes, ships, airplanes, radars, and satellites every six hours. These centres are able to provide long series of quality controlled and analysed three dimensional (3-D) global data grids. Subsets of theses data for the region of interest, serve as the input

to the MC2 model, used in the Yukon wind simulation with WEST.

The wind climate classification follows the methodology set out in Frank and Landberg (1997). Each element of the time series of the geostrophic wind (components u_g in the east direction, v_g in the north direction) at 1000 mbar (near sea level) during the 43 years of NCEP Reanalysis data (Kalnay et al. 1996) is classified into tri-variate bins for

a direction (16 bins),

b speed (3-7 bins, depending on overall frequency of occurrence for that direction), and

c 1000-850 mbar geostrophic shear (2 bins, i.e., positive and negative shear).

The overall number of possible bins is $16 \times 7 \times 2 = 228$. The actual number of non-empty bins is climate dependent for each region and for the southern Yukon there are 162 bins. The wind speeds and directions from these bins were compiled and are presented in the form of wind energy-frequency roses in Figure 5.5 and Figure 5.6. These are discussed in Section 5.5b.

For each climate bin one MC2 run is executed, thus 162 runs are made for the southern Yukon. The whole 3-D mesoscale grid is initialized from the data of each bin component, that is, that bin's set of values for u_g, v_g, and temperature at four levels, 0, 1500, 3000, and 5500 m. This is a level-by-level geostrophic-hydrostatic initialization scheme that initializes the model fields to a horizontally uniform state (as seen along iso-planes of the vertical coordinate). It amounts to spreading the single profile for that bin, or climate condition, to the entire 3-D grid according

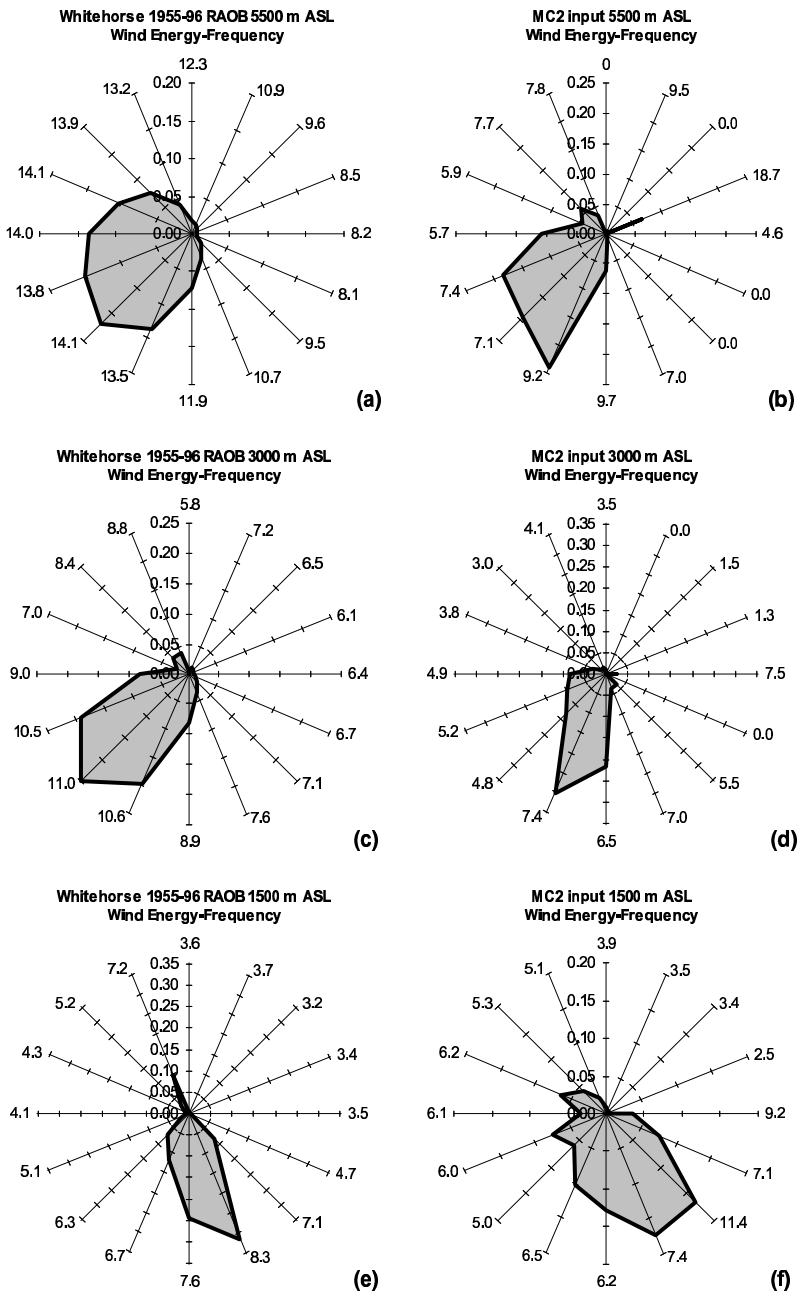

Figure 5.5: Wind energy-frequency roses for the Whitehorse upper air station on the left and the MC2 input data on the right, are shown at three elevations: 5500, 3000, and 1500 m. The wind energy-frequency rose is calculated, for each direction, as the product of the cube of the mean wind speed and its frequency of occurrence divided by the sum of those products in all directions. The long-term mean annual wind speed that occurs in each of the 16 directions is labelled at the end of each arm. The roses show that the wind climate input data for MC2 compares reasonably well with the Whitehorse data in terms of direction but displays rather low wind speeds at the 3000 and 5500 m levels.

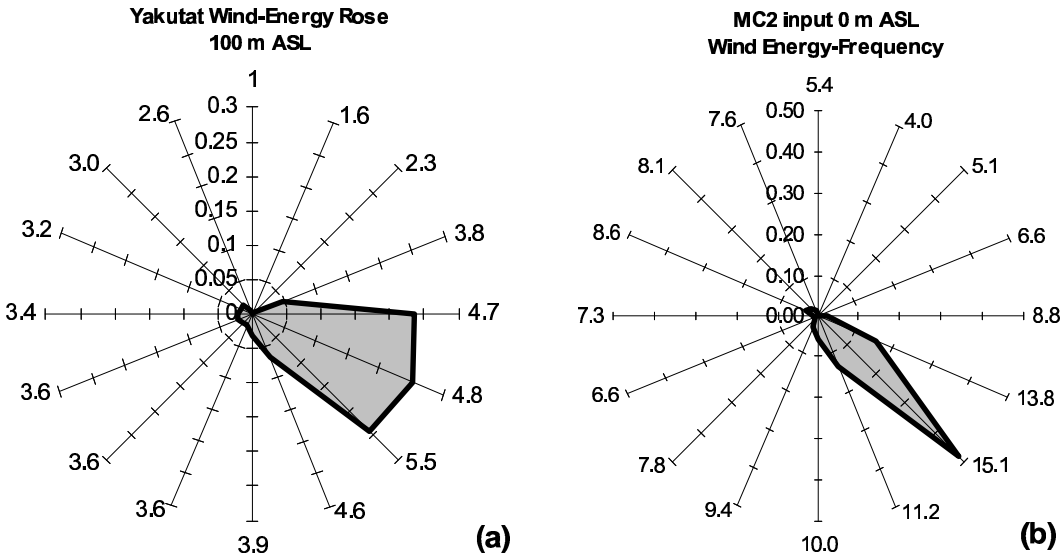

Figure 5.6: Same wind energy-frequency roses as in the previous figure. The rose on the left is for the Yakutat upper air station at 100 m ASL and the one on the right is for the MC2 input at sea level. The MC2 input displays a sharper wind direction for the south-east than the Yakutat rose. The MC2 input wind speeds at sea level are also higher; they are considered as geostrophic, that is, without the effect of surface friction.

to simple dynamical principles. Subsequently, the MC2's Navier-Stokes dynamics will transform that simple initial condition and adapt the quasi-straight flow to the terrain, within a few hours of physical time. All of the 162 runs use surface grids for the orography and land use.

Each simulation is performed as a dynamical downscaling of a quasi-geostrophic and horizontally uniform initial state. This is computationally less costly than the usual prognostic mode. The entire set of realizations is then combined according to the method of statistical-dynamical downscaling (Fuentes and Heimann 1996). This results in a statistically rich set of two-dimensional (2-D) mesoscale numerical data, which consists of moments of the flow vectors from several low levels of the MC2, point wind rose frequency, kinetic energy flux; i.e., the so-called wind-power

potential, joint speed-direction probability density function (PDF), and Weibull parameters of the joint PDF.

b. *MC2 input climate data versus Whitehorse and Yakutat radiosonde data*

To verify that the MC2 input climate data model is representative of the southern Yukon wind climate, it is compared to a forty-year time series of soundings from the Whitehorse upper air station at 1500, 3000, and 5500 m elevations and for the Yakutat upper air station at 100 m ASL. The Whitehorse station is well centralized in the model domain and should be representative of the regional wind climate. Yakutat is located in Alaska along the Pacific Coast and is 70 km to the south-west of Kluane National Park and 280 km west-southwest of Whitehorse. The soundings from the Whitehorse upper air station were compiled and arranged into the wind energy-frequency roses (explained in the next paragraph) shown in Figs 5.5a, 5.5c, and 5.5e. These roses are compared to those of the input data for MC2 which are in Figs 5.5b, 5.5d, and 5.5f. The Yakutat rose was compiled at 100 m ASL and is compared to the MC2 rose at level as shown in Fig. 5.6.

The orientation of the wind roses is such that north is towards the top of the page, east is the right arm, and so on. There are 16 sectors and each sector is 22.5 $^{\circ}$ wide centred on the arm. The value at the end of each arm represents the long-term annual mean wind speed (m s^{-1}) in each direction sector. The perimeter of the area in the wind rose represents the wind energy-frequency in each direction. The wind energy-frequency is the percent frequency of wind occurrence multiplied by

the cube of the mean wind speed and divided by the sum of those products in all directions.

The two wind datasets generally agree and show that there is a common trend of west to south-west winds at the levels above the mountaintops (at 3000 and 5500 m), and more south-easterly winds within the valleys (1500 m). At the 5500-m level, the MC2 input rose (Fig. 5.5b) displays a relatively stronger south-southwest component than the more widely south to west wind energy distribution of the Whitehorse rose (Fig. 5.5a). At this same level, the wind speeds (14 m s^{-1} from the south-west) for the Whitehorse radiosonde are about double those of the MC2 input ($\sim$ 7 m s^{-1} in the same general directions). At the 3000-m level, the Whitehorse rose (Fig. 5.5c) displays a narrower band of prevailing winds from the south-west than the level above, whereas the MC2 rose (Fig. 5.5d) displays a somewhat narrower south-south-west trend. The directional mean wind speeds of the MC2 input at 3000 m are weaker, being less than 70% of those for the radiosonde data.

The wind energy-frequency rose for the Whitehorse radiosonde station, shown at 1500 m in Fig. 5.5e, is typical of winds following the Whitehorse valley, which is in a north-northwest to south-southeast orientation. In the MC2 input data, the 1500-m level input, displayed in Fig. 5.5f, shows that the wind directions are more broadly spread with winds from the south to south-west. This broader distribution should be expected since it is not yet confined within any particular valley orientation when being applied to the model. The MC2 wind speeds are similar to those of the radiosonde at the same level except for the south-east arm where the wind speed is about 60% higher in the MC2 input.

The MC2 wind energy-frequency rose (Fig. 5.6b) at sea level reveals a strong south-east wind energy trend whereas Yakutat (Fig. 5.6a) is spread form the east to south-east. The model input winds at sea level seem rather high. The MC2 values are 10-15 m s^{-1} compared to the Yakutat values of 4-6 m s^{-1}. One argument for the high wind speed at sea level is that it does not include surface effects (that is, it is geostrophic) and it should diminish when the model terrain is used.

Figure 5.7 shows more clearly the differences between the vertical profiles of the long-term mean wind speeds for the MC2 input and those of the Whitehorse and Yakutat radiosondes (15-year mean). The panel on the left shows that the average wind profile of the 162 climate bins of the MC2 input have a somewhat inverse relationship to the Whitehorse and Yakutat radiosonde profiles. The wind speeds for MC2[2] at 3000 to 5500 m are of the order of 5 m s^{-1} less than both the Whitehorse and Yakutat winds, which are 9 to 13 m s^{-1}. At the 1500-m level they are relatively close, between 6 to 8 m s^{-1}. The sea level mean input speed for MC2 is about 10 m s^{-1}, the highest mean wind speed in the MC2 profile. The Yakutat soundings show wind speeds of about 6 m s^{-1} at 300 m which then decline sharply to zero at the surface. In the panel on the right, the profiles for the seven dominant wind climate bins, which represent 65% of the total wind energy in the model, are shown along with the July and the January long-term mean wind speed from the Whitehorse radiosonde data. This panel is used for comparison with the panel on

[2]Note that the MC2 input winds are considered geostrophic throughout the vertical and are used to set the pressure gradient in the model. These same input winds are then used to initialize the wind speed in the model. The measured winds are typically geostrophic above the orographic roughness but are not geostrophic within the valleys.

the left. The seven dominant bins occur in the winter but do not match the January profile for Whitehorse (they should be similar).

In Figure 5.8 the potential temperature profiles of the seven dominant wind climate bins are shown along with the mean for all the climate bins. The figure also includes the 15-year January, July, and yearly means of potential temperatures from the Whitehorse radiosonde. The potential temperatures are converted from measured temperatures using a lapse rate of -1 K per 100 m rise in altitude starting at sea level. The yearly mean potential temperature profiles for the MC2 input and the radiosonde are very similar. They both show a quasi-linear rise in potential temperature from 283 K at 1000 m ASL to about 300 K at 5000 m. The seven dominant climate bin temperature profiles of the MC2 input are clustered around the values for the Whitehorse mean January radiosonde profile. This confirms that the seven dominant wind climate conditions should occur in the wintertime. Further analysis (not shown) indicates that the July profile for the radiosonde is at the upper temperature limit of the 162 wind climate bins.

A neutrally buoyant condition in Figure 5.8 is a vertical line (i.e., potential temperature is height independent). As mentioned earlier, the temperature profiles at high latitudes reveal strongly stable atmospheric conditions throughout the year. This is evident here, where the mean potential temperature lapse rate of the MC2 input and the Whitehorse radiosonde average about +0.42 K/100 m. Strong stability suggests that the atmosphere is highly stratified, a condition in which the vertical mixing of the air from the mountaintop winds into the colder, denser valley air is less likely, especially in the winter.

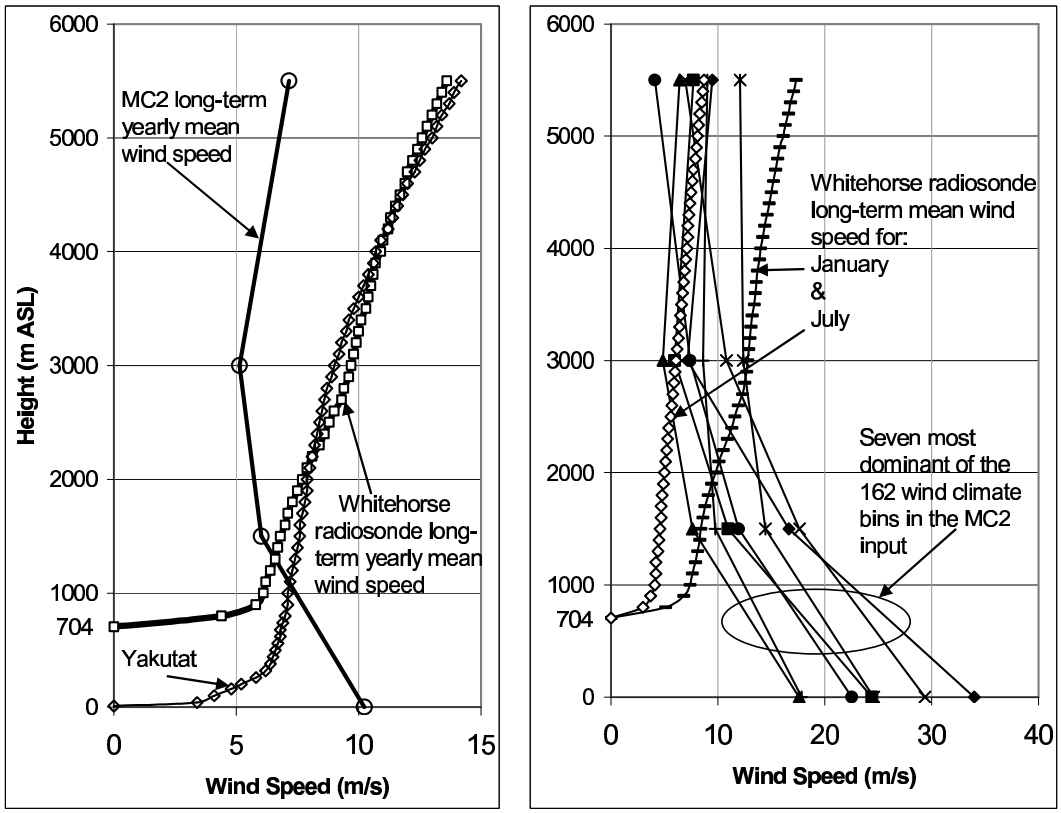

Figure 5.7: The chart on the left shows an inverse relationship in the vertical profiles of long-term yearly mean horizontal wind speed between the MC2 input and the radiosonde data of Whitehorse (704 m ASL) and Yakutat (10 m ASL). We must keep in mind that the MC2 input wind speed is geostrophic whereas those of the radiosonde data are measured and actual. The chart on the right compares Whitehorse radiosonde profiles for January and July (15-year mean) with the seven dominant wind climate bins which represent 65% of the energy in the wind climate input data. The seven dominant wind bins are wind climates that occur in the wintertime. The comparison on the left shows that the MC2 input data tend to underestimate wind speeds at levels of 1500 m and up and overestimate them at sea level.

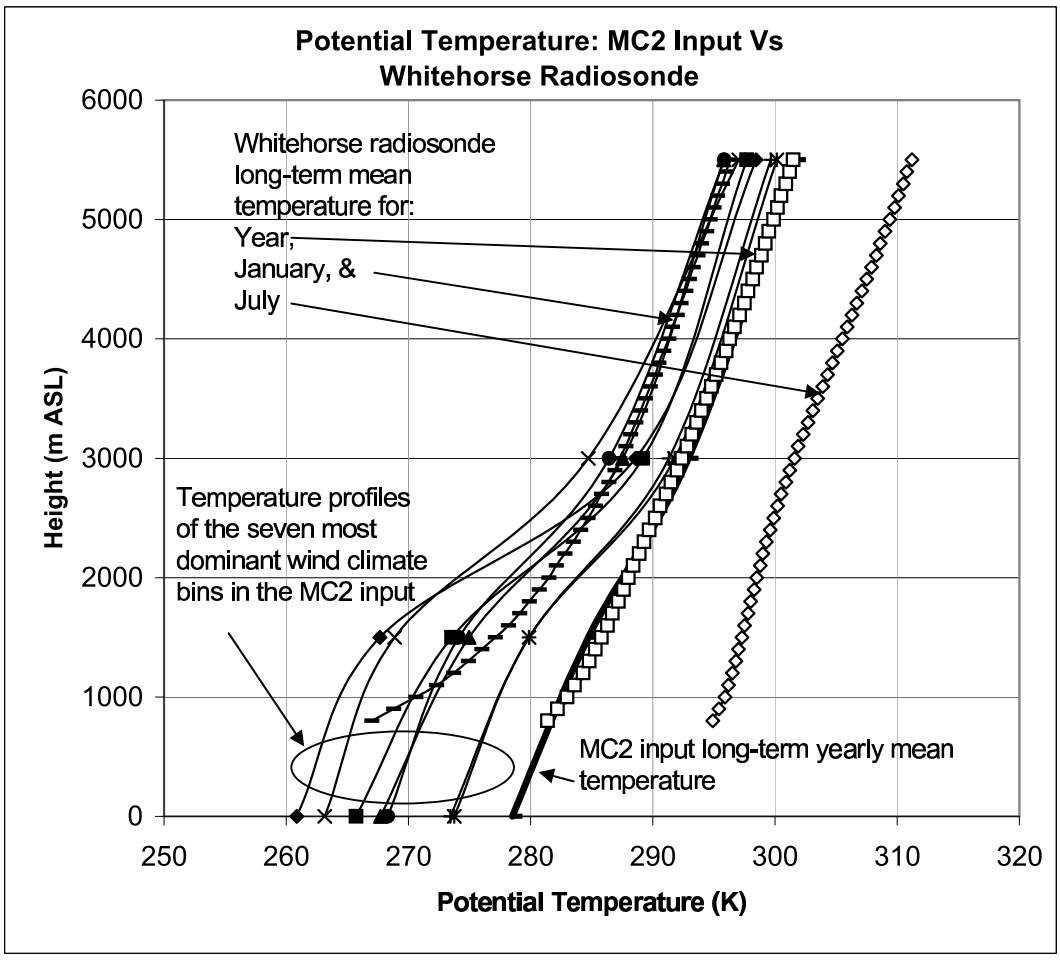

Figure 5.8: Vertical profile of input potential temperature for the WEST simulation along with the Whitehorse radiosonde profile for (15-year mean) January, July, and year. The single thick line is the weighted mean potential temperature of all 162 climate categories. There is also a series of the seven most important wind climate bins which represent 65% of the wind energy of the whole bin set. The yearly mean temperature for both the Whitehorse radiosonde data and the MC2 input data are very similar in value. The series of seven are clustered around the Whitehorse January mean as expected as these seven bins occur in the winter.

c. *The surface data*

Land use, or surface roughness, data are used by both the MC2 and the MS-Micro models to estimate winds near the ground. The roughness data used as input to WEST are based on vegetation classes identified by the United States Geological Survey (USGS) satellite classification. There are 26 roughness classes available for the WEST input and they are shown in Table 5.2. The land use map of the southern Yukon is accurate to 1 km and is represented in Figure 5.9. This map shows that the territory is mostly covered by tundra, particularly at higher elevations. The valleys are dominated by boreal spruce (evergreen needleleaf) and poplar (deciduous broadleaf) forests. Other areas in between are covered by deciduous shrubs and lakes. In the south-west are the Kluane ice fields, an area dominated by ice as shown by the land use map. This ice may misrepresent the surface as being overly smooth, like a lake ice surface. The ice fields are generally covered by snow and may be rougher than a lake ice surface.

The land use values that coincide with the wind sites are shown in Table 5.3 and are compared with the observed land use and estimated values of surface roughness at each site. Overall, the surface is somewhat rougher than the land use data suggest. It should be noted here that the satellite data, which were likely acquired during the last decade, may not necessarily reflect the conditions at the airport sites that were monitored a few decades ago. The same is true for the field observations made more recently. The past surface conditions are not well known. There may have been buildings nearby, or the towers may have been moved. These possibili-

Table 5.2: The following are roughness classes used for interpreting the land use data in the satellite imagery. The map resulting from the assigned surface roughness, shown in Fig. 5.9, is used in MC2 and MS-Micro.

Roughness Class	z_o (m)	Surface description
1	0.001	water
2	0.001	ice
3	0.001	inland lake
4	1.5	evergreen needleleaf tree
5	3.5	evergreen broadleaf tree
6	1	deciduous needleleaf tree
7	2	deciduous broadleaf tree
8	3	tropical broadleaf tree
9	0.8	drought deciduous tree
10	0.05	evergreen broadleaf shrub
11	0.15	deciduous shrub
12	0.15	thorn shrub
13	0.02	short grass and forbs
14	0.08	long grass
15	0.08	arable
16	0.08	rice
17	0.35	sugar
18	0.25	maize
19	0.1	cotton
20	0.08	irrigated crop
21	1.35	urban
22	0.01	tundra
23	0.05	swamp
24	0.05	soil
25	1.5	mixed wood forest
26	0.05	transitional forest

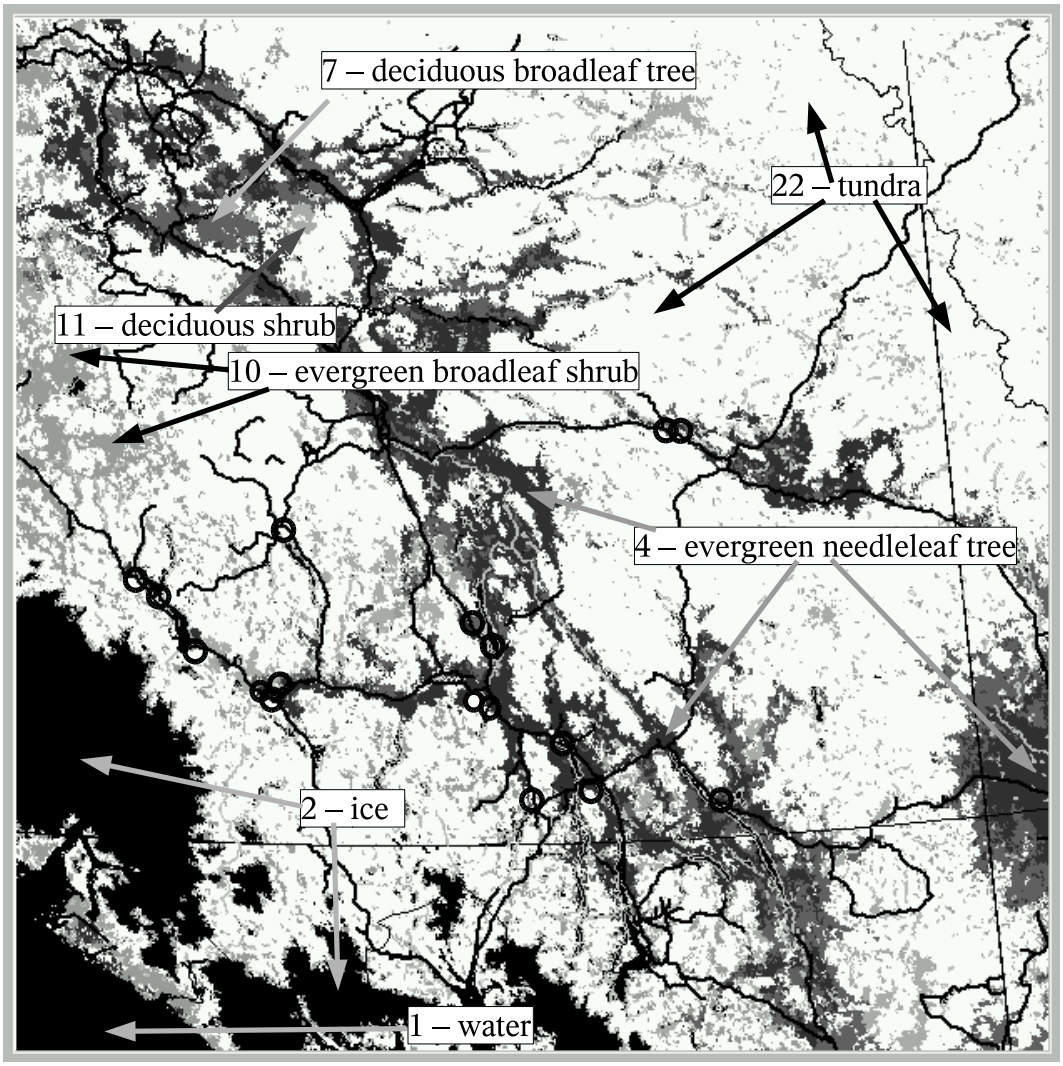

Figure 5.9: Land use map of the southern Yukon can be referenced to Table 5.1 for the surface roughness values. This map shows that most of the southern Yukon is covered with tundra. The treed areas are typically located in the valleys. The areas indicated as ice are the Kluane ice fields, which are treated as having the same surface roughness as water.

ties cannot be excluded, although definite information has not come to light either from the literature or from conversations with knowledgeable locals. If the surface conditions were smoother (as pointed out in Section 5.3) then, this would imply that the wind speeds projected to 30 m would be less, thus widening the gap between the model output and the measured values, as will be seen later.

The satellite land use data at 1-km resolution were applied to the 5-km grid of MC2. Those coincident grid-point values then represent larger areas, overriding the accuracy of the original data. Some land features may not be resolved faithfully on a 5-km square area. For example, the Teslin airport site was, according to the land use data, situated on water (z_o = 0.001 m) when in reality it was situated on land (z_o = 0.2 m).

The DEM data used in the MS-Micro simulations originate from 1:250,000 National Topographic Systems (NTS) from Canadian digital elevation data (NRCan 2000) at Geomatics, Canada. The original DEM, spaced 93 m (north-south) by 35 to 65 m (east-west) is projected to a 333-m spaced microscale grid (see Fig. 5.2). The terrain grid used by MC2 is derived from the USGS 1-km DEM and is projected on the 5 km spaced mesoscale grid using area averaging (see Fig. 5.10). Figure 5.11 shows the elevation differences between the microscale and the mesoscale grids. The black areas in the figure show differences in elevations below -200 m. These areas are the original mountaintops that are being depressed through the conversion of a (relatively) real terrain to a 5-by-5 km spaced grid system. On the same grid, particularly where the land relief is more pronounced, such as along the Kluane Lake valley (Shakwak Trench), the mesoscale grid raises the land by over

Table 5.3: The land use data interpreted from the USGS satellite imagery is compared to the surface roughness observed and estimated in the field. The location of each station is identified on the satellite data interpretation map and the land use, surface roughness and vegetation description (referred to in Table 5.2) are extrapolated and shown in columns (2), (3), and (4). The observed surface roughness for each station was estimated by the first author through site visits and are listed in columns (5) and (6).

Column (1)	(2)	(3)	(4)	(5)	(6)
	According to satellite data interpretation			Observed in the field and estimated	
Wind Stations	Land use	z_o (m)	Vegetation type	z_o (m)	Vegetation type
Aishihik A	22	0.01	tundra	0.05	Open field with sparsely spaced shrubs
Burwash A	10	0.05	evergreen broadleaf shrub	0.1	Low-lying, field with nearby buildings and poplar
Faro A	22	0.01	tundra	0.1	Short grass field with nearby buildings and poplar
Haines Junction A	4	1.5	evergreen needleleaf tree	0.2	Low-lying field surrounded by spruce and buildings 200-500 m away
Kluane Lake A	10	0.05	evergreen broadleaf shrub	0.05	Open field with sparsely spaced shrubs
Teslin A	1	0.001	water	0.2	Short grass field with nearby buildings and poplar
Whitehorse A	6	1	deciduous needleleaf tree	0.02	Open field to the SE and NW
Sheep Look-out, Faro	22	0.01	tundra	1	Poplar and spruce mix forest to 10-m heights
Haeckel Hill	22	0.01	tundra	0.01	Hill top tundra and short shrubs
Destruction Bay	22	0.01	tundra	0.05	Short grass, undulating surface on bank exposed to prevailing wind
Bear Creek	4	1.5	evergreen needleleaf tree	0.01	Open short grass field on bank exposed to prevailing wind
Fox Lake	4	1.5	evergreen needleleaf tree	3.85	Mature spruce forest to 15-m heights
Carcross	22	0.01	tundra	3.55	Poplar forest average 6-m heights
Lake Laberge	10	0.05	evergreen broadleaf shrub	0.01	Small rocky hill, by lakeshore and exposed to prevailing wind
Marsh Lake	1	0.001	water	0.01	Beach sand on lake shore, exposed to prevailing wind
Paint Mountain	4	1.5	evergreen needleleaf tree	0.05	Hill top tundra and short shrubs
Jubilee Mountain	22	0.01	tundra	0.05	Hill top tundra and short shrubs
	Mean z_o:	0.42	Mean z_o:	0.55	

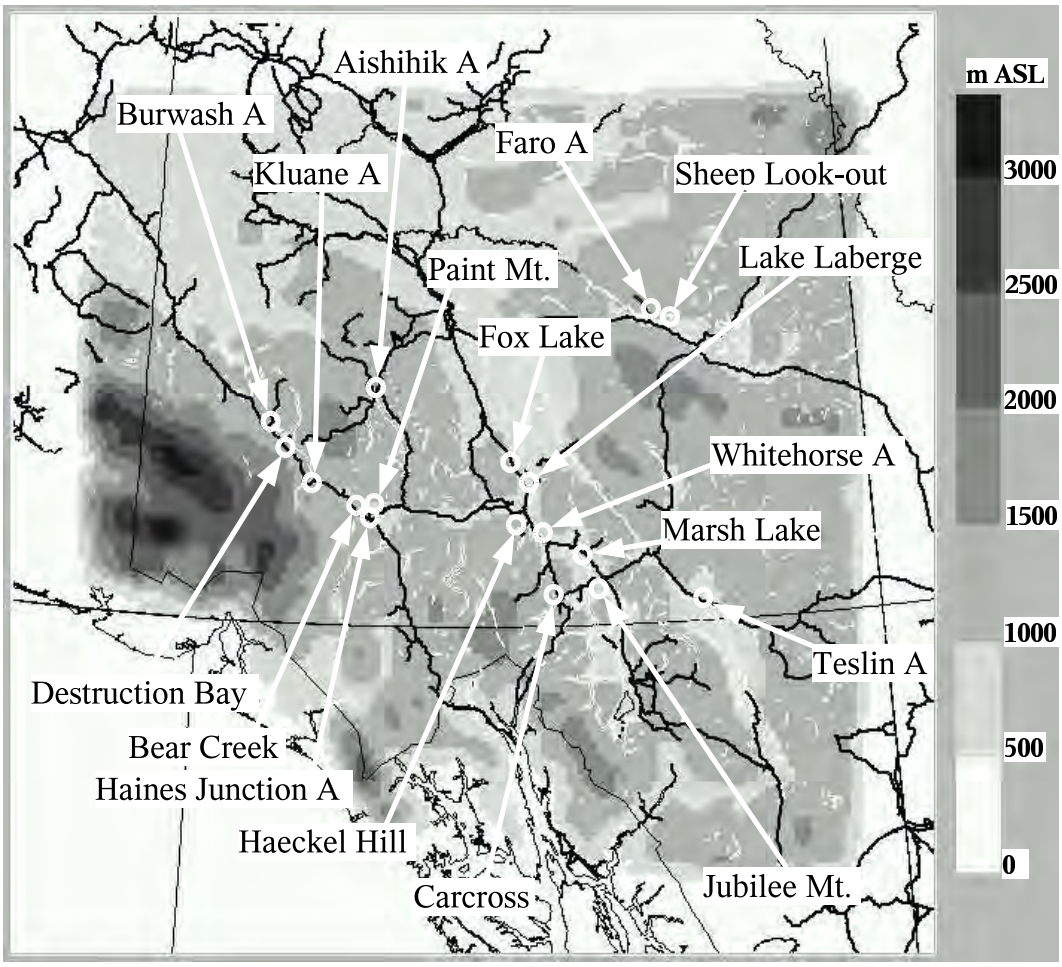

Figure 5.10: The DEM used for the MC2 simulation. The 5-km spaced grid shows a less detailed terrain than the microscale map of Fig. 5.2. The mountainous features are smoothed out in this map.

200 m. These elevation changes in the mesoscale model are clearly noticeable by the elevation differences noted beside each site name in Fig. 5.11. The sites that are in the valleys are raised, on average, 230 m from their original elevations. The three mountaintop sites (Haeckel Hill, Paint Mountain, and Jubilee Mountain) are depressed by an average of 440 m.

The Bear Creek site, in a valley, is raised by 316 m from its real elevation of 670 m. The Kluane site is raised 352 m in the mesoscale terrain model from its

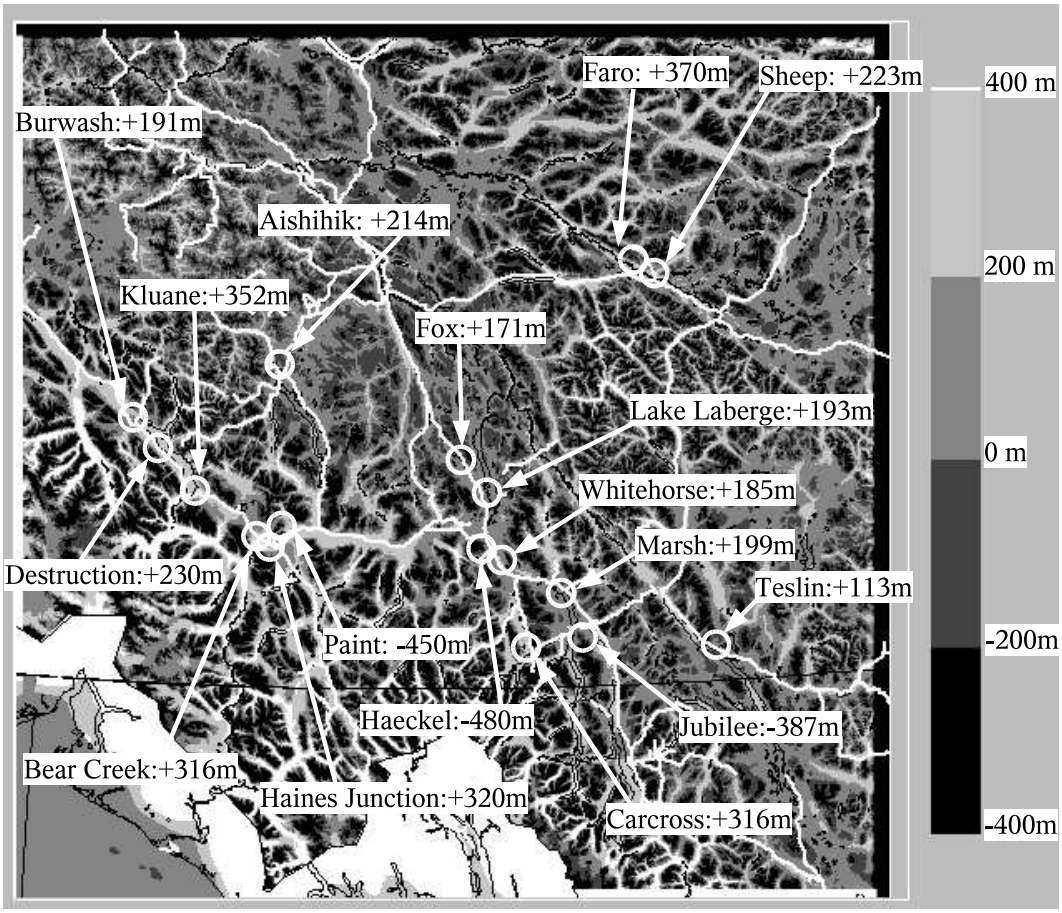

Figure 5.11: An elevation map depicting the difference between the mesoscale and the microscale DEMs. The darkest areas represent a drop in elevation of at least 200 m where the mountaintops are normally located. The valleys tend to be uplifted. The elevation changes are more pronounced in locations such as the Kluane Lake area where the land is lifted up by more than 200 m in the mesoscale model.

original height of 786 m. The model grid point at Aishihik is approximately 1180 m high whereas the actual site is at an elevation of 966 m, raising the site by 214 m in the model terrain. The mountains to the south of the Aishihik station and just north of Paint Mountain are at mostly 1500 m with peaks above 2000 m, whereas in the model, the highest terrain is below 1400 m. The hills surrounding the valley of the Aishihik site are smoothed considerably. Paint Mountain is reduced by about 450 m from the actual station height of 1370 m. The mesoscale map topography shows that the grid point representing Paint Mountain is still relatively high compared to the surrounding terrain.

The Front Range that lies immediately south-west along Kluane Lake is not resolved; its peaks of 2500 m are "washed out" into a mere slope between the ice fields and Kluane Lake with an average height of about 1500 m in the mesoscale map. The isolated mountain at the south-east end of Kluane Lake has, in reality, a vertical relief of at least 1500 m and this is shown in the microscale map. In the mesoscale map this mountain barely exceeds 500 m in relief. The differences between the site elevations as read from the NTS sheets and those of the microscale DEM are less dramatic. For the valley stations, there is a mean rise of only 26 m, and for the mountaintop sites, there is a mean drop of 67 m. In this same comparison the Haeckel Hill and Paint Mountain sites are prominent with elevation changes of about -134 and -176 m respectively.

d. *The grid set-up and simulations*

The MC2 mesoscale model domain covers a 500-km square portion of the southern Yukon. The grid has 151 $\times$ 151 points in the western and northern directions and each grid box is 5-km square in the horizontal direction, creating a 750-km square model domain. The domain becomes increasingly smooth beyond the 500-km model terrain, forming an "island" of a realistic Yukon topography in the middle of a flat plain. The DEM used for the MC2 simulation is shown in Fig. 5.10. The model's atmosphere is 20 km high and consists of 30 levels. Ten levels are below 1500 m, with the two lowest levels at 200 and 65 m above the surface.

The lateral boundaries of the MC2 model are open with inflow wind information being given at the four levels as described earlier; and the boundary values are time invariant. The upper and lower boundaries are solid. The lower boundary uses surface roughness information from the land use data. As indicated earlier, for the WEST simulations, most of the MC2 physics are inactive resulting in no surface radiation calculations but there is adiabatic boundary layer turbulent friction.

The MC2 model was run for each of the 162 wind climates for approximately nine hours of physical time. During each simulation the model terrain was initially flat and then increased to the full values over the first six hours. MC2 was set up in a time-independent mode and the remaining three hours were considered sufficient for the model to reach equilibrium. The output data for all 162 runs were compiled and made available for viewing and for input to MS-Micro.

The MS-Micro tiles have a full-width domain size of 42.5 km, with 128 points

in the x and y directions (grid spacing is 333 m). The full-width domain includes a flat plain surrounding the model terrain. The horizontal size of the terrain is usually half the width of the whole domain. Each microscale domain is centred at every third grid point of the mesoscale domain, that is, every 15 km. Each domain overlaps its neighbour by a ratio of 0.3, normalized on the half-width. MS-Micro is run in several directions at each of the mesoscale grid points used by the microscale model. The joint frequency table of mean wind speed for each of the directions produced by MC2 is applied to the MS-Micro results. The resulting mean wind speed for each direction is then weight-averaged to one mean wind speed at a given height for each microscale grid point. This averaged wind speed from MS-Micro is used for comparison with field measurements. The other statistics, such as the frequency and mean wind speed by direction, used for the wind rose comparisons, are obtained from the MC2 output. All microscale tiles are aggregated to produce a large microscale map covering the entire mesoscale domain. The DEM used for MS-Micro is shown in Fig. 5.2.

5.6. Results

The mean wind speed comparisons between the model and the field measurements are listed in Table 5.4. Here the stations are listed along with their elevations and tower heights in columns (2) and (3) respectively. Their mean wind speeds at, or projected to, 30 m are shown in column (4). Columns (5) and (6) show the model results from WEST (MC2 and MS-Micro) and from MC2 only. Column (7) shows the ratio of the WEST wind speeds to the measured wind speeds and column

(8) shows the ratio of the MC2 wind speeds to the measurements. The WEST simulation generally predicts higher wind speeds than those observed. As shown by the mean ratios (bold font) in columns (7) and (8) in Table 5.4, the wind speeds of WEST and MC2 are approximately double those observed at the airport wind monitoring sites. The same WEST and MC2 simulations predict higher wind speeds at the wind energy stations by a factor of 1.4 and 1.2 respectively. The standard deviations of the ratios between the WEST and MC2 models and the measurements are lower for the wind energy stations, with values of 0.2 and 0.3 respectively, than for the values measured at the airport stations, 0.5 and 0.7 respectively. The model also correlates much better with the wind energy stations with R = 0.95 and 0.80 respectively than with the airport stations with R = 0.49 and 0.12 respectively.

The two groups of stations were originally treated as one until the graph in Figure 5.12 revealed that there was (except for Whitehorse airport, Fox Lake, and Marsh Lake) a distinct difference between the wind speeds at the airport and the wind energy stations. A trend line is shown for each of those two groups; the grey line indicates agreement between the measurements and the model. Also shown on the graph are the total possible errors (vertical bars) due to vertical projection and period variability from long-term means. The error bars in Figure 5.12 (also refer to Table 5.1 and Section 5.3) show that some stations such as Whitehorse, Carcross, and Lake Laberge may likely match the model output if the measurements actually underestimate the true wind speeds. In the graph in Figure 5.12 it can be seen that the wind speeds from the WEST model agree best with the measurements from the Whitehorse airport and Haeckel Hill sites, giving higher speeds of about 10%

Table 5.4: The following is a comparison of mean wind speeds between the model and the field measurements. The two groups, the airport and the wind energy stations, are shown along with their elevations in column (2). The measurement heights are in column (3) and the long-term mean annual wind speeds are in column (4). These measurements are projected to 30 m using Equation 5.1 and the surface roughness information from the observed values in Table 3. Column (5) shows the results of long-term mean annual wind speed as modelled by MS-Micro from the output of MC2. Column (6) contains the values directly from MC2 projected to 30 m from 65 m AGL using Equation 5.1 and surface roughness values from the satellite data shown in Table 5.2. The last two columns are ratios of the model results of WEST (MC2 and MS-Micro) and MC2 respectively divided by the measurements.

Column (1)	(2)	(3)	(4)	(5)	(6)	(7)	(8)
	Height	Field Measurement		WEST	MC2	Ratio	Ratio
	ASL (m)	Projected from (m)	30-m Speed ($m\ s^{-1}$)	30-m Speed ($m\ s^{-1}$)	30-m Speed ($m\ s^{-1}$)	WEST/ Measured	MC2/ Measured
Airport							
Aishihik A	966	10	3.3	9.0	8.8	2.7	2.7
Burwash A	799	10	4.2	7.5	6.2	1.8	1.5
Faro A	694	10	2.7	5.6	5.9	2.1	2.2
Haines Junction A	599	10	2.3	5.3	5.6	2.3	2.5
Kluane Lake A	786	10	3.0	6.8	7.9	2.3	2.7
Teslin A	705	10	2.8	4.8	3.3	1.7	1.2
Whitehorse A	703	10	4.2	4.7	4.5	1.1	1.1
					Mean ratio model/field	**2.0**	**2.0**
					Standard Deviation	0.5	0.7
					Correlation (R):	0.49	0.12
Wind Energy							
Sheep Look-out, Faro	795	30	4.6	6.0	5.9	1.3	1.3
Haeckel Hill	1440	30	7.1	8.0	6.1	1.1	0.9
Destruction Bay	823	30	6.0	7.8	8.8	1.3	1.5
Bear Creek	670	26	5.0	6.4	5.3	1.3	1.1
Fox Lake	793	20	2.7	4.9	4.4	1.8	1.6
Carcross	702	20	4.1	4.8	4.8	1.2	1.2
Lake Laberge	645	10	4.5	5.6	4.9	1.3	1.1
Marsh Lake	656	10	3.0	5.4	3.9	1.8	1.3
Paint Mountain	1370	10	5.3	7.3	4.2	1.4	0.8
Jubilee Mountain	1280	10	4.3	5.9	4.1	1.4	1.0
					Mean ratio model/field	**1.4**	**1.2**
					Standard Deviation	0.2	0.3
					Correlation (R):	0.95	0.80

(also refer to Table 5.4). For the rest of the wind energy sites the model predicts higher wind speeds than have been measured by 20 to 30% — except for the Marsh Lake and Fox Lake sites by 80 and 100% respectively. WEST predicts higher wind speeds for the airport group of stations by 70 to 170% (factor 1.7 to 2.7 times).

Further analysis concentrating on the Kluane region shows an isotach of the long-term annual mean wind speed at 30 m AGL resulting from the WEST simulation (Figure 5.13). The map is overlaid with the locations of the wind monitoring sites along with their wind energy-frequency roses. As can be seen from the shaded areas on the isotach map, most of the stations in this region are predicted to have wind speeds in the 6 to 8 m s^{-1} range. The Aishihik airport site wind speeds are predicted to be 9 m s^{-1}.

The wind energy-frequency roses for the measurements (light shading Fig. 5.13) at the Burwash airport and Destruction Bay sites show that more than 70% of the wind energy is from the east-southeast to south-south-east directions, following the valley axis. At the same two locations the model (dark shading) predicts a bimodal distribution for the direction of wind energy; one that is roughly from the south-east, and the other from the south-southwest. At the Burwash airport site, the dominant south-southwest to southwest energy component predicted by the model represents 60% of the total energy. This dominant wind direction is not supported by the measurements and a generally accepted belief that winds follow the valley axis. Despite the erroneous southwest modes, the MC2 model shows that the southeast modes of the Burwash airport and Destruction Bay sites agree with the directions of both station measurements. The model predicts 1.8 and 1.3 times higher wind speeds for

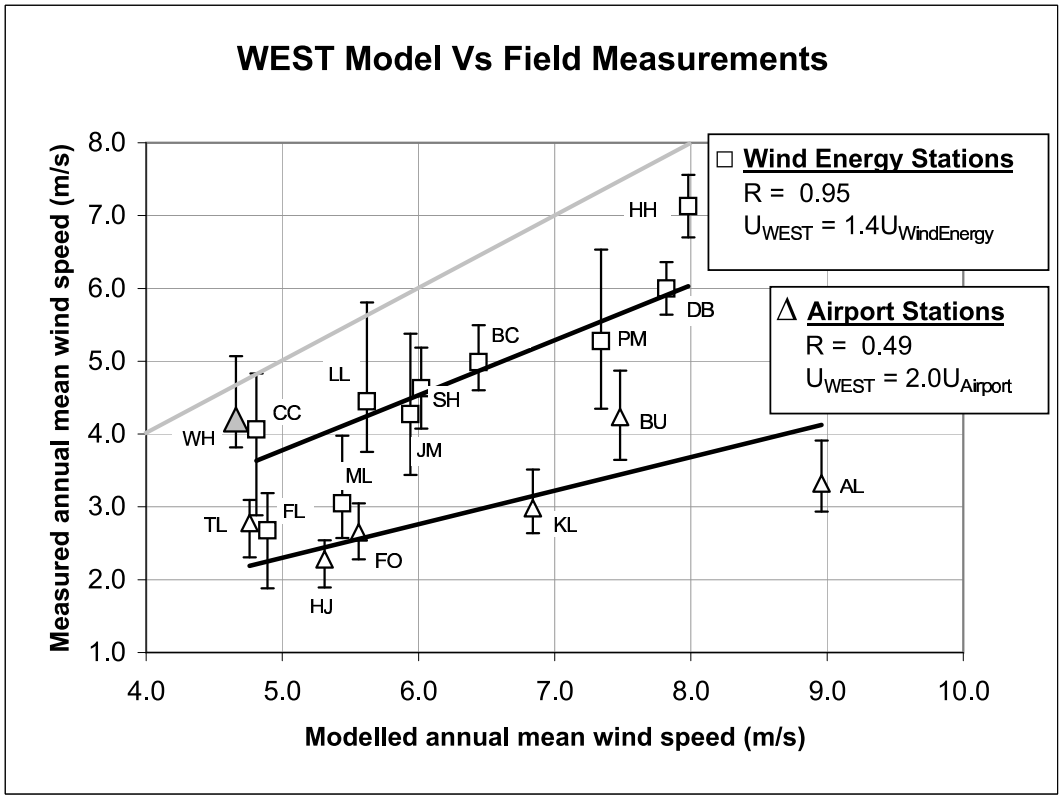

Figure 5.12: A graphical comparison between the WEST simulation and the measurements from the airport and the wind energy stations. Trend lines are associated (Whitehorse not included) with each group. The grey line indicates where the model would ideally conform to the measurements. The vertical error bars represent the total error (see Table 5.1) due to vertical projection and to a shorter monitoring period of the wind speed measurements. The WEST simulation predicts better results at the wind energy stations than at the airport stations: WEST simulates 40% higher wind speeds at the wind energy stations, whereas, at the airport stations it simulates 200% (double) of the observed wind speeds. Despite the strong bias, the wind energy group shows a much stronger correlation with the model than the airport group. The symbols representing each station are as follows: AL - Aishihik Lake, BU - Burwash, FO - Faro, HJ - Haines Junction, KL - Kluane Lake, TL - Teslin, WH - Whitehorse, SH - Sheep Look-out, HH - Haeckel Hill, DB - Destruction Bay, BC - Bear Creek, FL - Fox Lake, CC - Carcross, LL - Lake Laberge, ML - Marsh Lake, PM - Paint Mountain, JM - Jubilee Mountain.

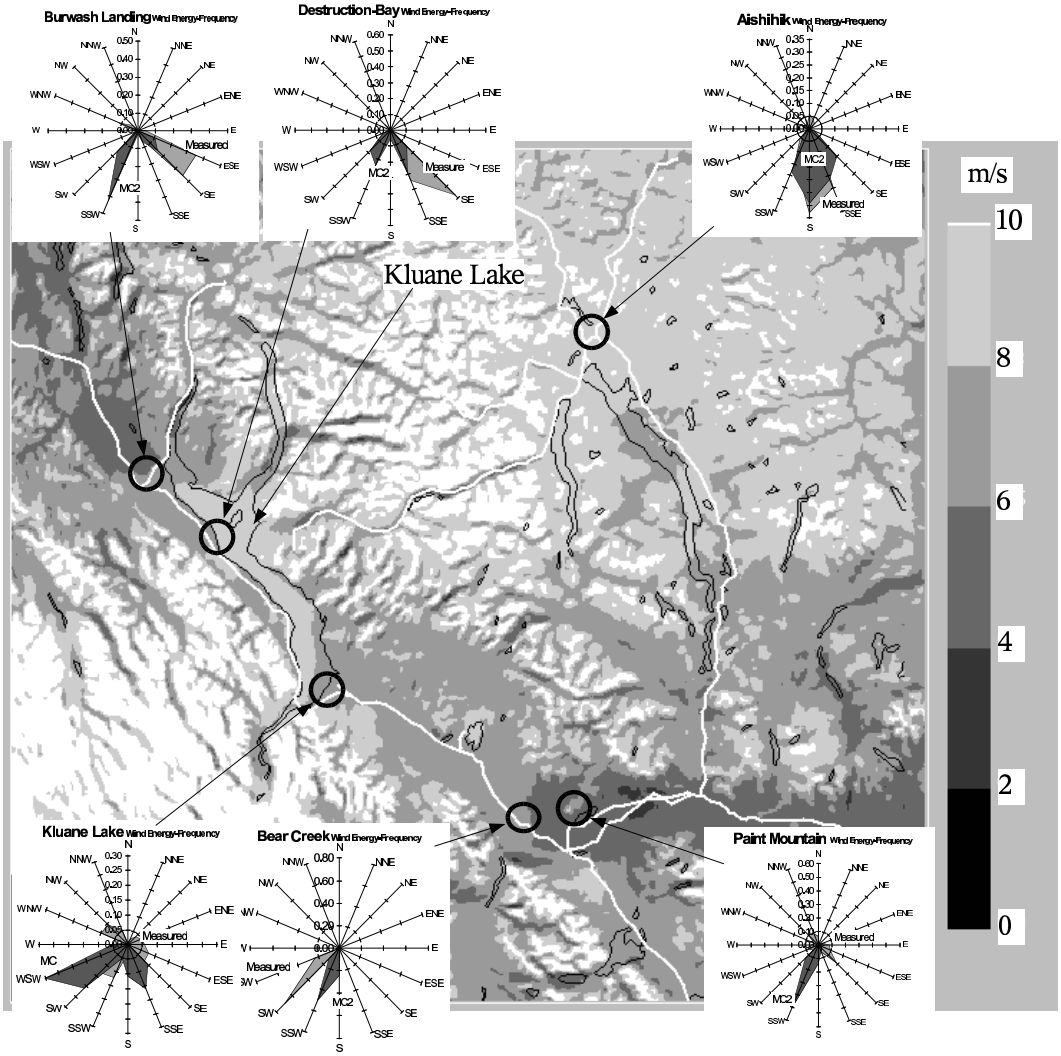

Figure 5.13: An isotach map of 30-m (AGL) long-term annual mean wind speed as produced by WEST for the Kluane region. The map is overlain by the sites of the monitoring stations along with wind energy-frequency roses for both the field measurements and the model. The roses representing the measurements are in a lighter shade and are overlapped by the MC2 output in the darker shade. For all of the stations in this region, except for Aishihik airport at 9 m s^{-1}, the WEST model predicts their wind speeds to be in the 6 to 8 m s^{-1} range.

the Burwash airport and Destruction Bay sites respectively.

The modelled rose for the Aishihik site in the north-east part of Fig. 5.13 compares very well with the measurements in terms of a southerly trend in direction. However, the wind speed comparison shows that the model simulates wind speed values which are 2.6 times the measured values. At Paint Mountain, the rose for the measured wind shows a small dominant east to south-east mode containing a little more than 40% of the wind energy and two smaller modes from the north-west and west-southwest. The model, on the other hand, predicts nearly 80% of the wind energy results from the south to south-west directions. MC2 predicts a lower wind speed at Paint Mountain by a factor of 0.8 but WEST predicts a higher wind speed by a factor of 1.4. The wind direction that the model predicts at Paint Mountain is similar to that of the Bear Creek site. At Bear Creek, the model predicts that almost 90% of the wind energy comes from the south to south-west, which is slightly more southerly compared to the measurements where about 95% of the wind energy comes from the south-west to west-south-west. MC2 predicts 10% higher wind speeds at the Bear Creek site, and WEST predicts 30% higher wind speeds.

The measured wind fields at the Kluane site showed three equally distributed modes in the south-west, south-east and north-west directions. At the same site, the model produced two modes similar to the Burwash airport and Destruction Bay sites. One mode has a more dominant component of 50% in the southwest and west-southwest directions and a smaller component in the south-southeast direction. Here the model more than doubles the wind speeds as measured at the Kluane site.

5.7. Discussion

The most important questions that arise in this study are why the WEST model predicts wind speeds which are 40% higher than the wind energy measurements and why there is a strong erroneous south-west wind component in the Kluane area.

One possible answer may lie in the mesoscale projection from the original DEM (the creation of a 5-km surface grid) which results in a smoothed topography. In the Kluane study area for example, nearly all of the stations in the mesoscale model are "lifted" (see Fig. 5.11) by at least 200 m in elevation. At the same time, some of the 2500-m peaks in the Front Range that lie immediately to the southwest, along Kluane Lake, become a simple 1500 m slope between the ice fields and Kluane Lake as a result of the smoothing. The flattening of the terrain relief is likely providing less orographic resistance and allowing strong winds into the raised valleys. The south-west wind component produced by the model in the Kluane Lake area, shown on the wind roses, results from flow through a non-existent Front Range.

The wind roses in Fig. 5.13 are overlaid on the mesoscale topography in Fig. 5.10 and are shown in Fig. 5.14, where it can be seen more clearly that the erroneous wind components modelled at each site in the Kluane region seem to point toward saddles in the smoothed mesoscale model terrain. At the Burwash, Destruction Bay, and Kluane Lake sites, those modes point towards a saddle on the east side of the St. Elias Mountains. At the Paint Mountain and Bear Creek sites, the modes point towards a much wider Alsek valley which is immediately to the south-west of these

sites. It becomes evident that the terrain has been smoothed so much that wind regimes occur in the simulation which are not seen in the observations.

Another possible explanation for the high wind speeds around the Kluane region could be due to the smooth surface roughness assigned over the ice fields to the south-west of Kluane Lake (see lower left of Fig. 5.9). The ice field is given a roughness of z_o = 0.001 m which is equivalent to that of water or smooth flat ice. This smooth surface, along with a modified DEM, could allow for stronger winds to flow over the ice fields and onto the areas immediately to the northeast.

There are other factors relating to the land use that may have an adverse influence on the wind fields around the sites of interest. This can be more of a concern when modelling and measuring at low levels such as 10 m AGL. However, we have allowed for large errors in estimating the wind speeds to the standard height of 30 m AGL due to errant local surface roughness and atmospheric stability and we have allowed for errors due to the variability of a short wind monitoring period mean to represent a long-term mean.

The discrepancy in wind speeds between the MC2 and the MS-Micro outputs may be due to the use of every third point of the mesoscale grid in the MS-Micro simulations. A mesoscale grid point used as nearest neighbour to compare a site may not be the same point used for the MS-Micro simulations. Although computer resources and time are saved by using every third point for MS-Micro, perhaps concentrating the microscale runs to every grid point in areas of greater interest may be a better solution to this particular modelling problem.

The same concept of grid concentration mentioned above, could be applied at

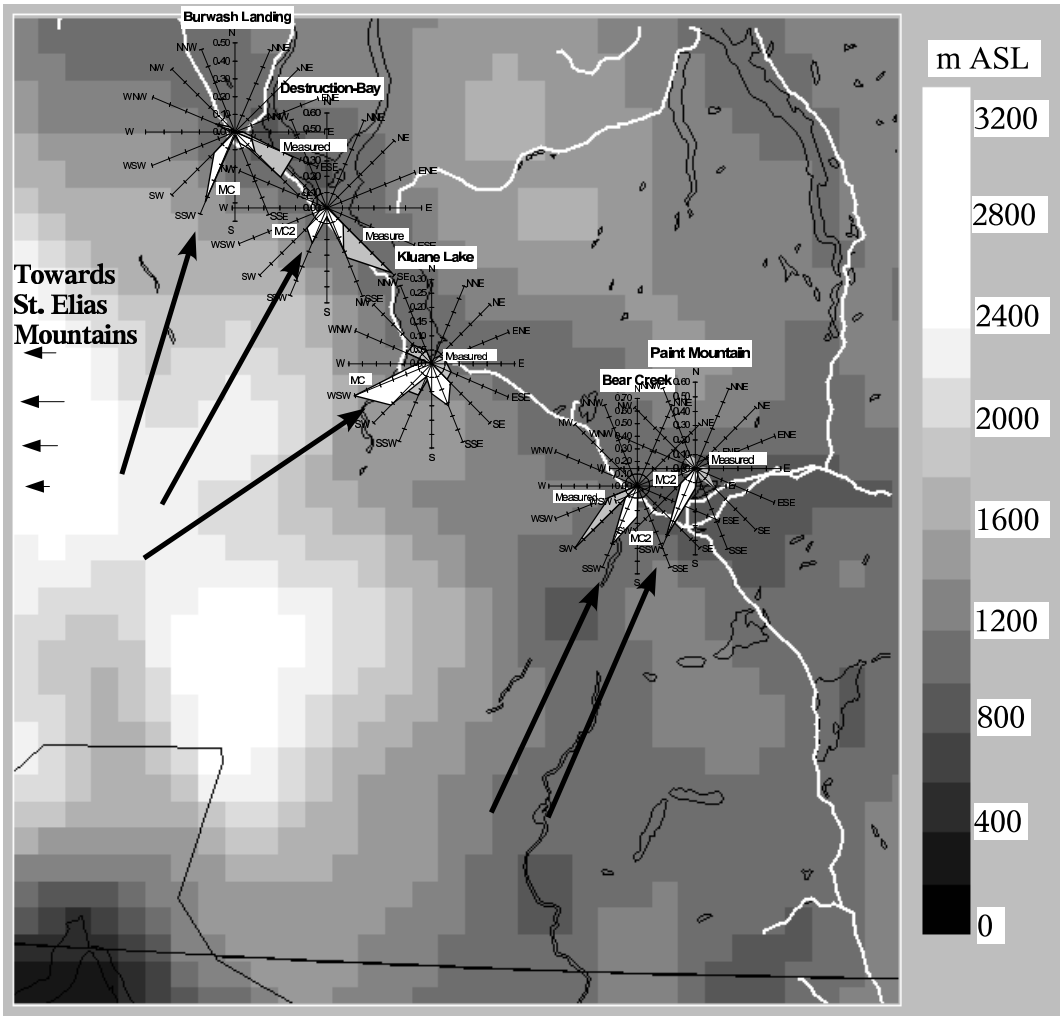

Figure 5.14: Wind energy-frequency roses overlain on the 5-km spaced mesoscale surface elevation grid of the same Kluane region shown in Fig. 5.13. Roses from the model results are white and those from the measurements are grey. The heights labelled in the legend are in metres ASL. The black arrows illustrate some of the wind directions from which the model predicts at each of the five sites.

the mesoscale level, where in areas of greater interest, a finer grid could be nested within the main grid. In the Kluane Lake region, a finer grid of say 1 km would likely resolve the Front Range in a more satisfactory manner in the mesoscale terrain. The MS-Micro runs likely do not need to be applied to every grid point. If a selection procedure could be developed to choose the grid points in areas of interest where results are most important, then this would maximize the use of the computer resources. These areas of interest are usually within a few tens of kilometres from power lines and communities.

It is possible that the high input (geostrophic) wind speed at sea level may contribute to simulated wind speeds which are too strong. The elevation in the mesoscale model is mostly 1000 m ASL and should cause the sea level winds to flow around the model topographical "island". This effect would need to be studied through a detailed look at a vertical profile of the wind roses around the island.

A possible problem that might be of concern in WEST is in some of the limitations of MS-Micro. MS-Micro is only capable of modelling terrain that has slopes of less than about one in four. While the mountains generally are within that limitation there are areas that are steeper. At most sites of interest, however, the mountain slopes seem to be within this limitation. In most cases, those mountains that exceed the slope limitation are not accessible for wind development. But at Destruction Bay, for example, the site is relatively close to the edge of an escarpment that has a slope of about one in two. Since the model grid is already quite coarse at 333 m, a sudden elevation change of about 40 m is smoothed to a very slight slope of about one in eight.

Another limitation in MS-Micro that could be a source of error, is the assumption of neutral stability. The neutral assumption implies a smaller wind shear; hence, a narrower vertical profile of horizontal wind speeds. Since wind speed inputs to MS-Micro are from higher levels such as 65 m AGL, this likely causes MS-Micro to predict higher wind speeds at lower levels. This also raises the question as to whether these stable atmospheric conditions are properly simulated in the MC2 model. The turbulence closure scheme in MC2 is designed to account for temperature profiles by means of a static stability function that is dependant on the Richardson number. In a future analysis it may be useful to produce outputs of vertical profiles of wind speed and temperatures to verify that this stability effect is occurring and properly influencing the simulated wind flows in the model. If the stability effect were accounted for in MS-Micro, as is apparently the case in MC2, then this effect should increase the wind shear, thus reducing the wind speed near the ground in the WEST simulation.

It is interesting to note the difference in the trends between the wind energy stations and the airport stations when comparing them to each other via the WEST simulations. Assuming that the wind energy group is the more correct one, and that the WEST simulation is accurate (although highly biased), the airport group then seems to underestimate wind speeds to about 60% (MC2 only) or 70% (WEST). It is not certain why there seems to be an underestimation by the airport stations but two possible reasons are suggested. The method for measuring wind speed on the hour by reading from a dial and recording on paper is prone to human error and could possibly underestimate the true wind speed. This underestimation could

be larger for those airport sites which take observations only during office hours. The other reason is that the airports, and their accompanying stations are typically "not" located in areas of high wind speed conditions, perhaps for safety reasons with regard to the landing of aircraft.

5.8. Conclusions

The mean annual wind speeds predicted by the WEST model, which couples MC2 and MS-Micro, at ten wind energy stations are higher than the measured annual wind speeds by about 40%. However, the correlation coefficient between the series of long-term mean wind speeds for the model and the wind energy stations is high, with a value of R = 0.95. The predicted wind speeds from the MC2 model used alone are only 20% higher than those measured at the wind energy stations.

The measured wind speeds at seven airport weather stations also used in the model comparison are approximately half of the wind speeds predicted by the model. The airport stations also have a poor correlation coefficient of R = 0.49 with the model. Interestingly, with the WEST simulation, most of the airport stations seem to measure wind speeds that are roughly 60 to 70% that of the wind energy stations. This discrepancy might result from airport stations being located in relatively sheltered areas and from the method in which wind data were measured and collected.

An examination of the wind roses for both the wind stations and the model output in the Kluane Lake region reveals some agreement with the measured wind directions following the valley orientations. Along Kluane Lake, however, the model

shows erroneous wind directions that are nearly perpendicular to the valley axis. The odd wind directions and strong wind speeds simulated by WEST may be most influenced by a modified and somewhat flattened terrain in the mesoscale elevation model. It is illustrated that in the Kluane region the erroneous directions seem to point to simulated winds flowing over saddles or passes through modified terrain east of the St. Elias Mountains. Other possible influences on the biased wind speeds in the model could be attributed to the following:

a Raised valleys and lowered mountains in the mesoscale terrain may increase simulated wind speeds in the valleys. The 5-km mesoscale grid may perhaps be overly smoothed in the conversion process. It would be useful to investigate the conversion process to find ways to reduce discrepancies between the original and the mesoscale terrain. This process may also be applicable to the microscale terrain.

b The assumption of neutral stability in MS-Micro may likely lead to predicted higher wind speeds in the model. Vertical wind shears in the more stable atmospheric conditions of the Yukon are higher, resulting in lower wind speeds near the ground relative to the winds above. This phenomenon needs to be verified in the MC2 model.

c The general application of MS-Micro to every third mesoscale grid point may be the cause of the deterioration of the MS-Micro wind speed results relative to MC2. If computer resources are a problem then it may be useful to allow the possibility that the microscale model can be applied to the nearest grid

point of a wind site of interest.

d Abnormally high sea level (geostrophic) wind speeds in the MC2 wind climate input may create high near-surface wind speeds in the MC2 simulations. This may or may not be an issue because the terrain in the model is raised to over 1000 m ASL and these sea level winds may be reduced by the terrain surface drag and diverged around the "island". It would be useful, however, to study vertical profiles and wind roses throughout the model atmosphere to determine the influence of the input wind speed used in the MC2 simulation.

e Mismatched land use at the model surface may cause errant wind speeds near the surface. In areas such as the Kluane ice fields, the smooth surface roughness may allow higher wind speeds over this area. The WEST is a promising candidate for providing solutions of the wind fields near the surface in the mountainous regions of the Yukon. However, the points noted above need to be investigated further to improve the model. The modified mesoscale terrain, in particular, needs the most attention. Any improvement in the grid's ability to represent the original terrain may provide the biggest improvement in the model's ability to simulate winds in mountainous terrain such as that of the Yukon.

Bibliography

Adrian, G. and F. Fiedler, 1991: Simulation of unstationary wind and temperature fields over complex terrain and comparison with observations. *Contributions to Atmospheric Physics*, **64**, 27–48, non-hydrostatic meso-scale meteorological model KAMM - Karlrushe Atm. ....

AES, 1976: Climatological station data catalogue. Technical report, Environment Canada, Downsview, Ontario, 34 pp.

— 1982: *Canadian Climate Normals Vol. 5 1951-1980*. Environment Canada, 283 pp.

Baker, D. R., 1995: Annual report wind monitoring and analysis. Technical report, Nor'wester Energy Systems Ltd., prepared for the Yukon Energy Corporation, Box 5920, Whitehorse, Yukon, Y1A 6S7, 350 pp.

Benoit, R., M. Desgagne, P. Pellerin, S. Pellerin, Y. Chartier, and S. Desjardins, 1997: The Canadian MC2: A semi-lagrangian, semi-implicit wideband atmospheric model suited for finescale process studies and simulation. *Mon. Wea. Rev.*, **125**, 2382–2415.

Benoit, R., W. Yu, and D. Lemarquis: 2001, Mesoscale mapping of the wind energy climate of Canada. *CANWEA 2001 Annual Conference*, 25.

Brower, M., J. W. Zack, B. Bailey, M. N. Schwartz, and D. L. Elliott: 2004, Mesoscale modeling as a tool for wind resource assessment and mapping. *14th Conference on Applied Climatology*, 8, found at ams.confex.com (American Meteorological Society).

Cottrell-Tribes, C., 2000a: Destruction Bay wind analysis. Technical report, Yukon Energy Corporation, John Maissan (Ed.), 11 pp.

— 2000b: Haeckel Hill wind analysis: December 1998 to October 1999. Technical report, Yukon Energy Corporation, John Maissan (Ed.), 26 pp.

— 2001: Phillips wind analysis: August 2000 - July 2001. Technical report, Yukon Energy Corporation, John Maissan (Ed.), 6 pp.

— 2002a: Abbott wind analysis: August 2001 - July 2002. Technical report, Yukon Energy Corporation, John Maissan (Ed.), 43 pp.

— 2002b: Lendrum wind analysis: August 2001 - July 2002. Technical report, Yukon Energy Corporation, John Maissan (Ed.), 24 pp.

— 2002c: Luet wind analysis: August 2001 - July 2002. Technical report, Yukon Energy Corporation, John Maissan (Ed.), 41 pp.

— 2003: Faro sheep site wind analysis: August 2000 to June 2002. Technical report, Yukon Energy Corporation, John Maissan (Ed.), 295 pp.

Elliott, D. and M. Schwartz, 1993: Wind energy potential in the United States. Published at www.nrel.gov.

Frank, H. P. and L. Landberg, 1997: Modelling the wind climate of Ireland. *Boundary Layer Meteorology*, **85**, 359–378.

Frank, H. P., E. L. Petersen, R. Hyvönen, and B. Tammelin, 1999: Calculations on the wind climate in northern Finland: the importance of inversions and roughness variations during the seasons. *Wind Energy*, **2**, 113–123.

Fuentes, U. and D. Heimann, 1996: Verification of statistical-dynamical downscaling in the alpine region. *Climate Res.*, **7**, 151–168.

Jackson, P. S. and J. C. R. Hunt, 1975: Turbulent wind flow over a low hill. *Quart. J. R. Meteor. Soc.*, **101**, 929–955.

Kalnay, E., M. Kanamitsu, R. Kistler, W. Collins, D. Deaven, L. Gandin, M. Iredell, S. Saha, G. White, J. Woollen, Y. Zhu, A. Leetmaa, R. Reynolds, M. Chelliah, W. Ebisuzaki, W. Higgins, J. Janowiak, K. C. Mo, C. Ropelewski, J. Wang, R. Jenne, and D. Joseph, 1996: The NCEP/NCAR 40-year Reanalysis project. *BAMS*, **77**, 437–471.

Mailhot, J., S. Bélair, R. Benoit, B. Bilodeau, Y. Delage, L. Fillion, L. Garand, C. Girard, and A. Tremblay, 1998: Scientific description of RPN physics library - version 3.6. Technical report, Recherce en Prévision Numérique, Atmospheric Environment Service, 197 pp.

Mason, P. and R. Sykes, 1979a: Separation effects in Ekman layer flow over ridges. *Quart. J. R. Meteor. Soc.*, **105**, 129–146.

Mason, P. J. and R. I. Sykes, 1979b: Flow over an isolated hill of moderate slope. *Quart. J. R. Meteor. Soc.*, **105**, 383–395.

Mortensen, N., L. Landberg, I. Troen, and E. Petersen, 1993: *Wind Atlas Analysis and Application Program (WAsP)*. Riso National Lab.

NG, 2002: Power till the cows come home - mapping Canada's winds help promote an underused energy resource. *National Geographic*, 2.

NRCan, 2000: Canadian digital elevation data - standards and specifications. Technical report, Natural Resources Canada, Geomatics Canada, Centre for Topographic Information Customer Support Group 2144 King St. West, Suite 010 Sherbrooke (Quebec) J1J 2E8, report available online at www.cits.rncan.gc.ca.

Pinard, J. D. J., 2001: Yukon wind energy potential, Bear Creek wind monitoring study. Technical report, Boreal Alternate Energy Centre, prepared for the Community Development Fund, Yukon Territorial Government, 16p.

Tanguay, M., A. Robert, and R. Laprise, 1990: A semi-implicit semi-lagrangian fully compressible regional forecast model. *Mon. Wea. Rev.*, **118**, 1970–1980.

Taylor, P. and H. Teunissen, 1983: Askervein '82: Report on the September/October 1982 experiment to study boundary-layer flow over Askervein, South Uist. Technical report, Environment Canada.

Troen, I. and E. L. Petersen, 1989: *European Wind Atlas*. Riso National Laboratory, Roskilde, Denmark, 656 pp., for the Commission of the European Communities ISBN 87-550-1482-8.

Vincent, M. and S. Fick, 2001: Who has mapped the wind? *Canadian Geographic*, 2.

Walmsley, J., P. Taylor, and T. Keith, 1986: A simple model of neutrally stratified boundary-layer flow over complex terrain with surface roughness modulations (MS3DJH/3R). *Boundary-Layer Meteorology*, **36**, 157–186.

Walmsley, J., D. Woolridge, and J. Salmon, 1990: MS-micro/3 user's guide. Technical Report ARD-90-008, Atmospheric Environment Services, 85 pp.

Walmsley, J. L. and R. J. Morris, 1992: Wind energy resource maps for Canada. Technical report, Atmospheric Environment Service, 53 pp.

Walmsley, J. L., J. R. Salmon, and P. A. Taylor, 1982: On the application of a model of boundary-layer flow over low hills to real terrain. *Boundary-Layer Meteorology*, **23**, 17–46.

WSD, 1977: MANOBS - manual of surface weather observations. Technical report, Weather Services Directorate, Environment Canada.

Chapter 6

Wind Climate of the Whitehorse Area

[1]

[1] A version of this chapter has been published. Pinard 2007. Arctic. **60**: 227-237.

6.1. Introduction

While the southern Yukon is energized mainly by hydro power, the territory's growing energy demand and the limited wintertime hydro availability are increasing the need for diesel-electric generation during the coldest months of the year. Diesel is an imported, non-renewable fuel that emits carbon dioxide gases and locally hazardous pollutants. The fossil fuel is transported from long distances and stored, adding further environmental risks. These drawbacks, combined with the rising cost of fossil fuel, are creating opportunities for wind energy. Wind energy complements hydro power because mountaintop winds increase markedly in winter, when the hydro-electric storage capacity is at a minimum. Two large commercial- scale wind turbines were installed on Haeckel Hill near Whitehorse in 1993 and 2000. Together, they have a capacity of 850 kW and have been feeding 150 residences year round. With the growing energy demand, new locations with greater wind potential are needed to accommodate the expansion of wind energy in the Yukon. Figure 6.1 shows a map of Whitehorse and its mountainous vicinity. The map also shows the power lines of the main electrical grid, along which wind energy development should focus. The terrain in the Whitehorse area ranges from 600 to 2500 m above sea level (ASL) with valleys oriented in roughly two directions: southeast to northwest (Whitehorse Valley) and east to southwest (Takhini River valley).

The most relevant criterion for new wind energy sites is that annual mean wind speed should exceed a threshold of 6 m s^{-1} (21.6 km/hr). From Pinard (2005), it is apparent that valley bottoms have less wind energy potential than mountaintops.

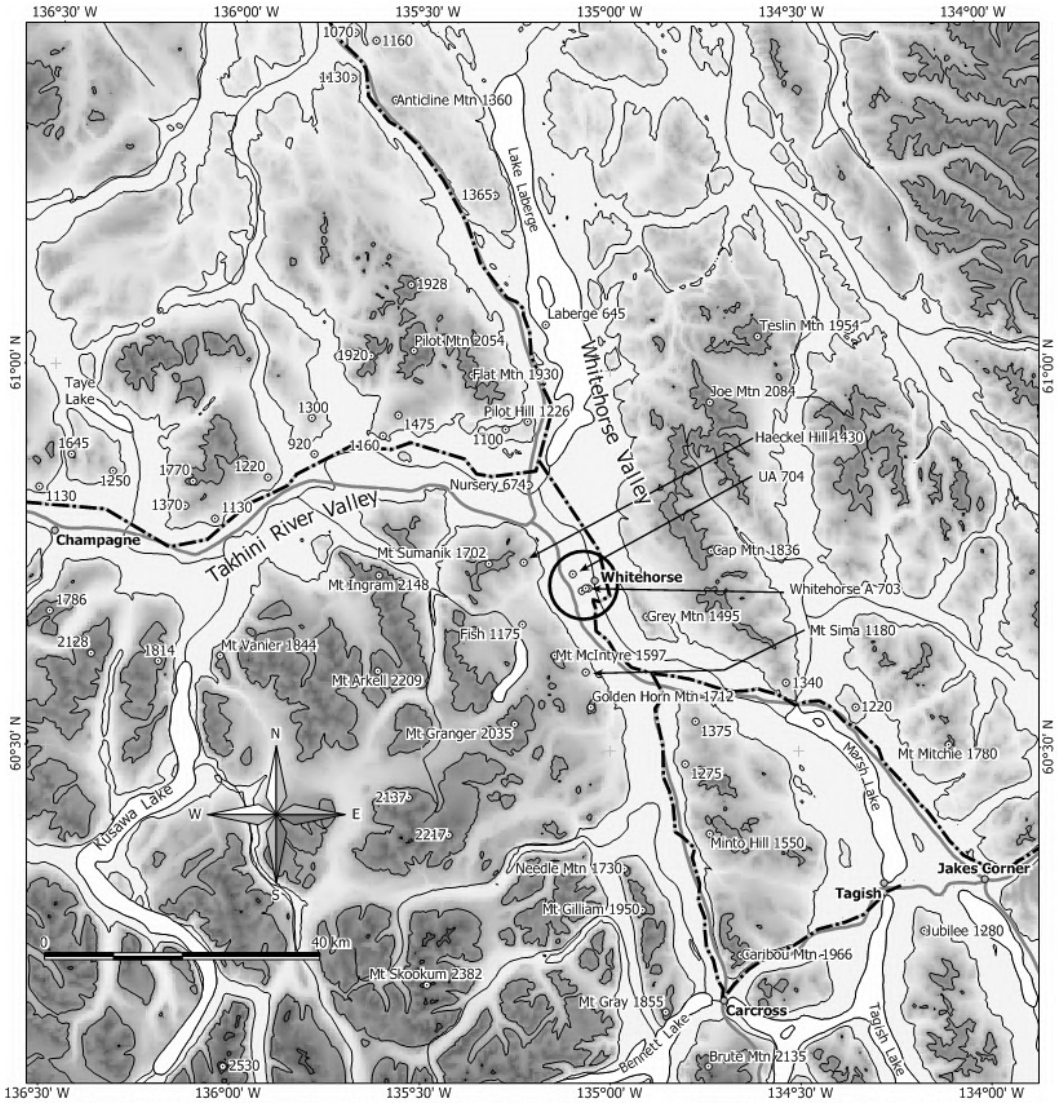

Figure 6.1: Map of the Whitehorse area, with contours at 900, 1500, and 2100 m ASL. Dash-and-dot lines indicate the approximate location of the power lines. Local peaks, isolated hills, and wind monitoring sites are identified by circle-dots and accompanying elevations (in metres ASL). The three successive locations of the three upper-air stations are within the circle. The first two locations were near the Whitehorse A station, and the present location is identified as "UA."

However, there are compelling reasons to find good windy sites at the lowest elevations possible. Haeckel Hill and the mountaintop sites are all prone to heavy rime icing in the winter. Anti-icing technology has been applied to the blades of the Haeckel Hill turbines, but it is desirable to avoid this rather expensive modification. Icing occurs during times when clouds form on Haeckel Hill (Maissan 2001), and anecdotal evidence shows less frequent cloudiness at lower elevations and perhaps less icing. Finding a windy hilltop within a valley requires an understanding of the predominant wind flows within and above the mountainous region.

According to Klock et al. (2001), the mean summer flows aloft (500 mbar) over the southern Yukon are southwesterly. In the winter, they are stronger and more westerly. While the winds at the Whitehorse airport and on Haeckel Hill were primarily from the south-southeast following the valley (Pinard 2005), Baker (1991) found that the prevailing wind direction was south-southeast at 1220 m ASL and shifted by 40 clockwise to south-southwest at 1830 m ASL. The relationship between winds aloft and those within the valley can be explained by a number of forcing mechanisms, two of which may be more relevant to wind energy applications in a mountainous terrain such as the Whitehorse area. The two are forced channeling of the downward momentum transport and pressure-driven channeling. These conditions are described in greater detail by Gross and Wippermann (1987) in their study of the Rhine Valley and by Whiteman and Doran (1993) for the Tennessee Valley.

Similar veering of winds was observed at Burwash Landing in the Kluane Valley, 200 km west of Whitehorse, in a 1977-78 winter minisonde study reported by

Faulkner (1981) and Nikleva (1979, 1984). The Kluane Valley is oriented northwest to southeast. In this study, low-level valley jets (local maxima in wind speed) were observed and typically occurred from the southeast at mid-height within the valley when winds aloft were from the southwest. The observed jets were 500 to 600 m below the top of the temperature inversion (height of maximum temperature). When the winds aloft followed the valley from the southeast, there was vertical momentum transfer into the valley (winds aloft mixing downward into the valley through turbulence), and no jet appeared. Nikleva (1984) noted similar results in a study at Beaver Creek, 150 km to the northwest, but the phenomenon was not as pronounced as the valley there was wider. Along the same valley system in Alaska, a study by Mitchell (1956) also described strong east-southeast winter winds similar to those at Burwash Landing. Valley jets may have important implications for wind energy in the Whitehorse region.

Although much research has investigated the forcing mechanisms of the low-level jet, no universally applicable paradigm has emerged. It is safe to say, however, that the phenomenon is closely associated with the occurrence of an inversion, which inhibits vertical momentum transfer and so decreases turbulent friction. The maximum wind speed (i.e., the nose of the jet) most often occurs below the top of the inversion. The existence of valley/ridge terrain (with associated pressure gradients and non-uniform cooling) further complicates the explanation (and modeling) of the low-level jet.

According to Wahl et al. (1987), the inversion cap (level of maximum temperature) in the Whitehorse Valley has typically been just below the mountaintops

(2000 m ASL) in the winter, but shallower inversions also occurred during summer nights. No valley jets have been reported in the Whitehorse Valley; however, Wahl et al. noted that super-gradient winds existed in mountain passes oriented along the prevailing pressure gradients.

While the above conditions may be relevant in the Whitehorse Valley, it is important to note that they might change with time. Evidence indicates that the Yukons climate is warming up and becoming windier. The Intergovernmental Panel on Climate Change indicated that the climate in the Yukon has been warming by 0.2 to 0.6°C per decade (IPCC 1998). Dormann and Woodin (2002) described climate models predicting trends in which winter temperatures are increasing more dramatically than summer temperatures. Graham and Diaz (2001) indicate that the winter cyclones have intensified over the North Pacific Ocean since 1948, causing increased wind speeds over the ocean surface. Hartmann and Wendler (2005) note that mean wind speeds in Alaska have increased because of the increasing difference in sea level pressure between the western North Pacific and western Canada. This change has also increased southerly winter winds, bringing more warm moisture from the Pacific to Alaska and Yukon.

The Whitehorse Valley wind climate is studied here using 50 years of wind and temperature data (weather balloon, radiosonde, sounding) from the local upper-air station. The upper-air measurements are also compared to those from local surface stations to construct an area wind climate model. The upper-air data is a twice-daily set of vertical profiles of horizontal wind information that may serve to answer some of the more relevant questions:

- At what elevations will threshold annual mean wind speeds for cost-efficient wind-energy production be attained? (i.e., where do annual mean speeds exceed 6 m s^{-1}?)

- How do the wind speed and the prevailing wind direction change with elevation and location?

- How are inversions factored into the above phenomena?

- How does the wind climate change with the seasons?

- Has the wind climate changed over the years?

Pinard et al. (2005) attempted to answer some of these questions using numerical modeling techniques, but with only a partial understanding of the relationship between the winds and the mountainous topography. The present study of Whitehorse upper-air data is intended to add to the existing knowledge base used to understand wind climate trends and patterns in the territory and other mountainous regions.

6.2. The monitoring stations

The surface stations used in this study are a combination from several programs of the Yukon Government (YG), the Boreal Alternative Energy Centre (BAEC), and the Meteorological Service of Canada (MSC; the Whitehorse airport and upper-air stations). The YG surface stations, Nursery and Mount Sima, were established for forest fire purposes, and the Laberge and Fish stations were part of a community wind resource assessment program. The BAEC surface stations, Haeckel Hill,

Mount Sumanik, and Flat Mountain (see Fig. 6.1), were all mountaintop sites, and their measurements (in contrast to the other surface stations) exhibited commercially feasible wind speeds. These three sites are given more attention in this study and are correlated against the measurements of the upper-air station.

All of the surface stations measured wind speed and direction with one- or two-second sampling rates averaged across 10-minute intervals (except the Whitehorse airport station, which had one-hour samplings). The monitoring from the YG sites covers periods of one to three years over the last ten years. Data from the Whitehorse airport, compiled for the period 1955-80, come from the Atmospheric Environment Service (AES 1982), now the Meteorological Service of Canada (MSC). Nearly all of these stations measured winds at 10 m above ground level (AGL hereafter). The period mean wind speed for each site was projected to a new wind speed at 30 m AGL using the logarithmic law and estimates of local surface roughness. The combined error in measurement, period variability, and vertical projection for these stations is about 20%.

At the three BAEC sites, measurements were taken for at least one year from 1991 to 1995, but these measurements were contaminated to some extent in the wintertime by mountaintop rime icing conditions. Approximately one year of ice-free wind speed and direction measurements were available for creating wind roses. For correlation with the upper-air measurements, two periods of uncontaminated measurements were extracted: June-August 1992 (88 days) for Mount Sumanik and Flat Mountain, and August-October 1994 (61 days) for Mount Sumanik and Haeckel Hill. The combined error in measurement, period variability, and vertical

projection for the BAEC stations is a maximum of about 10%.

The sounding data (radiosonde) used in this study are administered by NOAA (The National Oceanic and Atmospheric Administration, U.S. Department of Commerce, which administers sounding data for North America). Sounding data from other northern locations are briefly analyzed to compare trends with the Whitehorse analysis. Most of these soundings begin in the mid-1950s. For Whitehorse, the soundings date back to July 1955. The upper-air station was first established by the U.S. military during the Second World War and was taken over by the MSC in 1946. As of 1948, it was located at the Whitehorse International Airport on the east side of the runway (60.7157° N, 135.0626° W), in a field well exposed to both south and north. It was at 698 m ASL and well centralized in the valley. This location was also near the present-day location of the Whitehorse airport wind station. In 1962, the upper-air station was moved 950 m southwest across to the west side of the runway (60.7106° N, 135.07668° W, 704 m ASL). In 1996, the station was moved to its present location (60.7330° N and 135.0979° W, 704 m ASL), about 2.7 km northwest of its original airport site. It is in a small field, surrounded by a few buildings and sheltered by a small, forested hill about 300 m to the southeast.

A question arises as to how much the three moves affected wind speed measurements in the valley. Figure 6.1 shows a 10 km diameter circle encompassing the three sites (white circle-dots) that were home to the upper-air stations. The present site is northwest of the other two. Each balloon typically rises from the valley bottom to the mountaintop elevation (704 to 2200 m ASL) in about five minutes. The balloon climbs at rate of approximately 5 m s^{-1}, while its maximum mean hor-

izontal speeds rarely exceed 10 m s^{-1} at heights below 2200 m ASL. Therefore, the balloon is estimated to travel a maximum horizontal distance of 3 km in any given direction on its trajectory from surface to mountaintop.

The upper-air balloons have been released every 12 hours daily (approximately 3:00 AM and 3:00 PM Pacific Standard Time) and occasionally at six-hour intervals. In the early part of the NOAA data set, the occurrences of temperature and wind measurements are vertically distributed in the lower troposphere. In each sounding, however, the measurements do not appear consistently at fixed elevations; they are tied to mandatory pressure levels. Figure 6.2 shows two profiles of wind measurement frequencies. The one for 1956-60 shows an increased number of measurements at the surface, at 800 to 1000 m ASL, and roughly every 500 m above this. The 2001-05 profile shows wind measurements concentrated at 300 m intervals with very few measurements in between. The total number of wind speed measurements increased by 73% between the two periods. This increase had occurred by about 1988. Records of wind measurements at 914 and 1219 m ASL are common from 1998 on.

Although the pattern of temperature measurements was similar to that of wind speed measurements in the early part of the data set, the density and concentrations had not changed in recent years. The total number of temperature measurements actually decreased slightly between the two five-year periods. Errors in the sounding wind and temperature measurements are within 5% and 1% respectively (Golden et al. 1986). In this study, the measurements are interpolated to 100 m intervals. The wind speeds in the latter part of the data set are likely to be underestimated in

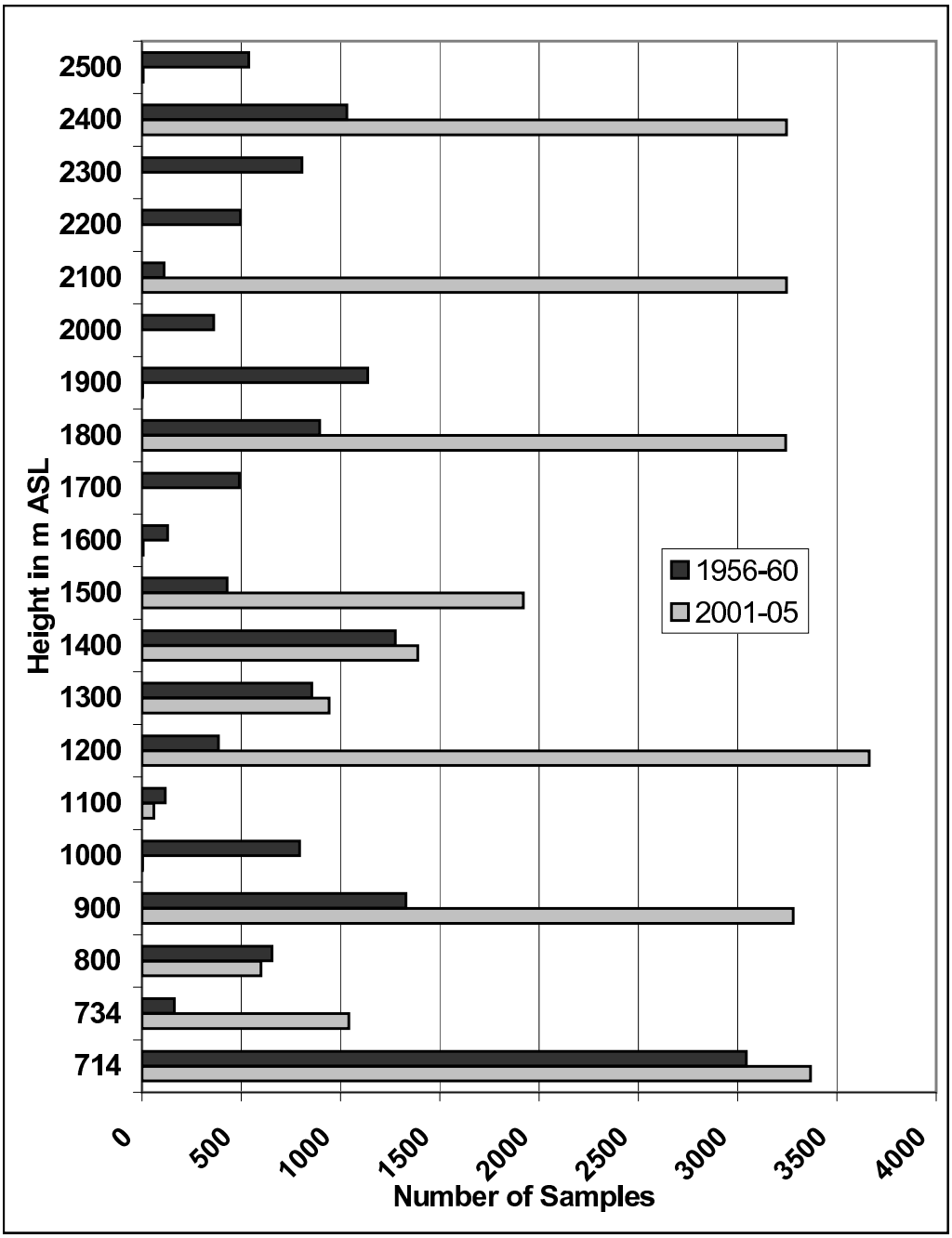

Figure 6.2: Occurrence of wind speed measurements with respect to elevation for the first five and last five years of the 50-year study period. For example, in 2001-05, 3280 measurements occurred between 900 and 1000 m ASL.

between the 300 m levels. This is especially likely in the lowest 200 m because of local surface obstructions and the reduced number of measurements in the first few hundred metres above the surface station.

6.3. Upper-air time series and surface correlations

Time series of annual mean wind speeds for the Whitehorse upper-air station, presented in Figure 6.3, show that the wind speeds have increased over the 50-year analysis period. A linear least squares method (LLSM) trend extending over the period shows the wind speeds increasing by about 1 m s^{-1} (0.2 m s^{-1} per decade) at 1200, 1500, and 2000 m ASL. These values represent an increase in wind speed of approximately 3% per decade at these elevations. Time series for the upper-air stations at Inuvik, Norman Wells, Fort Nelson, Prince George, and Yakutat also show wind speed increases (at 1200 m ASL) over the last 50 years. For the same period, the annual mean temperature at Whitehorse also increased (using LLSM) by 2.7° C at the surface and 1.0° C at 2000 m ASL. Record annual mean winds of 7.6, 8.0, and 8.8 m s^{-1} were attained in 1999 at 1200, 1500, and 2000 m ASL, respectively. Beginning in 2000, the annual mean wind speeds at 1200 m ASL were higher than those at 1500 m ASL. The five-year (2001-05) average at 1200 m ASL was 7.3 m s^{-1} (compared to 7, 6.7, and 6.4 for the 10-, 20-, and 50-year averages, all ending in 2005). A five-year moving average of the wind speed at 1500 m ASL reveals local minima in 1977 and 1997 and local maxima in 1963, 1988, and 2003.

The 2001-05 monthly mean wind speeds at mid to upper elevations show minimum winds in June and July and a maximum in December (Fig. 6.4). January

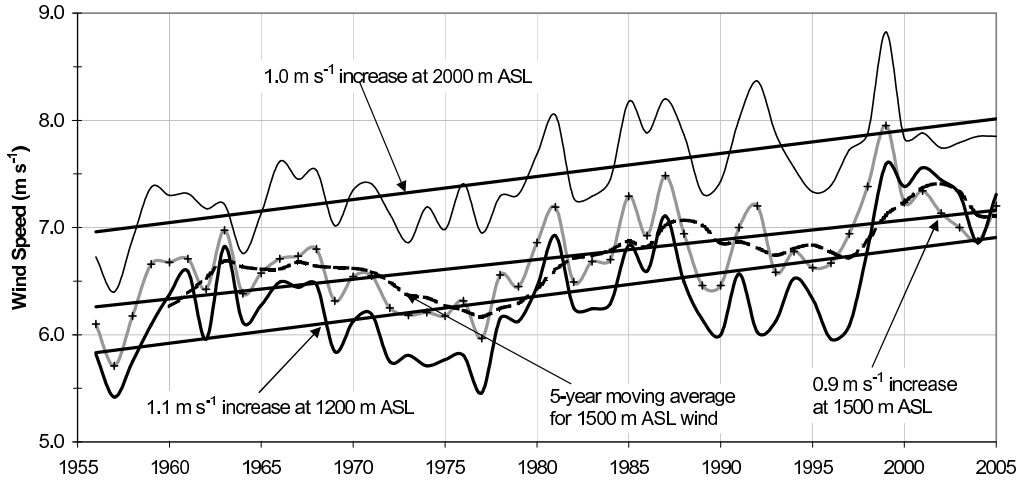

Figure 6.3: Time series of annual mean wind speed at three elevations (1200, 1500, and 2000 m ASL) within the Whitehorse valley. The trends at the three elevations were estimated using a linear least squares method fit to the data. A five-year moving average for the 1500 m ASL elevation is shown as a dashed line.

is the coldest and July the warmest month of the year, and this pattern has not changed over the 50-year period. At 10 m above the valley floor, or 714 m ASL, the wind speed varied slightly between 2.2 and 2.7 m s^{-1}. The wind speed at 900 m ASL (200 m AGL) varied from a minimum of 5.0 m s^{-1} in July to a maximum of 9.2 m s^{-1} in December. A drop in wind speed at 900 m ASL and at the surface is noticeable in January, when the winter inversion is typically deepest. The winds at 1200 and 1500 m ASL reached a minimum of about 5 m s^{-1} in June-July and maxima of 9.9 and 9.1 m s^{-1} respectively in December. The mean winds at 1800 m ASL (not shown) were similar to those at 1200 and 1500 m ASL.

A local wind speed maximum, or low-level jet, is apparent in Figure 6.4, where monthly mean wind speeds at 1200 m ASL surpass those at 1500 m ASL from

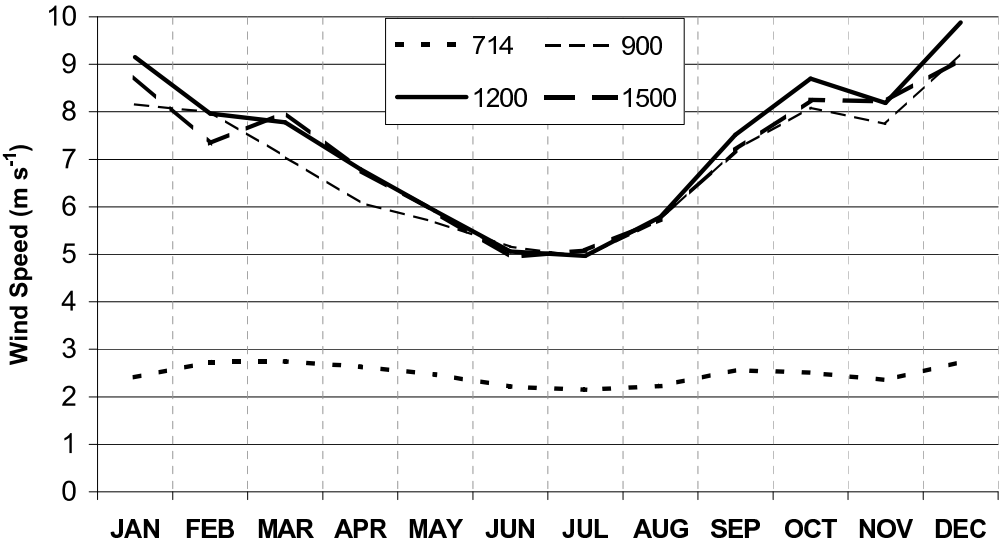

Figure 6.4: Monthly mean wind speeds for the period 2001-05 at 714, 900, 1200, and 1500 m ASL within the Whitehorse Valley. (The elevation 714 m ASL = 10 m AGL.)

September to February. As common as these jets seem to have become in the most recent five years, they have occurred regularly over the 50-year period. From 1956 to 1999, wind speeds at 1200 m ASL surpassed those at 1500 in 30% of the soundings released each year. During the period 2001-05, the jet occurred in 50% of the soundings. There are at least two possible explanations for this: an increase in sounding measurements near 1200 m ASL since 1998, and a substantial increase in lower-troposphere wind speed and pressure gradient after 1997.

Measurements from the three nearby mountaintop surface stations operated by BAEC are compared to those of the upper air at similar elevations. Mount Sumanik (24 m AGL, 1700 m ASL), Flat Mountain (18 m AGL, 1930 m ASL), and upper air (1700 and 1900 m ASL) measurements are compared for June-August 1992 (88

days). Haeckel Hill (30 m AGL, 1430 m ASL), Mount Sumanik, and upper air (1400 and 1700 m ASL) measurements are compared for August-October 1994 (61 days). The Pearson correlation (R^2) of the daily mean wind speed between Mount Sumanik and the upper air was 0.88 in 1992 and 0.94 in 1994. The corresponding correlation between Flat Mountain and the upper air was 0.70 in 1992; and that for Haeckel Hill and the upper air was 0.94 in 1994. Ratios of wind speeds between surface stations and the upper air were calculated as 0.95 for Haeckel Hill, 1.01 for Mount Sumanik, and 1.03 for Flat Mountain.

The surface station wind speeds were then projected to 2001-05, using the upper air measurements as a base line. Those projections resulted in wind speed estimates of 6.9 m s^{-1} for Haeckel Hill, 7.5 m s^{-1} for Mount Sumanik, and 7.9 m s^{-1} for Flat Mountain. Mount Sumanik and Flat Mountain wind speeds were projected to 30 m AGL from their measurement elevations using multipliers of 1.03 for Mount Sumanik and 1.07 for Flat Mountain. These multipliers were derived from the logarithmic profile law, using z_0 = 0.01 m. This estimate assumes a flow over a flat plain; however, it closely matches the Haeckel Hill profile. These projections resulted in wind speed ratios between surface and upper air stations of 0.95 for Haeckel Hill, 1.04 for Mount Sumanik, and 1.10 for Flat Mountain (estimated at 30 m AGL). At 30 m AGL, wind speeds were estimated as 7.7 m s^{-1} for Mount Sumanik and 8.4 m s^{-1} for Flat Mountain. The Haeckel Hill measurements by Yukon Energy that were made in 1998-2001 included the year 1998 with the record annual wind speeds. Projected to 2001-05, this sites long-term mean wind speed was approximated as 6.7 m s^{-1}.

6.4. Climatological vertical profile of upper-air wind speed

The 2001-05 annual mean wind speed above the Whitehorse station was 6.9 at 900 m ASL, 7.3 at 1200 m, 7.1 at 1500 m, and 7.3 m s^{-1} at 1800 m. A local maximum annual mean wind speed is evident at 1200 m ASL. Using linear interpolation, the minimum wind speed of 6 m s^{-1} is reached at about 150 m above the surface, or 850 m ASL. In Figure 6.5, vertical profiles of wind speed and temperature are classified into winter (December to February) and summer (June to August) means for two periods: 1956-2005 and 2001-05. The graph on the left shows significant increases in mid-valley wind speeds for 2001-05 compared to the 50-year average. Note the apparent quasilinear interpolations of the January 2001-05 profile between the surface, 900, 1200, 1500, and 1800 m ASL. The elevations at which most samplings occur (shown in Fig. 6.2) are evident here, and errors are expected to be larger between these elevations. It is therefore likely that a higher vertical density of measurements will produce different results from those described in the next paragraph.

From the 50-year to the five-year mean wind speed profiles, the maximum increases are at 900 m ASL, where the summer and winter winds show gains of 0.8 m s^{-1} and 2.2 m s^{-1} respectively. The winter profiles also show a significant increase of 1.5 m s^{-1} at 1200 m ASL. A low-level winter jet is apparent at this same elevation, and could also be said to exist in the summer profile at 900 m ASL. In the winter 2001-05 profile, the local maximum wind speed is 9 m s^{-1} at 1200 m ASL,

and the local minimum is 8.4 m s^{-1} at 1500 m ASL. This value is slightly lower than the wind speed of 8.5 m s^{-1} at 900 m ASL. In the summer 2001-05 profile, the wind speed reaches a local minimum of 5.2 m s^{-1} at 1400 m ASL and a local maximum of 5.4 m s^{-1} at 1000 m ASL. Note that at the surface the five-year mean wind speed is lower than the 50-year average. Mean wind speed was 4.2 m s^{-1} (10 m AGL) in 1955-79, but it decreased to 2.4 m s^{-1} in 1997-2005, after the upper-air station was relocated to its present, more sheltered location. Between 1979 and 1997, there was a significant lack of surface wind data.

The graph on the right in Figure 6.5 shows little change from the 50-year to the five-year mean summer temperatures, but a significant increase for winter. The summer profiles show that the mean summer atmosphere is conditionally unstable: the mean environmental lapse rates (rate at which air temperature changes with elevation) are less than the dry adiabatic rate, but more than the moist adiabatic rate. The winter profiles show that the atmosphere is absolutely stable, as the environmental lapse is less than the moist adiabatic rate. The five-year mean winter temperature, compared to the 50-year mean, is warmer by 1.5°C at 2500 m ASL and by 4°C at the surface. Time series (using LLSM) show that the mean surface temperature in January warmed by 9°C compared to less than 1°C in July. The winter profile for 2001-05 shows that the atmosphere below 2000 m ASL has become less stable. The mean elevation of the top of the wintertime temperature inversion has decreased from about 1900 m ASL in the late 1950s to 1200 m ASL in 2001-05. For the same period, the temperature inversion (based on monthly means) was more common in December and January and was most pronounced in January. In the late

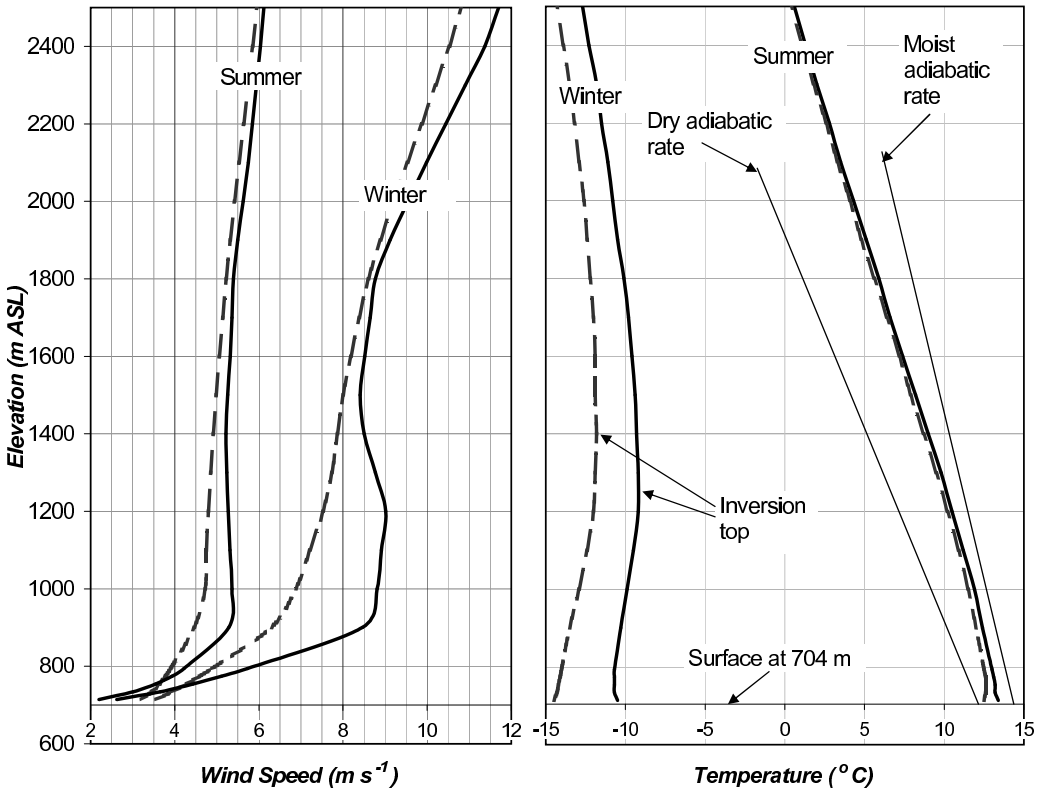

Figure 6.5: Vertical profiles of winter (December, January, and February) and summer (June, July, and August) mean wind speed and temperature for the 50- year period 1956-2005 (dashed line) and the five-year period 2001-05 (solid line). Graph on the right shows two reference lines: the dry adiabatic rate (10°C decrease per 1000 m rise) and the moist adiabatic rate (6°C decrease per 1000 m rise). The top of the temperature inversion (height of maximum temperature) is also identified.

1950s, the inversion appeared over a longer period: from November to February.

6.5. Geostrophic wind — valley wind relationship

A map of the vicinity of Whitehorse is shown in Figure 6.6, along with wind energy-frequency roses for the upper-air and local surface stations. The roses represent the relative amounts of wind energy that occur in each direction. The wind energy frequency is calculated as the product of the percentage frequency and the cube of

the mean wind speed for each direction, divided by the sum of those products in all directions. Compared to a simple wind frequency (occurrence) rose, this type of rose provides a better measure of the direction of the important wind energy. The upper-air roses in the upper right corner are for the period 2001-05; they do not vary substantially from the 50-year average.

At the bottom of the Whitehorse Valley, the Laberge, Nursery, and airport stations show predominant winds from the south-southeast, whereas the upper-air surface station shows predominant southerly winds. The airport station has the highest wind speeds of the four valley-bottom surface stations and is the most exposed. The wind direction of the upper-air surface station is affected by local topography, i.e., a small treed hill to the southeast and a north-south boulevard to the south. The upper-air winds at 900 (not shown), 1200, and 1400 m ASL were predominantly from the south-southeast, with over 75% of the wind energy from the southeast to south. The wind directions at 1200 m ASL were more narrowly focused than those at elevations above and below. The largest rate of change in wind direction with elevation occurred between 1700 and 1900 m ASL. At 2500 m ASL, the wind energy was predominantly from the southwest. From 1200 to 2500 m ASL, there is a veering of about 65° (clockwise looking from above) in the predominant wind direction.

Higher up in the valley, the Mount Sima station measured two main wind energy modes. One is from the southeast to the east of Mount Golden Horn (1713 m ASL) located directly south. The other mode is from the west-southwest between Mount McIntyre and Mount Golden Horn. The Fish station measured predominant

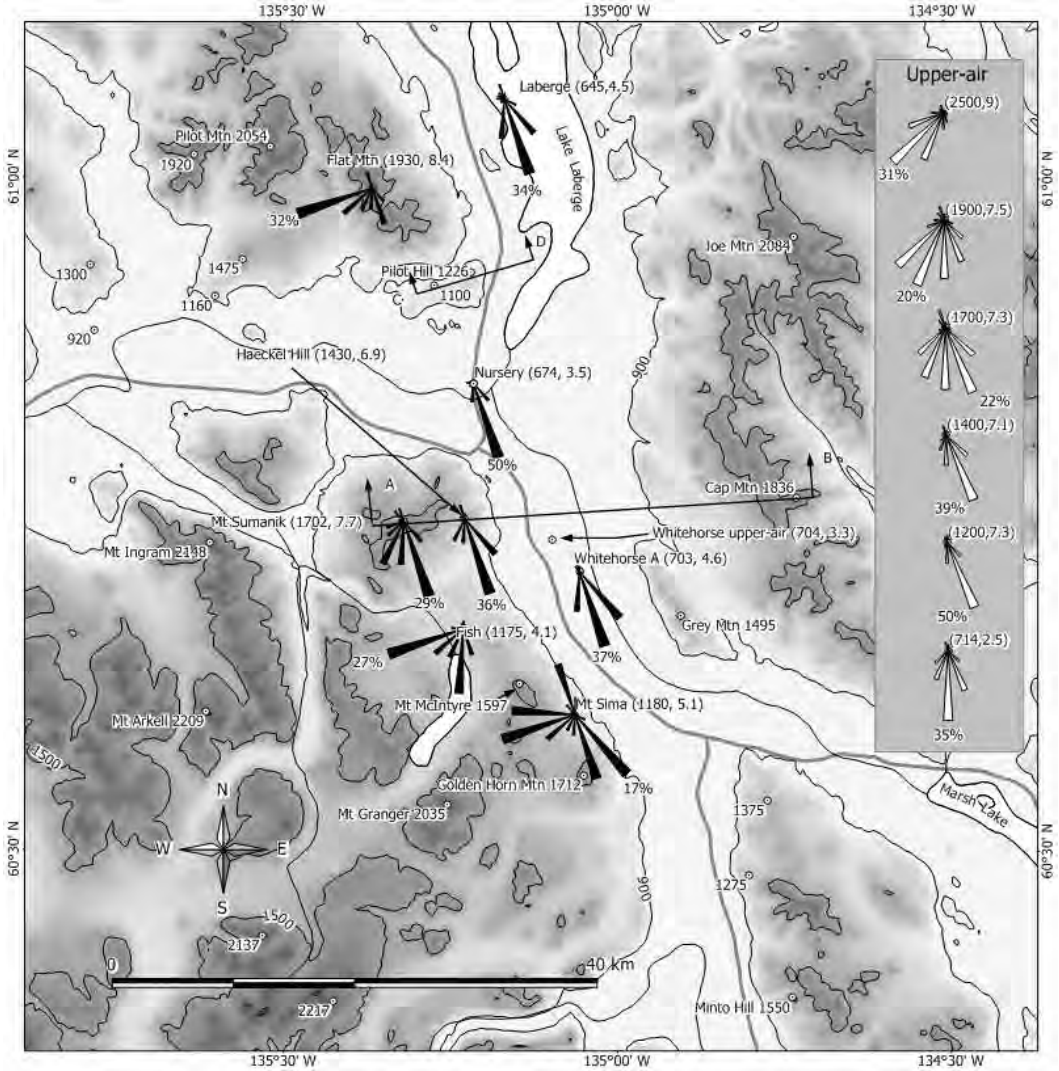

Figure 6.6: A relief map of the Whitehorse vicinity shows wind monitoring stations and their wind energy-frequency roses. The length of each rose arm represents relative wind energy-frequency by direction. The wind energy-frequency is calculated as the product of the percentage frequency and the cube of the mean wind speed for each direction, divided by the sum of those products in all directions. The direction with the maximum relative energy is identified with a % sign. The numbers beside each name are the site elevation in metres ASL and the mean wind speed estimated at 30 m AGL. The elevation contours are at 900, 1500, and 2100 m ASL.

winds from the west-southwest and although it is at the same elevation, it measured roughly 80% of the wind speed at Mount Sima. At the mountaintop elevations both Haeckel Hill and Mount Sumanik measured predominant south-southeasterly winds. While Haeckel Hill showed a tendency for more southeasterly winds, Mount Sumanik, 5 km to the west and 300 m higher, measured more significant winds from the south and south-southwest. Flat Mountain, across the Takhini Valley to the north, recorded winds that were primarily from the west-southwest, with a smaller mode from south-southeast.

The relationship between the winds aloft (geostrophic, above the mountaintops) and within the Whitehorse Valley is illustrated in Figure 6.7, using joint wind energy-frequency roses. The winds aloft (2400m ASL) are categorized into four wind direction quarters, two parallel to and two perpendicular to the valley. At 900 m ASL, the resulting joint wind energy-frequency roses show that winds aloft that are perpendicular to the valley are associated with valley winds that flow to the left (facing downstream of the winds aloft). Winds aloft that were parallel to the valley were associated with valley winds flowing in the same direction. When comparing the ratios of mean winds in the valley to those aloft, there appears to be little difference between the mean valley wind speeds relative to the mean winds aloft that are south-southeast (parallel) and west-southwest (perpendicular).

Figure 6.8 shows that when the winds aloft are from the west-northwest, two important direction modes appear within the valley. In this figure, the roses are further classified into summer and winter. The roses show that the prevailing summer valley winds are from the north-northwest. In the winter, however, the winds are

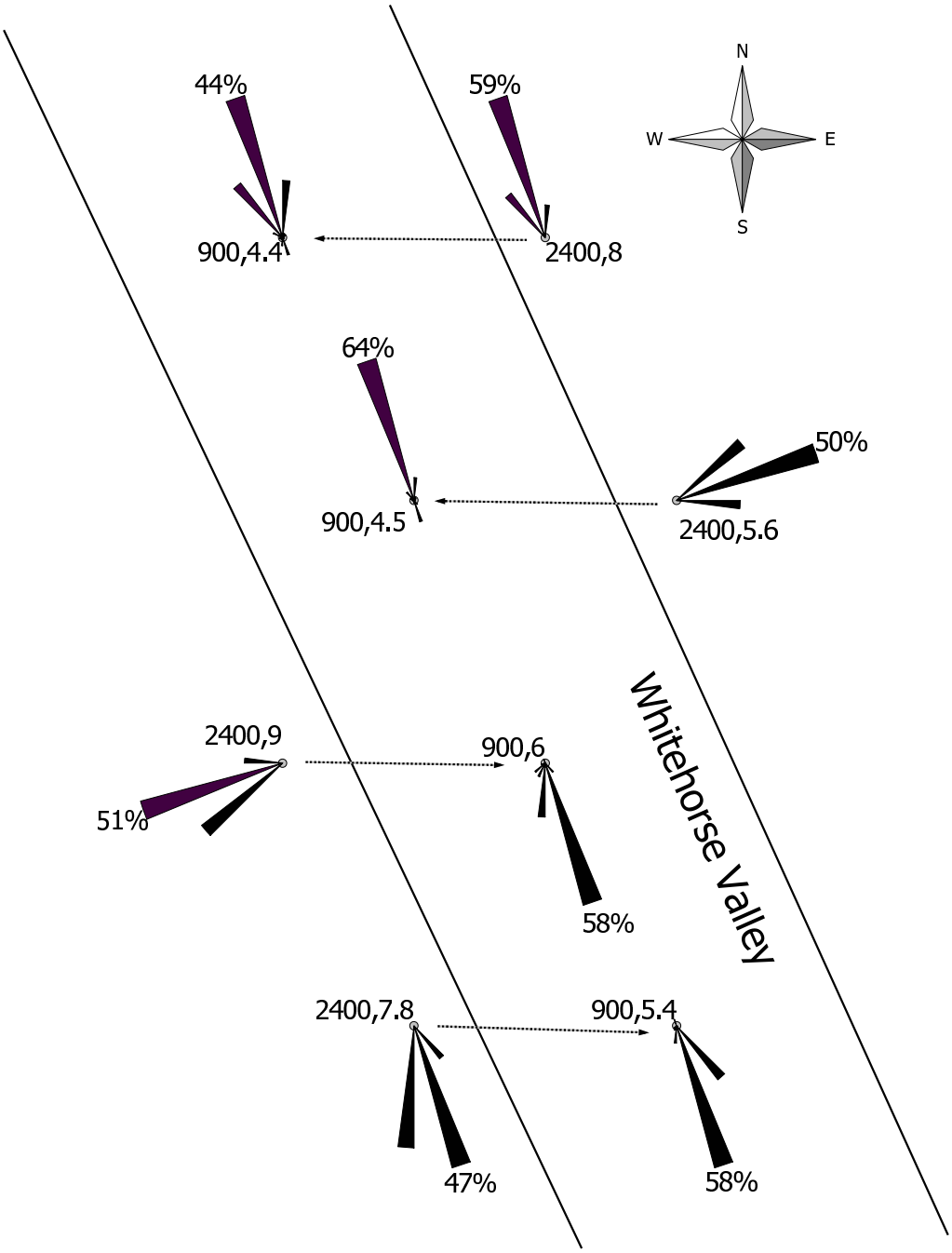

Figure 6.7: Joint wind energy-frequency roses of winds aloft and within the Whitehorse Valley for the period 1956-2005. The winds at 2400 m ASL are categorized into four quarters with respect to the valley. For each quarter at 2400 m ASL, the joint occurrence of the wind energyfrequency at 900 m ASL is shown within the valley outline. The valley is oriented north-northwest to south-southeast. The two numbers near the center of each rose represent the elevation and the mean wind speed for each category. At the end of the largest mode is the percentage of relative wind energy for that direction sector.

predominantly from the south-southeast. A wintertime countercurrent is evident here, and there is an apparent decoupling between the winds aloft and those in the valley.

Figure 6.9 provides a simple illustration of the forcing mechanisms that dominate according to the valley orientation with respect to the winds aloft. The valley that is parallel to the winds aloft experiences a forced channeling of valley winds through a downward momentum transport from the winds aloft. The valley that is perpendicular experiences winds that flow to the left (facing downwind aloft, in the Northern Hemisphere). This leftward flow is caused by high pressure to the right of the winds aloft, which drives the valley winds to the left, and it is also known as pressure-driven channeling. The right quadrant valley on Fig. 6.9 is a valley oriented to the right of the winds aloft (say -45°). In the right quadrant (in the Northern Hemisphere), the two forcing mechanisms are oriented in the same direction. In the left quadrant, however, the two forcing mechanisms oppose each other. As demonstrated in Figure 6.8, in the left quadrant, forced channeling is the dominant mechanism in the summer, while pressure-driven channeling dominates in winter. It is evident here that the temperature inversion must have a greater suppressing effect on the vertical momentum transport than on the pressure gradient. In all cases however, the mean in-valley wind speed is lower in winter than in summer. Further investigation of the relationship between the depth of the temperature inversion and the geostrophic and valley winds is merited.

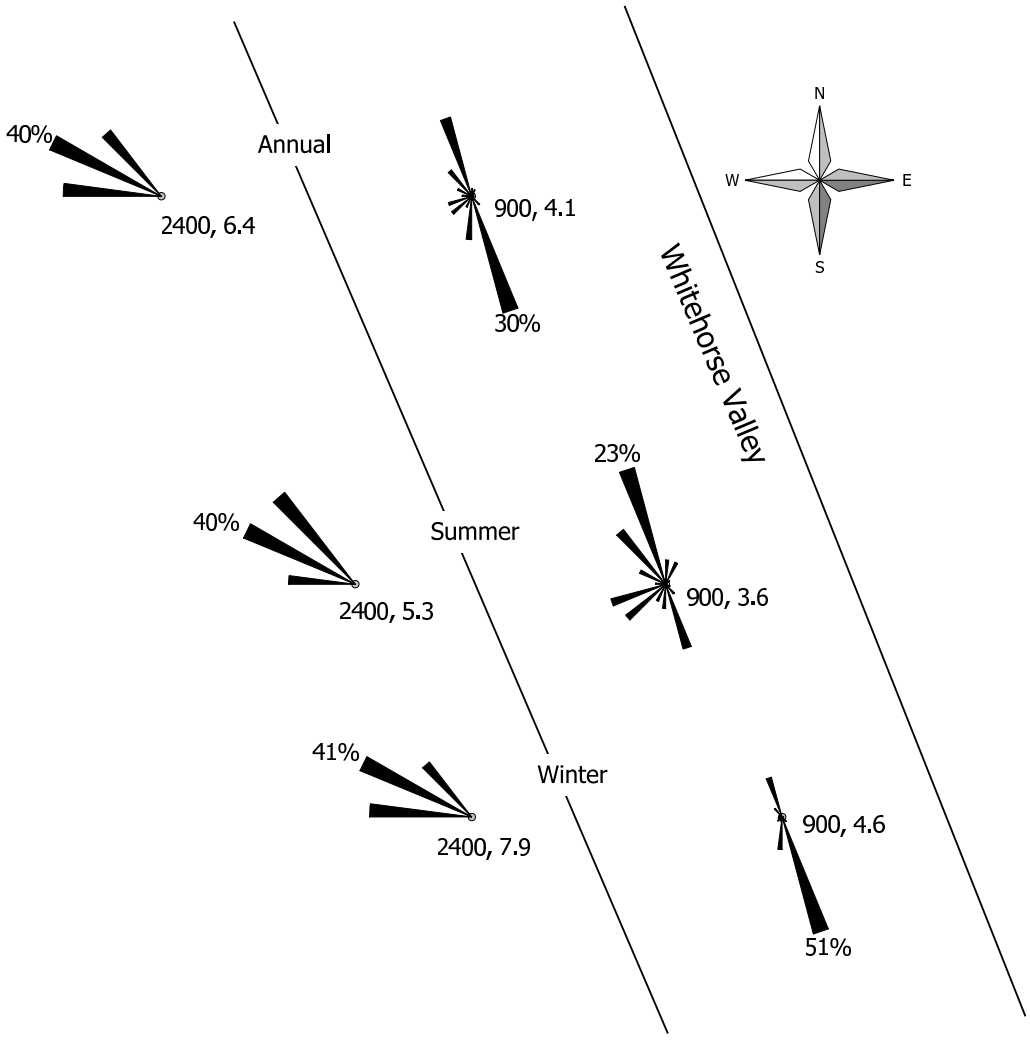

Figure 6.8: Same as Figure 6.7, except that the winds at 2400 m ASL are limited to 270-315 (west-northwest). The roses are classified into annual, summer (June, July, August) and winter (December, January, February).

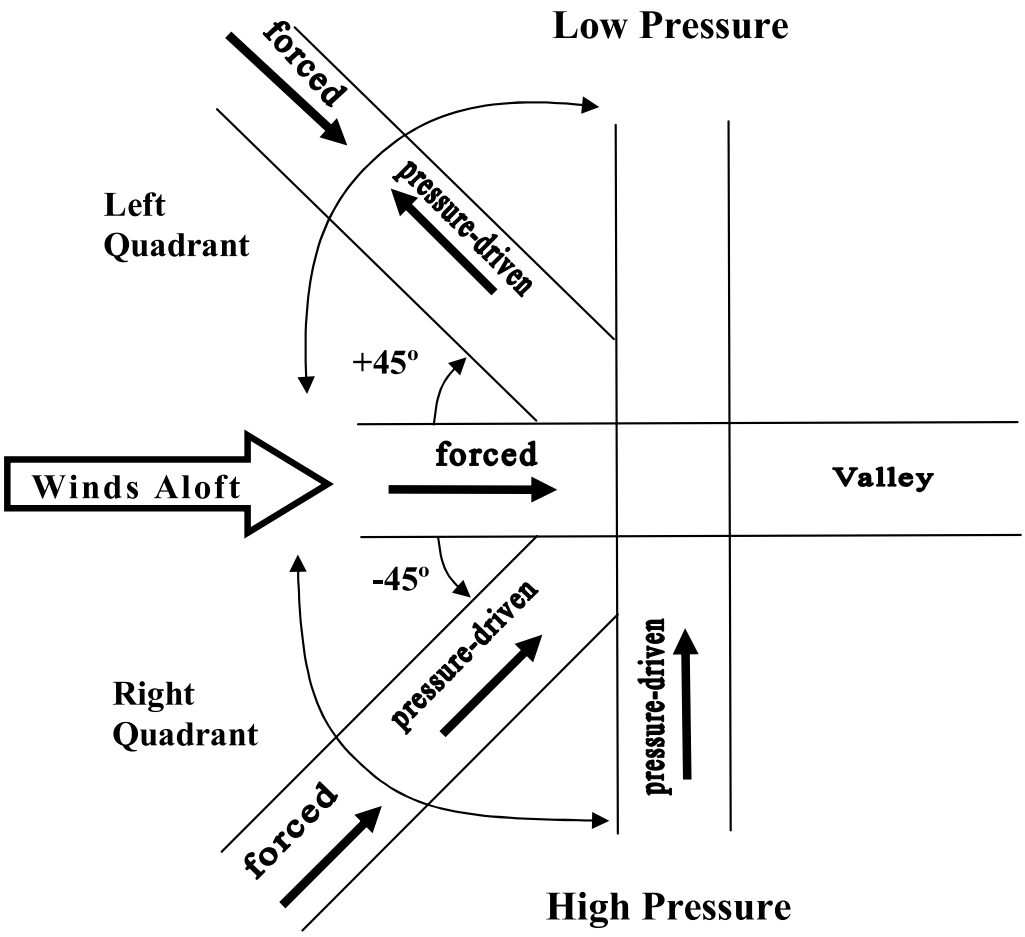

Figure 6.9: A relationship between the winds aloft (geostrophic winds) and winds within a valley of various orientations. Note that pressure is driven from high to low pressure, and "forced" refers to downward momentum transport by winds aloft.

6.6. Discussion

The positive trend in annual mean wind speed over 50 years suggests that wind farm economics are in the long run becoming more attractive. In the wintertime, the greater increase in mean wind speeds complements the seasonally higher energy demand. If the trend toward increasing wind speed trend continues at 3% increase per decade, then we could expect a growth in energy production of about 9% per decade. However, it is difficult to predict whether the trend will continue or has reached a climax. Since the record annual mean wind speed in 1999, there has been a (short-term?) decrease. The five-year moving average in Figure 3 suggests that this may be temporary. Since 1999, the increased mid-valley winds appear to be associated with a shallower winter temperature inversion. If the climate continues to warm, the temperature inversion will likely become even shallower. This will allow a greater influence of the forcing mechanisms presented earlier and hence promote higher wind speeds within the valley.

Figure 6.10 shows isotachs of annual mean wind speed overlying elevation profiles from cross-sections drawn across the Whitehorse Valley in Figure 6.6. It is clearly seen here that the elevation of 850 m ASL at which minimum annual mean wind speed (6 m s^{-1}) is achieved is relatively low in the valley. Towards the center of the valley there should be greater exposure to the main valley flow. This is evident in the higher surface wind speeds measured at the airport (see Fig. 6.6). The Laberge station, downstream from Whitehorse, measured similarly high wind speeds. We should then expect comparably high wind speeds in the upper air over

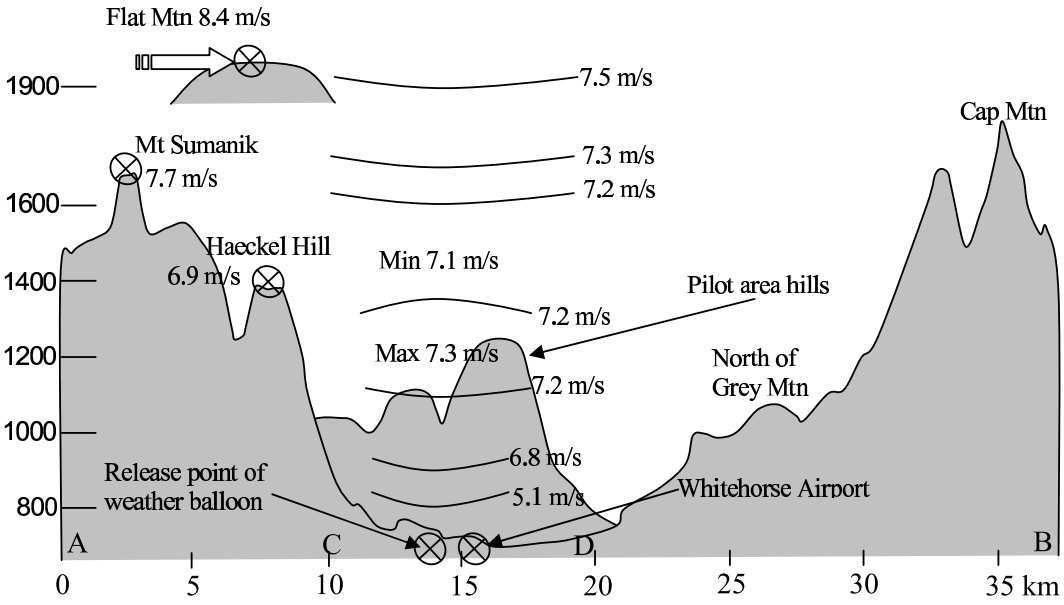

Figure 6.10: Elevation profiles along lines A-B, C-D in Figure 6.6 of the Whitehorse area valley, with isotachs of annual mean speeds for 2001-05. Flat Mountain is 28 km north of Mount Sumanik and 32 km north-northwest of the upper-air station. The Pilot area hills (line C-D) are about 22 km north-northwest of the upper-air station.

the Laberge station. The hills in the Pilot area range from 1100 to 1200 m ASL and could be considered prime candidates for new wind turbine sites, as they would be expected to have winds of at least 7 m s^{-1}. It is difficult to ascertain whether the winds here would be strictly from the south-southeast, or have a component from the west.

Upstream of Whitehorse, the Mount Sima station measured relatively lower winds, and this is caused by the shadowing effect of Mount Golden Horn upstream of the station. The Fish station is also in a sheltered location, being in a bowl surrounded by mountains in all directions but the east. Haeckel Hill may possibly experience the same wind shadow effects from Mount Golden Horn (1713 m ASL)

and Mount McIntyre (1598 m ASL), though less severely than Mount Sima.

Mount Sumanik is higher and more exposed, but it is still influenced by the predominant wind along the Whitehorse Valley. The range of mountains from Mount Granger (2035 m ASL) to Mount Ingram (2148 m ASL) must act as a barrier that redirects the winds observed at Mount Sumanik and the Whitehorse Valley. Two possible causes of the relatively higher winds at Mount Sumanik are the position of the station, on a long ridge perpendicular to the prevailing winds, and the Fish Lake valley to the southeast, which allows a long reach of undisturbed wind flow upstream of the Mount Sumanik site. Upper-air measurements of prevailing wind directions at the same elevation show relatively more winds from south and south-southwest than at Mount Sumanik. The upper-air measurements are made about 10 km east of Mount Sumanik and so are less influenced by the orographic barrier that affects Mount Sumanik.

With the predominant winds aloft from the southwest, we ought to expect that parallel valleys will experience valley winds from the southwest by downward momentum transport. The Takhini Valley (see Fig. 6.1), for example, has such an orientation between Pilot Mountain and Kusawa Lake. Flat Mountain provides a clue, as its predominant wind direction is along this valley. The west-southwesterly wind at Flat Mountain may be caused by a deviation of wind flow south of the massif of Pilot Mountain (2054 m ASL), which lies 9 km west-northwest (see Fig. 6.1). The winds at 1900 m ASL above Whitehorse are from the southwest, being less influenced by mountain barriers. It could be concluded that within the Takhini valley, the predominant winds are predicted to be from the southwest.

6.7. Conclusions

The Whitehorse upper-air measurements have been analyzed and found to correlate well with those from local mountaintop surface stations. The upper-air measurements indicate a 50-year increase in both temperature and wind speeds, and those increases are more profound in the winter. Above the upper-air station, viable winds occurred as low as 150 m above the valley floor, and a mid-valley jet was found to be a dominant feature. Winds within the valley were predominantly from the south-southeast, whereas above the mountaintops they were from the southwest. Surface stations open to the southwest recorded significant winds from those directions. Two dominant forcing mechanisms were identified: a downward momentum transport (when winds aloft were parallel to the valley axis) and a horizontal pressure gradient (when the winds aloft were perpendicular). The wintertime temperature inversion plays a role in reducing the vertical momentum transport, but winds that are dominated by or attributable to pressure-gradient forcing are affected only indirectly by stratification. Further studies are required to understand these interactions. Areas of high wind potential were identified for further exploration. Numerical modeling techniques are suggested as aids to locating sites of strong wind potential. The forcing mechanisms that drive the valley winds should be carefully considered in the parameter settings of numerical modeling.

Bibliography

AES, 1982: *Canadian Climate Normals Vol. 5 1951-1980*. Environment Canada, 283 pp.

Baker, D. R., 1991: Analysis of upper air wind speed and direction data collected at Whitehorse, Yukon, 1980 to 1989. Technical report, Nor'Wester Energy Systems Ltd., prepared for the Yukon Energy Corporation, Box 5920, Whitehorse, Yukon, Y1A 6S7.

Dormann, C. F. and S. J. Woodin, 2002: Climate change in the Arctic: Using plant functional types in a meta-analysis of field experiments. *Functional Ecology*, **16**, 4–17.

Faulkner, D. A.: 1981, A winter-time low-level jet in a Yukon valley. *Second Conference on Mountain Meteorology, November 1981, Steamboat Springs, Colorado*, American Meteorological Society, 36–39.

Golden, J. H., R. Serafin, V. Lally, and J. Facundo: 1986, Atmospheric sounding systems. *Mesoscale Meteorology and Forecasting*, P. S. Ray, ed., Amer. Meteor. Soc., 50–70.

Graham, N. E. and H. F. Diaz, 2001: Evidence for intensification of north Pacific

winter cyclones since 1948. *Bulletin of the American Meteorological Society*, **82**, 1869 – 1893.

Gross, G. and F. Wippermann, 1987: Channeling and countercurrent in the upper Rhine Valley: Numerical simulations. *J. Climate Appl. Meteor.*, **26**, 1293–1304.

Hartmann, B. and G. Wendler, 2005: The significance of the 1976 Pacific climate shift in the climatology of Alaska. *Journal of Climate*, **18**, 4824–4839.

IPCC, 1998: *The Regional Impacts of Climate Change: An Assessment of Vulnerability*. Cambridge University Press, Cambridge, UK.

Klock, R., E. Hudson, D. Aihoshi, and J. Mullock, 2001: *The Weather of Yukon, Northwest Territories and Western Nunavut*. NAV Canada, Ottawa, Ontario, 221 pp.

Maissan, J. F., 2001: Wind power development in sub-Arctic conditions with severe rime icing. *The Northern Review*, **24**, 174–183.

Mitchell, J. M., 1956: Strong surface winds at Big Delta, Alaska. *Mon. Wea. Rev.*, **84**, 15–24.

Nikleva, S., 1979: Environmental data study Alaska highway pipeline project report no.1a - minisonde data analysis - Burwash Landing Yukon. Technical report, Atmospheric Environment Service, 21 pp.

Nikleva, S.: 1984, Low-level jet in the Kluane Valley. *Meeting on Northern Climate, April, 1984, Whitehorse, Yukon*, 29–30.

Pinard, J. D. J.-P., R. Benoit, and W. Yu, 2005: A WEST wind climate simulation of the mountainous Yukon. *Atmosphere-Ocean*, **43**, 259–282.

Pinard, J.-P.: 2005, Wind climate of the mountainous Yukon. *New Northern Lights: Graduate Research on Circumpolar Studies from the University of Alberta*, Canadian Circumpolar Institute.

Wahl, H. E., D. B. Fraser, R. C. Harvey, and J. B. Maxwell, 1987: Climate of Yukon. Technical report, Environment Canada, Ottawa.

Whiteman, C. D. and J. C. Doran, 1993: The relationship between overlying synoptic-scale flows and winds within a valley. *J. Appl. Meteor.*, **32**, 1669–1682.

Chapter 7

Mesoscale wind modelling in steep mountain terrain

[1]

[1]A version of this chapter has been accepted for publication. Pinard Et Al. 2008. Atmosphere-Ocean.

7.1. Introduction

The mountainous Whitehorse region is being considered for wind project development to compliment the hydro-electric system in meeting Yukon's growing energy demand. The context of this paper is simulation of the long term mean annual wind energy climate over the Whitehorse mountainous region (see Fig. 7.3), using the statistical-dynamical downscaling approach to extract a high resolution local climate from the observed larger scale wind climatology. As the primary component of the wind energy simulation toolkit "AnemoScope[2]", the mesoscale model MC2 is used in the EOLE, or diagnostic mode over high resolution topography, to provide a wind field that is in equilibrium with boundary conditions derived from large-scale climate. Evidently then, these boundary conditions will be of crucial importance, and their optimal provision is the topic of this paper.

The standard procedure has been to set the boundary state using the mean geostrophic winds and temperatures defined by the NCEP/NCAR Reanalysis (Reanalysis hereafter; see Sec. 7.3 for full description); hundreds of such macroscopic climate states have been extracted from 43 years of global measurements (Kalnay et al. 1996). For any region of interest, the MC2 model is run to steady state for each of the relevant boundary states (if desired, each MC2 solution can be further refined on even higher resolution terrain, using a microscale simulation tool; however this is not relevant to the present work).

In Yu et al. (2006) the toolkit was used to simulate the wind climate in the

[2]Formerly called WEST; Wind Energy Simulation Toolkit, by RPN, Recherche en Prévision Numérique, Environment Canada.

Gaspé region of Quebec, over 90% of whose surface has an elevation lower than 1000 m ASL (above sea level). The resulting simulations produced near-surface winds that were in general agreement with the measurements. However when used by Pinard et al. (2005) to simulate winds over the Southern Yukon, where the terrain relief ranges from 600 m to over 3000 m ASL, a similar approach resulted in erroneous long-term mean surface wind directions in some major valleys and on nearby ranges: it was apparent that in the simulation, winds aloft had tended to mix down into the valleys, resulting in this unrealistic long term climatology.

A study of radiosonde temperature profiles from the Whitehorse upper-air station (Pinard 2007) made it clear that the temperature inversion is a dominant feature, and surely plays an important role in decoupling valley air from the winds aloft. Then in the absence of strong downward momentum transport, the pressure gradient is the main forcing mechanism in the channelled valley flow (eg. see Vogel et al. 1986; Gross and Wippermann 1987; Smedman and Bergström 1995; Bergström and Juuso 2006). In view of this, one avenue to improve the high resolution wind climate simulation would appear to be the provision of driving (boundary) states that are more strongly stratified. This is justifiable because the (true) long-term annual wind climate certainly is more heavily weighted by the strong wintertime winds than it is by the winds during the other (less strongly stratified) seasons.

The Reanalysis is universally available for mesoscale modelling and it is important to find ways to improve how it is used to provide the boundary conditions for MC2 and the Anemoscope toolkit. The form in which the Reanalysis has been used has produced rather weak lapse rates in the lowest portion of the model do-

main. In Figure 8 of Pinard et al. (2005) for example, the temperature lapse rates in the lowest 1500 m for the dominant winter profiles (bins) are approximately -6 $^{\circ}\mathrm{C\,km^{-1}}$ (potential temperature lapse rate of +4$^{\circ}\mathrm{C\,km^{-1}}$ in Fig. 8) compared to much stronger temperature inversions of +8 $^{\circ}\mathrm{C\,km^{-1}}$ measured by radiosondes at the Whitehorse station. Our objective is to show that the method by which the boundary conditions are derived from the Reanalysis may need to be modified to reflect the stratified nature of the atmosphere in mountainous terrain such as the Yukon.

In the following sections we show that an improved MC2 simulation of wind climate in the Yukon can be achieved, by supplying MC2 with a boundary wind profile that can be taken from the upper levels of the Reanalysis (above the mountaintops, where the wind is geostrophic), but a boundary temperature profile that reflects more closely those reported by the Whitehorse upper-air measurements. The altered constraining temperature profile results in altered orographic winds over the simulated terrain.

7.2. AnemoScope toolkit

The group RPN (Recherche en Prévision Numérique) of Environment Canada has developed tools to simulate wind energy in complex terrain. The latest development is AnemoScope, a PC-based wind simulation toolkit consisting of both mesoscale and microscale components. AnemoScope is the next generation of the wind climate mapping software called WEST (Wind Energy Simulation Toolkit) which is described in Pinard et al. (2005) and Yu et al. (2006). A user's guide to

AnemoScope is found in CHC&EC (Canadian Hydraulics Centre and Environment Canada, 2006). RPN has also developed the Canadian wind atlas (www.windatlas.ca) which is based on the same principles as AnemoScope, minus the use of the microscale component. The simulation statistics (as provided by MC2) are available at the wind atlas website, and users of AnemoScope can produce their own microscale simulations.

AnemoScope is based on a statistical-dynamical downscaling approach (Frey-Buness et al. 1995). The assumption is that regional climate is associated with a specific frequency distribution of basic large-scale weather situations or climate bins (see Sec. 7.3). Each climate bin is characterized by its vertical profiles of horizontal wind speed, of wind direction and of temperature, and used to initialize (and bound) a mesoscale simulation (MC2). The winds are initially treated as geostrophic and used to set the horizontal pressure gradient at all levels in the model. In the present AnemoScope parameterization the surface-layer wind is then modified to reflect surface conditions. Topography is introduced progressively during the model run, starting from a flat plain at sea level at initial time. With the lateral boundary conditions held constant, the interior high resolution climate corresponding to each macro-climate bin is simulated, by running MC2 for long enough to achieve a steady state (i.e. typically 6-9 hours of physical time, as opposed to computation time). The simulation resulting for each climate bin is weighted by the frequency of occurrence of that bin, to produce a bivariate frequency distribution (frequency distribution of wind by direction and wind-speed interval). The statistical result can be interpreted on its own, or can be used to initialize a high-resolution

microscale model at each mesoscale grid point. This method of initializing this mesoscale model is known as the EOLE mode of MC2.

MC2 is a compressible, non-hydrostatic, limited area model (Tanguay et al. 1990; Thomas et al. 1998; Girard et al. 2005)[3] that (in AnemoScope) is used in a diagnostic (i.e. steady state or EOLE) mode, to produce a three-dimensional atmospheric state reflecting (only) the specified lateral boundary conditions, topography and surface roughness: more specifically, other forcing mechanisms that would be an essential component of *weather* (as opposed to wind climate) prediction are excluded, e.g. surface-air energy fluxes, latent heating effects, clouds, etc. This exclusion allows the model to efficiently reach steady state and (more importantly) relieves the user of the need to provide unknown boundary values (of surface sensible heat flux density, etc). As a consequence of the simplification, the computed equilibrium state depends mainly on temperature stratification, pressure gradient, and windspeed (as controlled by the boundary profiles), on model topography and on resolution , whereas the influence of the initial state, many hours after initialization when steady state has been attained, is "forgotten". Owing to the neglected physical processes, certain mesoscale phenomena such as diabatic slope winds and land/lake breezes cannot be simulated, so that their influence is excluded from the computed long-term climatology. While these types of orographic circulations are (in and of themselves) usually too weak to produce significant wind energy, the

[3]The scheme of Girard et al. (2005) is implemented in the MC2 version used, which improves the dynamical handling of topography by providing a correct discretization of the (semi-Lagrangian) advection of the vertical velocity w: this prevents spurious spatial oscillations in the w field in the lower troposphere over complex and steep terrain, as explained in Girard et al..

neglected physical processes that give rise to them undoubtedly do modulate the strength of the wind; thus their neglect does to some degree compromise accuracy of the computed wind climate.

MC2 being a fully non-linear finite difference model, reducing the horizontal grid spacing below (say) 1 km necessitates greatly increased computer resources to deal with the rapidly increasing number of grid points and smaller time steps. To overcome this practical limitation, a microscale model, MS-Micro (see Walmsley et al. 1990) is coupled to the MC2 output, to simulate winds at a finer resolution. Based on linearized equations of motion and a semi-analytic solution method, MS-Micro can simulate winds at a grid resolution of order tens of metres. Since this study concerns a mesoscale atmospheric flow, MS-Micro is not utilized here: we are trying to solve a problem present in the mesoscale part of the overall downscaling process of AnemoScope.

7.3. NCEP/NCAR Reanalysis extracted for driving MC2

The large scale climate classification driving MC2 is derived from a global 43-year (1958-2000) long term data set provided by the NCEP/NCAR[4] Reanalysis (Kalnay et al. 1996) on a latitude-longitude grid spaced at 2.5° intervals, and covering pressure levels from sea to 10 mb level. The procedure used by AnemoScope (i.e. to drive MC2) is to extract from the Reanalysis a set of wind climate bins, classified according to the sea-level pressure gradient (which can be considered to imply a fictive sea-level geostrophic wind speed and direction), and the vertical shear of

[4]National Centers for Environmental Prediction / National Center for Atmospheric Research

wind speed between 0 and 1500 m ASL.

There are 14 speed classes (2,4,6...30, and $>34\ \mathrm{m\,s^{-1}}$), 16 direction sectors, and two shear classes (positive or negative, shear not significant for wind speed less than or equal to $2\ \mathrm{m\,s^{-1}}$), resulting in (a maximum of) 432 bins at each lat/long node. Each bin has its own characteristic one-dimensional atmospheric state, as defined by averaging wind speed, direction, and temperature over all weather situations in the Reanalysis that conform to that bin. Each mean weather situation (bin) is interpolated to four tropospheric pressure levels (1000, 850, 700, 500 mb), and these profiles are mapped onto the MC2 coordinate by assuming these 'mandatory levels' correspond to 0, 1500, 3000, 5500 m ASL.

In the Southern Yukon the 2.5° grid spacing implies that nodes are spaced roughly 130 km apart in the east-west direction and 275 km apart in the north-south direction. The climate table used to simulate the Whitehorse wind climate is that associated with a node (Table no. 61/90) located at 61.25° North and 136.25° West, about halfway between the Champagne and the Braeburn measurement sites (marked in Fig. 7.3). The climate table for this node contains 287 climate bins occurring with non-zero frequency.

7.4. Comparing Reanalysis to observations

The input wind data from Table no. 61/90 of the Reanalysis are summarized in Table 7.1, along with observations from the Whitehorse radiosondes. The annual mean temperature profile according to the Reanalysis (Figure 7.1) reveals a mean temperature lapse rate of - 6.7 $\mathrm{K\,km^{-1}}$, corresponding to conditionally unstable

Table 7.1: Comparison of the Reanalysis and the radiosonde measurements in the Whitehorse area for the (43-year) period 1958-2000. The Whitehorse radiosonde station is at 704 m ASL at the bottom of a south-southeast oriented valley. The Reanalysis is a forty-three year mean annual climate for node 61/90 (Whitehorse region, see Fig. 7.3), formed as the weighted mean of the 287 bins pertaining to that node. The winds at given elevations [m ASL] are considered geostrophic for the Reanalysis. Please note that the sea-level wind is fictional.

	Elevation:	0		1500		3000		5500	Units
Reanalysis	Variable								
	Wind Speed	10.1		6.0		4.8		6.3	$\mathrm{m\,s^{-1}}$
	Wind Direction	ESE		SSE		S		SSW	
	Temperature	279		269		262		246	°K
	Lapse Rate		- 6.7		- 4.0		- 6.4		$\mathrm{^{\circ}K\,km^{-1}}$
	Elevation:	714		1500		3000		5500	Units
Radiosondes	Variable								
	Wind Speed	2.4		6.8		9.7		13.6	$\mathrm{m\,s^{-1}}$
	Wind Direction	SSE		SSE		SW		WSW	
	Temperature	274		271		263		247	°K
	Lapse Rate		- 3.8		- 5.3		- 6.4		$\mathrm{^{\circ}K\,km^{-1}}$

stratification. The Reanalysis lapse rates in the lowest 1500 m ASL range across the 287 climate bins from - 4.5 to - 9.1 $\mathrm{K\,km^{-1}}$. The neighboring Reanalysis nodes have characteristics that vary only slightly from this one. In contrast to the Reanalysis, radiosondes indicate the long-term annual mean temperature profile is stably stratified (i.e. environmental lapse rate is more stable than the moist adiabatic rate of nominally - 6 $\mathrm{K\,km^{-1}}$), and more strongly so toward the valley bottom (700 m ASL). Furthermore far stronger valley inversions, with lapse rates of about +8 $\mathrm{K\,km^{-1}}$ and caps at around 1600 m ASL, dominate the Whitehorse climate during winter. The important control of these more stable temperature profiles on the long-term wind climate is not fully reflected in the mean annual temperature profile.

Figure 7.1 indicates that only at around 1500 m ASL are annual mean wind

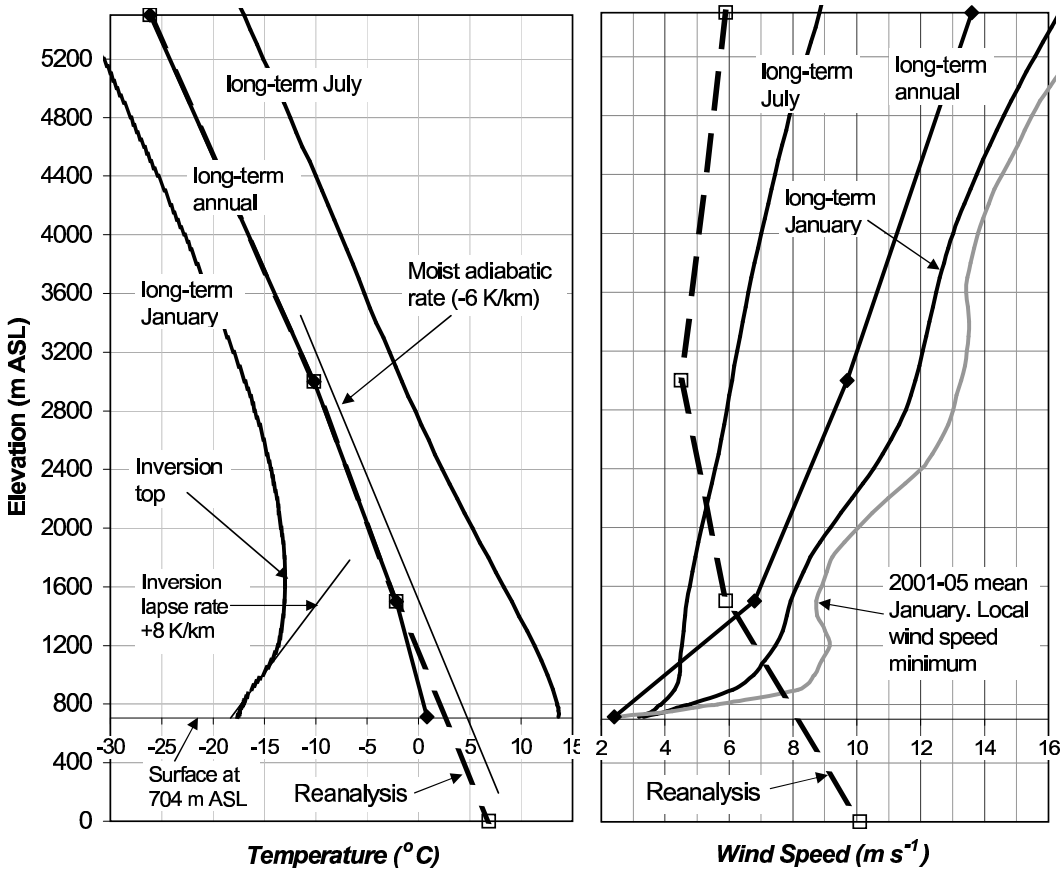

Figure 7.1: Vertical profiles of temperature and wind speed for the Reanalysis and the Whitehorse radiosondes for the 43-year, 1958-2000 period. The temperature and wind speed profiles (long-term annual mean) for the Reanalysis are represented by dashed lines.

speeds from the Reanalysis (thick dashed line) and from the Whitehorse radiosonde of similar magnitude. At higher levels radiosonde long-term annual mean wind speeds are much faster than those indicated by the Reanalysis, while conversely, at lower levels radiosonde windspeeds are slower than those of the Reanalysis, which increase towards and are fastest at sea-level (note: the high sea-level windspeed from the Reanalysis is unrealistic, and is due to neglect of the effects of friction, i.e. divergence of the Reynolds stress tensor, and of topographic steering). Evidently then, it will be inappropriate to use the sea-level wind speed of Table 7.1 as a lateral boundary condition for MC2.

The temperature lapse rates and wind speeds discussed here play an important role in the behavior of wind flow in mountainous terrain. A qualitative insight into the influence of atmospheric stability and wind speed on flow over terrain may be gained by considering the Froude number, defined

$$F = \frac{U}{NH} \ , \tag{7.1}$$

where U is mean wind speed, H the topographic amplitude, and N the Brunt-Väisälä frequency

$$N = \sqrt{\frac{|g|}{T_v}\left(\frac{\triangle T_v}{\triangle z} - \Gamma_d\right)} \tag{7.2}$$

(g the gravitational acceleration; T_v the virtual temperature; $\Gamma_d = 9.8\,\mathrm{K\,km^{-1}}$ the dry adiabatic lapse rate). The utility of F as a diagnostic stems from the fact that its square is the ratio of the kinetic energy (per unit mass) of oncoming air to the work needing to be done (per unit mass, against gravity) to ascend over the terrain: thus the magnitude of F loosely indicates the ability or tendency of air to ascend

over terrain, as opposed to deviating along valleys and over passes. In principle the lower the value of F the shallower the layer of air able to ascend over a barrier, and (correspondingly) the deeper the underlying column of cold valley air that must deviate horizontally around a mountain obstacle. This appealing interpretation is of course complicated by the fact that, in the case of real winds over real terrain, there is likely to be ambiguity in the specification of each of the factors U, H, N determining F.

In a stably stratified environment, under moderate wind conditions $F \lesssim 1$. For the annual mean conditions given in Table 7.1 the Brunt-Väisälä frequencies according to the Reanalysis and the radiosondes were respectively $N = 0.012, 0.015\ \mathrm{s}^{-1}$ while the corresponding Froude numbers were $F = 0.5, 0.4$. Season-specific values from the radiosondes were $N_{summer} = 0.01\ \mathrm{s}^{-1}$, $N_{winter} = 0.02\ \mathrm{s}^{-1}$ and $F_{summer} = 0.56$, $F_{winter} = 0.35$. Thus across all seasons the seasonal mean temperature profile is stably stratified, and valley air should be expected to have a strong tendency to move around mountain obstacles, with minimal vertical movement.

Figure 7.1 also gives the mean January wind speed profile for a shorter, more recent period 2001-05. Aside from the fact of an apparent long-term increase in wind speed in the Whitehorse region, what is noteworthy in this profile is the local minimum in windspeed that occurs at 1500 m ASL. Inset on Figure 7.3 are wind roses calculated from the Whitehorse radiosonde. At levels below 1500 m ASL the dominant wind tracks along the valley[5], this trend extending to 1600 m ASL

[5]Except at 714 m ASL, where the southerly dominant wind reflect the localized land forms; please refer to Pinard (2007) for details.

according to a mean January 2001-05 wind rose (not shown here). Above 1600 m ASL the winds gradually veer to a well defined southwesterly at 2600 m ASL. We tentatively suggest that the observed local minimum in radiosonde windspeed for this particular January period occurs at or below the level where a dividing streamline surface (Whiteman 2000) separates energetic winds aloft that are able to cross the ridges, from decoupled winds moving horizontally within the valley.

According to climatological geopotential height fields extracted directly from the NCEP/NCAR Reanalysis (website), the annual mean free winds above the mountaintops (i.e. 3000 m ASL) of the Whitehorse region are predominantly southwesterly, if they are assumed to be geostrophic. Within the valley elevations at and below 1500 m ASL the geopotential height fields imply geostrophic winds would be southerly[6], while at sea level they would be southeasterly. The wind directions from the geopotential height fields somewhat resemble those derived from the Whitehorse radiosonde[7] that are also shown in Figure 7.2 as wind-energy frequency roses. The Reanalysis wind roses as derived for use in AnemoScope (following the method in Sec. 7.3) are also shown in Figure 7.2, and summarized in Table 7.1. The Reanalysis indicates winds that are more southerly than the measurements at 3000 m ASL, but quite comparable with measurements at 1500 m ASL. At sea level the Reanalysis wind rose is dominated by east-southeasterly winds (please note: geostrophic here) whereas the measurements in the valley bottom (714 m

[6]That is, long term climatological isobars at 1500 m ASL run N-S in the Whitehorse region, with pressure increasing towards the east.

[7]Please note that the measured winds at 1500 and 714 m ASL are ageostrophic as they are controlled by the valley orientation.

ASL) follow the south-southeast orientation of the Whitehorse Valley.

Surface measurements from nearby, well exposed stations at various elevations compare well with the radiosonde. There are about 25 measurement sites in the Whitehorse region, half of them located in the valley bottoms. In Figure 7.3, most of these wind monitoring stations are shown along with their wind energy rose, ground elevation, and mean wind speed (at 30 m AGL). Details for the stations used in this study can be found in Pinard (2007); Pinard et al. (2005); Pinard (2005). Long term annual mean wind speeds at the bottom of the valleys are generally between 1 and 4 $\mathrm{m\,s^{-1}}$ (measured at 10-30 m above ground level, AGL), whereas sites on mountaintops that are open to the south and west have wind speeds between 5 and 8 $\mathrm{m\,s^{-1}}$. The wind roses of Figure 7.3 indicate two important prevailing wind directions: southwest and southeast. The stations at Flat, Watson, Jubilee, and Champagne measured southwest winds. The other stations measured south to southeasterly winds, depending on the local orography around each site.

In some locations the atmospheric stratification affects the dominant wind direction relative to the orography. At Mount Sima for example, the station is at mid-height on the west side of the Whitehorse Valley and has some orographic blocking from the southwest (see Fig. 7.3). In the summer, under rather weak stratification this station measured prevailing wind directions from the west-southwest. In the winter however, with more stably stratified conditions, the most dominant wind has been from the southeast. The Fish station to the northwest measured the same seasonal trend.

The Reanalysis climate is most strongly influenced by the nearest radiosonde, in

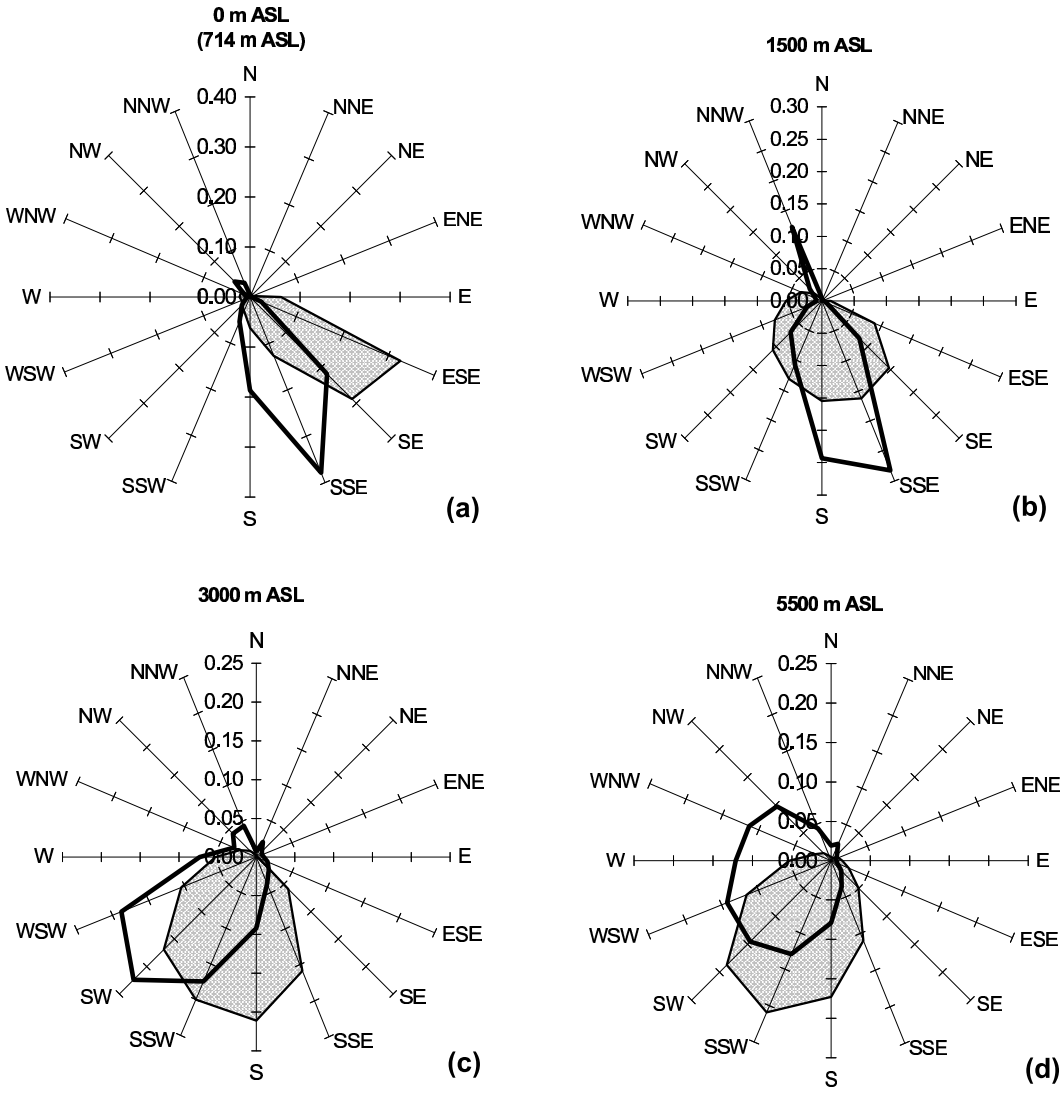

Figure 7.2: Wind energy-frequency roses comparing the Reanalysis (shaded) and the Whitehorse radiosondes (outlined) at altitudes 0 (714 only for radiosondes), 1500, 3000, and 5500 m ASL. Both analyses are for the period 1958-2000. The Reanalysis roses are from node 61/90 at the location shown in Figure 7.3 and are those used as input to the MC2 portion of the AnemoScope toolkit. The wind energy-frequency is calculated as the product of the percentage frequency and the cube of the mean wind for each direction, divided by the sum of those products in all directions.

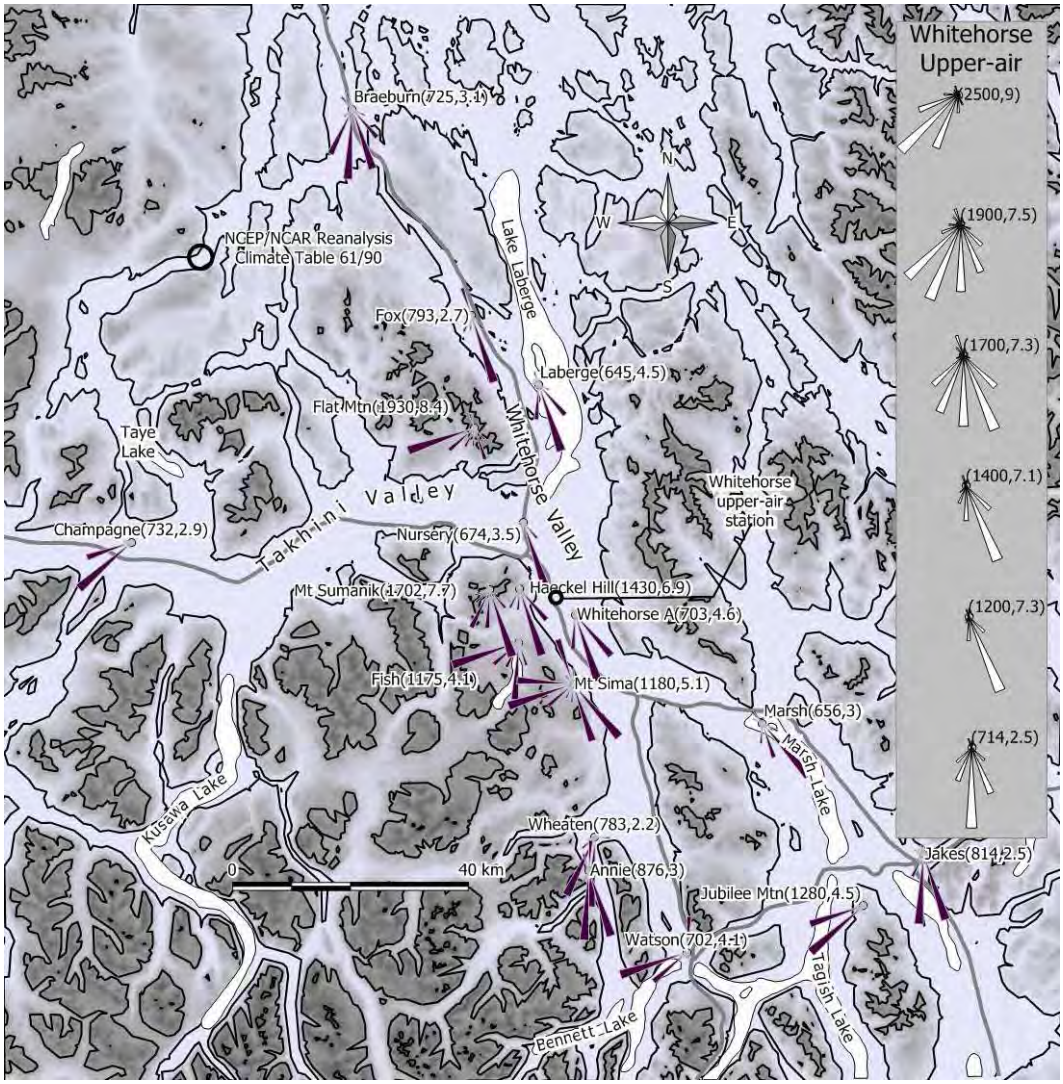

Figure 7.3: Map of the south-central Yukon including the Whitehorse area, showing contour lines at 900 m and 1500 m ASL. The roads are in gray. For present purposes two valleys are of most interest: the Whitehorse Valley and the Takhini River valley. The wind monitoring stations are shown along with their wind energy rose, surface elevation (m ASL), and mean annual wind speed (at 30 m AGL). The inset roses for Whitehorse upper-air are labelled with height (m ASL) and mean annual wind speed for the period 2001-2005. The wind energy-frequency rose is calculated, for each direction, as the product of the cube of the mean wind speed and its frequency of occurrence divided by the sum of those products in all directions.

this case the Whitehorse station (85 km southeast of node 61/90). The southeasterly low-level winds of the Reanalysis are attributable to the Whitehorse measurements having been made within this southeasterly valley. In contrast the Champagne station, 70 km west of Whitehorse, measured predominantly southwesterly winds. What would the Reanalysis look like for this region, had the radiosonde station been located at Champagne? We raise the question not in order to answer it, but simply to highlight a logical weakness of the present approach to climate input for simulating the regional wind climate.

7.5. Numerical simulations

As stated earlier, defining long term wind climate by appropriately weighting each of the MC2 solutions driven by each of the (287) distinct climate macrostates (as defined by the Reanalysis), had produced doubtful results in the mountainous regions of Whitehorse. In Pinard et al. (2005) it was not clear which of the driving climate macrostates were the dominant cause of the erroneous results. In this study we wish to simplify our simulation and so in this section we shall compare two simulated wind climates, each derived by driving MC2 with a simple, *single*, mean macroclimate:

- climate macrostate Ω_1: weighted average wind speed and temperature of the 287 Reanalysis bins and wind directions based (partly) on wind energy-frequency roses shown in Figure 7.2

- climate macrostate Ω_2: wind speed and direction taken as constant with

height, and approximately equal to the Reanalysis winds (averaged over all 287 bins) above mountain tops; temperature profile representative of winter conditions as measured by the Whitehorse radiosonde

Both simulations use the same 450 $\times$ 450 km domain with a 5 km grid resolution, and use the surface elevation and land use data from the United States Geological Survey (USGS) 1-km database (the elevated terrain is blended into a bordering sea-level flat plain at the boundaries). The parameters used for MC2 simulations are listed in Table 7.2. The vertical resolution is such that the lowest grid level (for horizontal components U, V) is 40 m above the surface (or AGL), with the next highest gridpoints at 125, 220 m AGL, and with a gradually increasing interval thereafter. The land use data are converted to surface roughness using a look-up table (see Pinard et al. 2005). Typically, the higher elevations in the land model are classified as tundra, with surface roughness z_o = 0.01 m. Valley bottoms are mainly covered in spruce forest, represented with z_o = 1.5 m. Lakes are assigned z_o = 0.001 m.

a. *Climate macrostate* Ω_1

This macrostate is defined by averaging over the 287 Reanalysis bins (Table 61/90) representing the Whitehorse area climate, and is given in Table 7.3. The (scalar) mean wind speed (and temperature) at each level is the sum of the frequency of occurrence in each bin multiplied by the associated wind speed (or temperature). The wind directions listed in Table 7.3 veer from southeast at sea level to southwest

Table 7.2: List of parameters used in the simulations of MC2.

Parameter descriptions	Values	Units
Horizontal resolution	5	km
Horizontal grid	90×90	grid cells
Height of model lid	20	km
Number of vertical levels	35	
Number of levels in 1500-m boundary layer	12	
Blending zone between mountains and flat plain	8	grid cells
Width of flat plain around model	9	grid cells
Time step	60	seconds
Total steps	960	
Total model time	16	hours
Time for mountain growth	4.2	hours
Run time on modern computer	<1	hour

at 5500 m ASL and these reflect the prevailing wind directions indicated in the wind energy roses of Figure 7.2. The veering of wind directions in this single profile is quite comparable to individual climate profiles of the most important (i.e. most frequent) bins in climate Table 61/90. As is standard procedure in Anemoscope, the sea level winds are reduced by 40% and rotated by 45° anticlockwise[8], but (please note) the surface *pressure gradient* of the Reanalysis is not altered. The temperature profile in the lowest 1500 m represents a mean temperature lapse rate of - 6.7°K km^{-1}.

The resulting MC2 simulation driven by climate macrostate Ω_1 is shown in the form of surface horizontal winds in Figure 7.4. The simulated wind vector field of

[8]In the model's low lying regions surface and orographic roughness does not adequately reduce and rotate the sea level geostrophic winds of the Reanalysis to reflect actual, or boundary layer winds. This results in a surface wind that is too fast, and that blows from a direction that is (roughly) 45 ° in error. While this adjustment has significant impact for simulation of winds over low terrain, the rotation becomes less important in mountainous regions — as will become evident.

Table 7.3: Input parameters of the climate macrostate Ω_1 representing the Reanalysis. This macrostate is used in the MC2 simulation of the Whitehorse Area.

	0 m	1500 m	3000 m	5500 m	Units
Speed	10.1 × 0.6	6.0	4.8	6.3	$\mathrm{m\,s^{-1}}$
Direction	135 - 45=90	158	180	223	$^\circ$
Temperature	279	269	262	246	$^\circ$K
Lapse Rate	- 6.7	- 4.0	- 6.4		$^\circ\mathrm{K\,km^{-1}}$

the present single MC2 run is comparable to that which results from averaging all 287 MC2 runs, one for each climate bin[9]. Along the boundaries (not shown in the figure) and on the flat plain (at 0 m ASL) surrounding the model terrain, the winds are easterly, that is, they are in conformance with the boundary condition with its rotated[10] surface wind direction (i.e. 135 - 45 = 90°).

In the central portion of the domain, within northwest-southeast oriented valleys such as the Whitehorse Valley, the simulation from macrostate Ω_1 correctly simulates southeasterly winds (compare Figures 7.3, 7.4). But the similarity with the measurements ends here. Outside of the Whitehorse Valley, the surface winds over the rest of the terrain are also dominantly southeasterly with easterly and southerly components, contradicting most of the measurements. In the Takhini Valley for example, the simulated winds are easterly (Fig. 7.4), and in some places northeasterly — in contrast with the dominant southwesterly winds measured by the Champagne surface station. On the mountaintops, the simulated winds are southeasterly, at odds

[9]Both results showed similar wind directions along the boundary, within the valleys and at the mountaintops.

[10]A second simulation was made without the 45-degree rotation of the surface winds. This simulation created southeasterly winds along the borders but had little effect on the surface winds within the model terrain. As stated earlier the angle adjustment is made after the pressure gradient is set for the initial and boundary conditions.

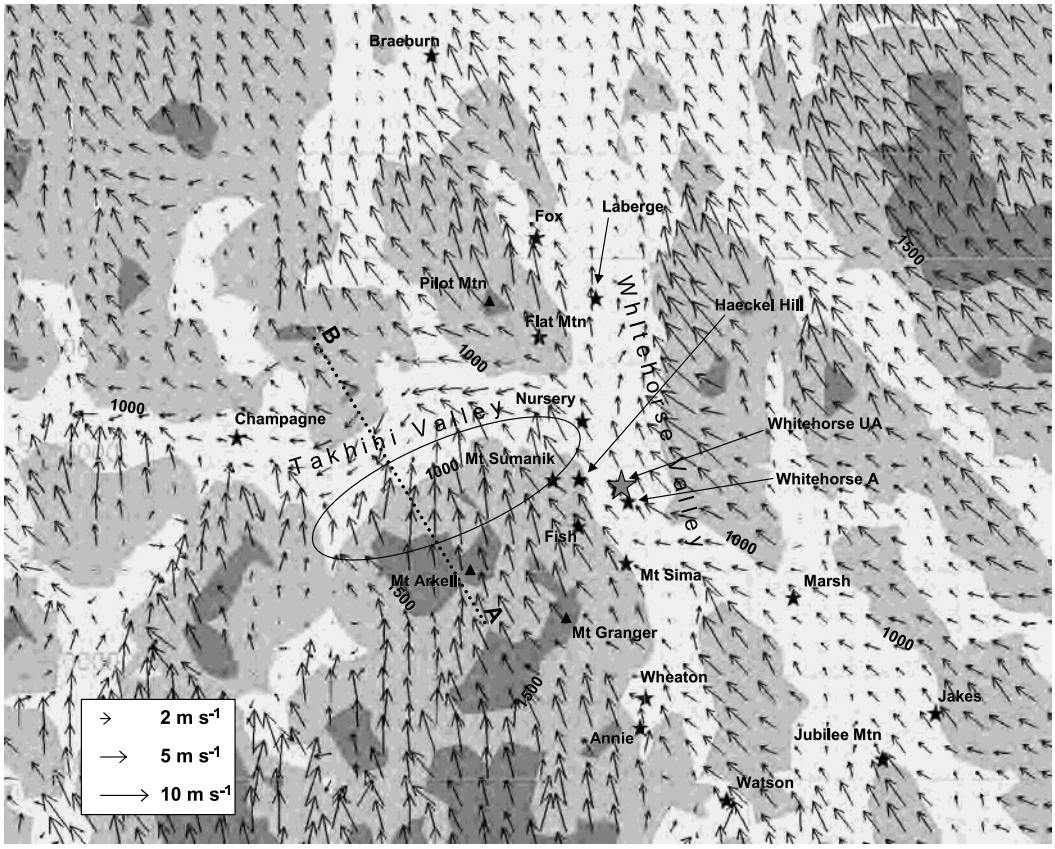

Figure 7.4: Outcome of wind climate simulation based on driving MC2 with climate macrostate Ω_1, which represents the Reanalysis. The vectors are long-term mean near-surface (40 m AGL) winds in m s^{-1}. There are two elevation contours at 1000 and 1500 m ASL.

(by some 90°) with the southwest winds measured by the Flat Mountain surface station, and the radiosonde at 1900 m ASL. One should note here that the simulated southeasterly winds at the mountaintops conform to the initial and boundary wind directions that were imposed on the simulation (as noted in Table 3), being 158 degrees at 1500 m ASL. At 700 mb in the model ($\sim$ 3000 m ASL, not shown) the simulated winds are southerly, consistent with the boundary conditions as given by the Reanalysis at the same elevation, but not consistent with the radiosondes, which measured predominant southwesterly winds.

Another important group of unrealistic modelled wind vectors that should be noted here are the strong southeasterly winds that appear on the north-facing slopes in the Takhini Valley (see oval in Fig. 7.4). These large magnitude surface winds appear from the mountaintop ($\sim$1700 m ASL) down to 800 m ASL on the lee side of the mountain. Several hundred metres below the peak these winds have speeds that are double those diagnosed at the crest. The wind flow pattern can be better visualized with a vertical cross-section of the potential temperature and vertical wind speed across the Takhini Valley. As shown in Figure 7.5, the isentropes and isotachs reveal significant sinking motion reaching a magnitude of 0.35 m s^{-1} down into the Takhini Valley, especially near the surface. However observations of the mean state of the Yukon climate (see Pinard 2007) suggest these cross-valley winds on lee slopes are unusual — winds typically flow horizontally around mountains, and there appears to be little vertical motion, especially during the winter months. These problematic strong lee-slope winds were also simulated in Pinard et al. (2005) in the deep Kluane Valley, west of Whitehorse, and these also contradicted the sur-

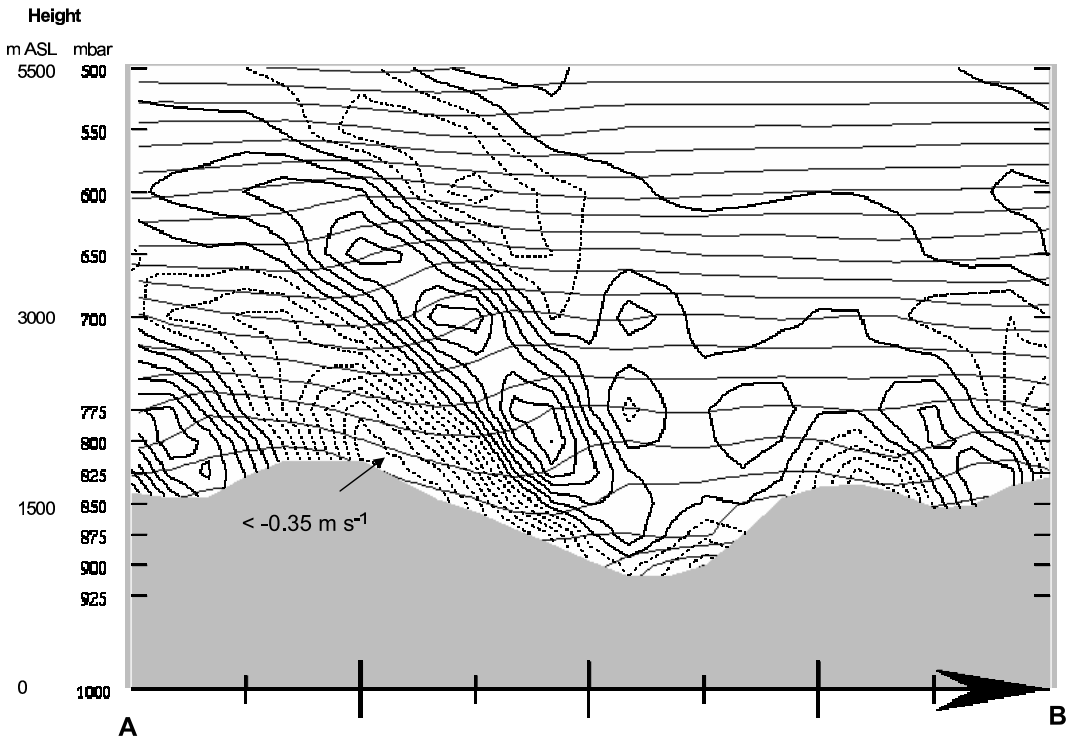

Figure 7.5: Outcome of wind climate simulation based on driving MC2 with climate macrostate Ω_1 representing the Reanalysis. Cross-section of potential temperature and vertical velocity across the Takhini Valley, line A-B in Figure 7.4. The potential temperature interval is 1 K. The vertical velocity interval is 0.05 m s^{-1} and the dashed lines are vertical velocities $\leq$ 0 m s^{-1}. In interpreting the pattern of the vertical motion, it is crucial to understand that the computed mean horizontal wind vector along this transect does not everywhere lie in the plane of this diagram; this is a complex 3-dimensional flow (refer to Fig. 7.4), not a simple uni-directional left-to-right flow.

face measurements in this valley. It had not been clear at the time which of climate macrostate was causing this problem.

How might one improve on this, the Ω_1 simulation? Ω_1 has been initialized with a southeasterly (geostrophic) wind in the lower troposphere (i.e. panel b of Fig. 7.2), in the light of which (and considering the improperly imposed easterly surface wind) the successfully simulated southeast wind in the Whitehorse Valley

is unsurprising. We note, though, that corresponding to the southeast geostrophic wind the alignment of the isobars implies the simulation must have come to an equilibrium with a pressure gradient oriented SW-NE, i.e. with higher pressure to the northeast (which is, in fact, the case in the simulation). Since the Takhini Valley is oriented west-east, it is reasonable to infer that this background macroscopic pressure gradient has driven the (simulated, and false) easterly winds in that valley, winds whose orientation is at odds with the wind direction seen in measurements. If the background pressure gradient were rotated so that higher pressure lay to the southeast, one would then expect southeast ageostrophic winds in the Whitehorse Valley, but the corresponding southwesterly geostrophic wind in the lower troposphere would be compatible with observations aloft. It also seems advisable to reduce or eliminate the noted spurious "downward mixing" associated with the Ω_1 macrostate, for which N = 0.01 s^{-1} and F = 0.6, assuming a characteristic mountain height of 1000 m and wind speed of 6 m s^{-1}. The effective Froude Number can be reduced by strengthening the stratification (increasing N), which should reduce the downward transfer of momentum into the valleys.

In view of the above-noted problems with the MC2 wind simulation when driven by climate macrostate Ω_1, in the following section we introduce driving macroclimate Ω_2 which results in an improved agreement of the modelled and observed wind climates.

b. *Climate macrostate* Ω_2

Although the Reanalysis indicates that at lower elevations ($\leq$ 1500 m ASL) the "geostrophic" sea level winds are from southeast, let us instead assume that the low level geostrophic winds are aligned with the southwest winds that occur above the mountaintops - in effect, we consider the Reanalysis data for the air aloft to be more reliable than that for the layer between mountain top and sea level. For simplicity, let us also define a height-independent wind speed that is comparable to that of the Reanalysis above the mountaintops. The lower boundary layer attenuation and rotation of the wind vector are not applied in this simulation. See Table 7.4 for the proposed climate macrostate Ω_2.

As noted earlier, to suppress the vertical movement of air into the valleys, the temperature stratification is strengthened. Since the bulk of wind energy production is in the winter, we adopt a stability condition that is representative of winter. The wintertime lapse rate (from the radiosondes) within the Whitehorse Valley is +8 $\mathrm{K\,km^{-1}}$: the temperature profile for the Ω_2 input is set to reflect this winter condition. This temperature profile results in N = 0.026 $\mathrm{s^{-1}}$, and F = 0.2 (U = 5 m $\mathrm{s^{-1}}$). Variants of Ω_2 have also been investigated, and these results will also be discussed.

With the climate macrostate Ω_2 adopted to define the boundary conditions, the resulting MC2 simulation produces flow directions that generally conform better with measurements at many locations. A first glance at Figure 7.6 shows that the mountaintop winds blow mainly from the southwest, conforming with the boundary conditions. These mountaintop vectors line up with the measurements at Flat

Table 7.4: Input parameters of the climate macrostate Ω_2 used in the MC2 simulation of the Whitehorse area.

Variable	0 m	1500 m	3000 m	5500 m	Units
Wind Speed	5	5	5	5	$\mathrm{m\,s^{-1}}$
Wind Direction	225	225	225	225	
Temperature	261	273	285	285	°K
Lapse Rate	8	8	0		$^{\circ}\mathrm{K\,km^{-1}}$

Mountain and the Whitehorse radiosondes at 1900 m ASL (see Fig. 7.3). To the south of the Champagne site the wind vectors also show southwest winds from an open valley as is expected at this location. At the grid point nearest Champagne, however, the simulation provides an erroneous northwest wind: winds in the Takhini River valley at Champagne are expected to be from west-southwest to southwest. At the two Whitehorse surface stations the simulated valley-bottom flow is generally southeast conforming to surface measurements and the valley orientation. This is expected as this simulation was purposely set up with the higher pressure to the southeast, so that within the Whitehorse valley the flow is pressure-driven from that direction.

The more important purpose of this exercise has been to prevent downward momentum transfer by inducing strong stratification (ie. F = 0.2) into the MC2 model. This is to allow a pressure-driven flow within the valley to occur uninhibited by the vertical transfers from the winds aloft when there is an orographic blocking. While the Ω_1 simulation, with rather weak stratification, allowed too much downward momentum transfer with the consequence that large magnitude winds reach far down the lee slopes, the Ω_2 state appears to have suppressed this, albeit only

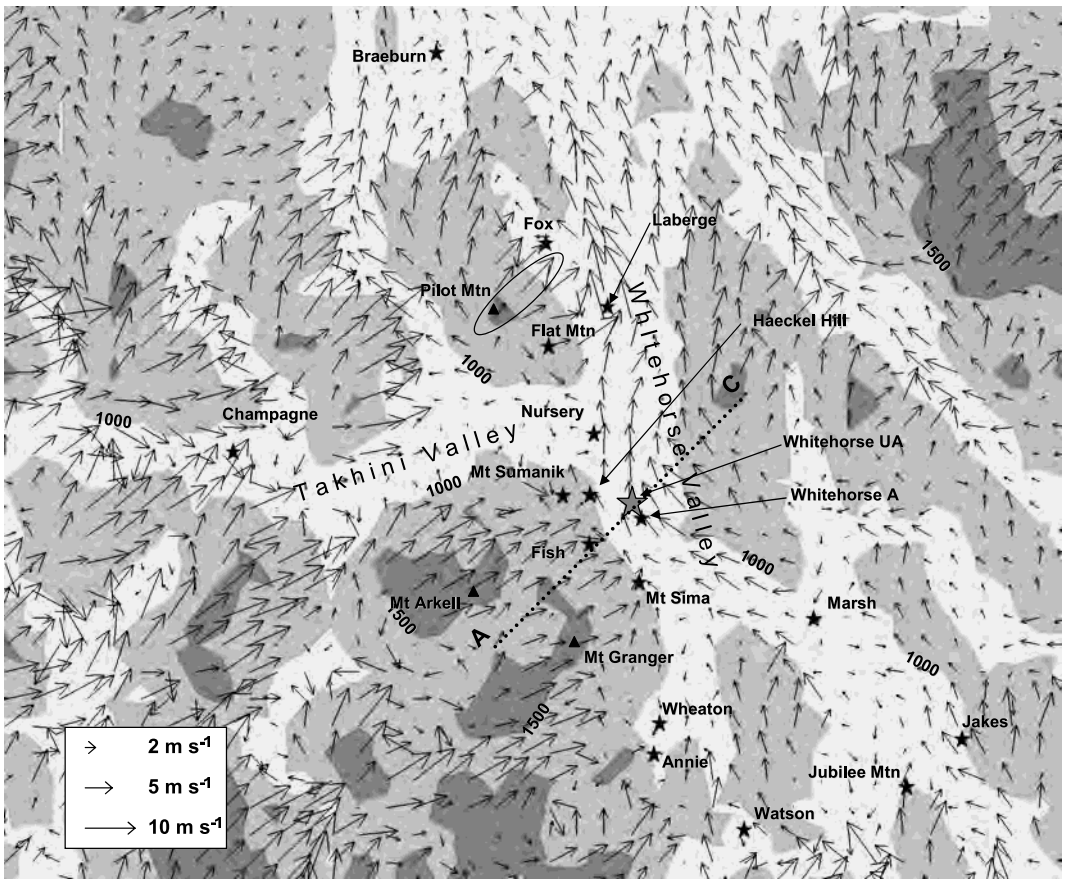

Figure 7.6: Same as Figure 7.4 but for climate macrostate Ω_2.

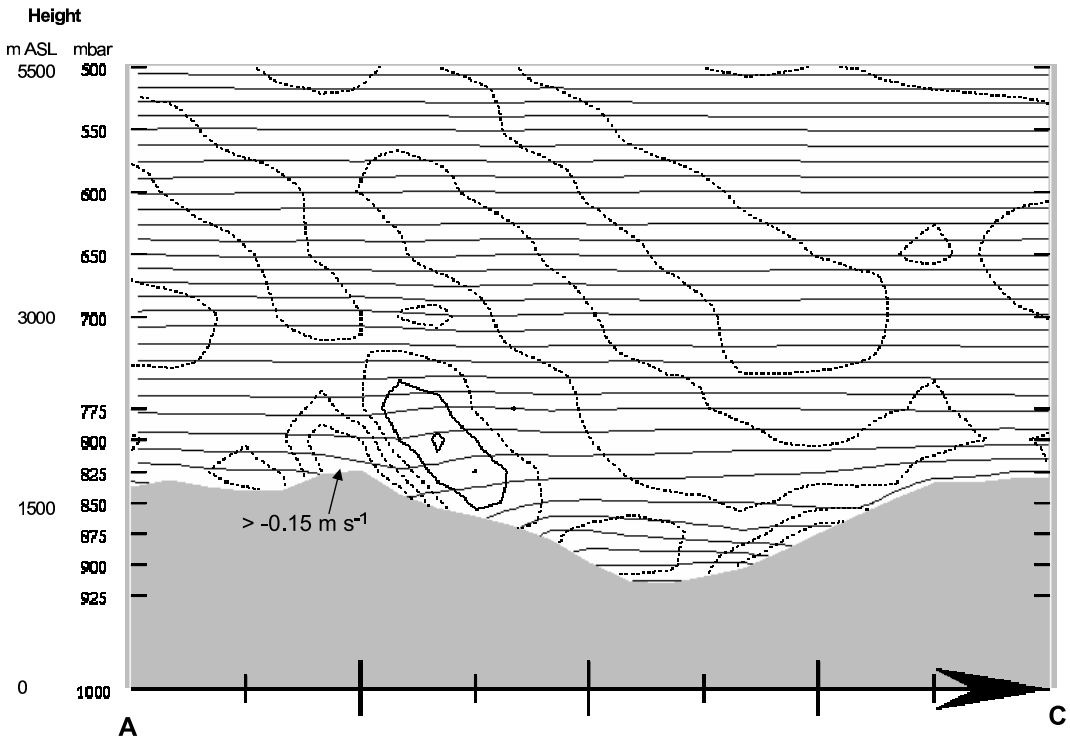

Figure 7.7: Same as Figure 7.5 but but for climate macrostate Ω_2 and across the Whitehorse Valley, line A-C in Figure 7.6. The potential temperature interval is 2 K. The vertical velocity interval is 0.05 m s^{-1}.

marginally. This suppression of downward wind is evident in Figure 7.7, which shows that the isentropes across the Whitehorse Valley (line A-C in Fig. 7.6) are relatively level and undisturbed by the mountains. The isotachs show that the downdraft does not exceed 0.15 m s^{-1}, which is an improvement over the Ω_1 simulation. The Ω_2 macrostate was also simulated with same weak stratification as Ω_1 and the downward vertical motion in this same cross-section exceeded 0.2 m s^{-1} and was present all the way down the lee slope, contrary to Figure 7.7. In summary Figure 7.7 indicates that there should be no significant downward momentum transfer and hence there should be no high winds on leeward slopes.

But despite the deep, strong inversion and low Froude number (F = 0.2) in the

Ω_2 simulation, there are still excessively large magnitude winds on the lee slope of mountains. For example, the surface wind speed at the peak of Pilot Mountain (see oval in Fig. 7.6) is 3.5 m s^{-1} while at the next downstream node, which is 300 m lower, it is 8.7 m s^{-1} (w $\approx$ -0.5 m s^{-1}) along the same direction. This scenario of strong discrepancy in wind speed also occurred when simulated with the same Ω_2 macrostate but with lower boundary winds of 2 m s^{-1} (ie. F = 0.08).

The massifs of Mount Arkell and Mount Granger shown in Figure 7.6 act as a barrier against the southwest winds aloft and on the plateau in the lee of this range, the surface winds ought to follow along the Whitehorse Valley axis as the measurements indicate (under wintertime conditions). In the simulation however, many of the surface nodes on this plateau are southwesterly. On Mt Sumanik and Haeckel Hill for example, the surface wind directions at those nodes are unorganized while measurements show clear evidence of the south-southeast winds. At the Fish station (as well as Mt Sima) the measured winds were southerly (southeasterly) under wintertime stratification but the nearest node simulated westerly winds.

To further investigate this problem a cross-section of the Whitehorse Valley with vertical profiles of horizontal wind speed is presented in Figure 7.8. The cross-section runs southwest to northeast across the valley (along line A-C in Fig. 7.6) and follows the southwest wind direction in the model. There are several features that are apparent here and that will be addressed, starting from the upper levels. Firstly we note that above the mountaintops (>2000 m ASL) the wind speed is generally over 6 m s^{-1} — a speed-up that is over 20% higher than the imposed boundary wind speed of 5 m s^{-1}. Above the first range of mountains where nodes

1 to 4 are located there are two local wind speed maxima, or jets. The upper jet (at 4000 m ASL over node 1) is above the dashed line and appears to be a gravity wave responding to orographic disturbance. Following Pinty et al. (1995) the hydrostatic vertical wavelength $\lambda_H = 2\pi\overline{U}/N$ = 1.5 km (where $\overline{U}$ = 6 m s^{-1} and N = 0.026 s^{-1})[11]. This is roughly equivalent to the vertical distance between the lower and upper jet above nodes 1 to 4 and is consistent with the gravity waves produced in Pinty et al. Over nodes 3 to 5 the nose of the upper jet appears to follow the terrain-following grid, along the dashed line. Note, however, that below 3000 m ASL the atmosphere is highly stable, which might be expected to suppress vertical momentum transport. The lower jet near the surface over the first range follows the dotted line in Figure 7.8, and appears to be a localized hill speed-up. At node 3 the elevation of the jet has dropped relative to sea level, but is at nearly the same height above the surface as it is at nodes 2 and 4. The lower jet disappears as the flow goes past node 5 on the downslope side of the first range.

At node 6, where the ground surface lies fully 600 m below the crest of node 4, the surface wind has swung to a southeasterly, following the valley (see Fig. 7.6 along line A-C). At node 6, moving up from the surface, the wind speed decreases to a local minimum not very far above ground, only to increase sharply at still higher elevations. This local minimum also appears at the nodes downstream from node 6, and is associated with a sharp veering of the wind direction and hence a separation surface, or a dividing streamline height. A thick solid line on Figure 7.8 delineates a

[11] $\overline{U}$ is the ensemble mean wind speed above this area, and the Brunt-Väisälä frequency N is calculated from the initial conditions for Ω_2

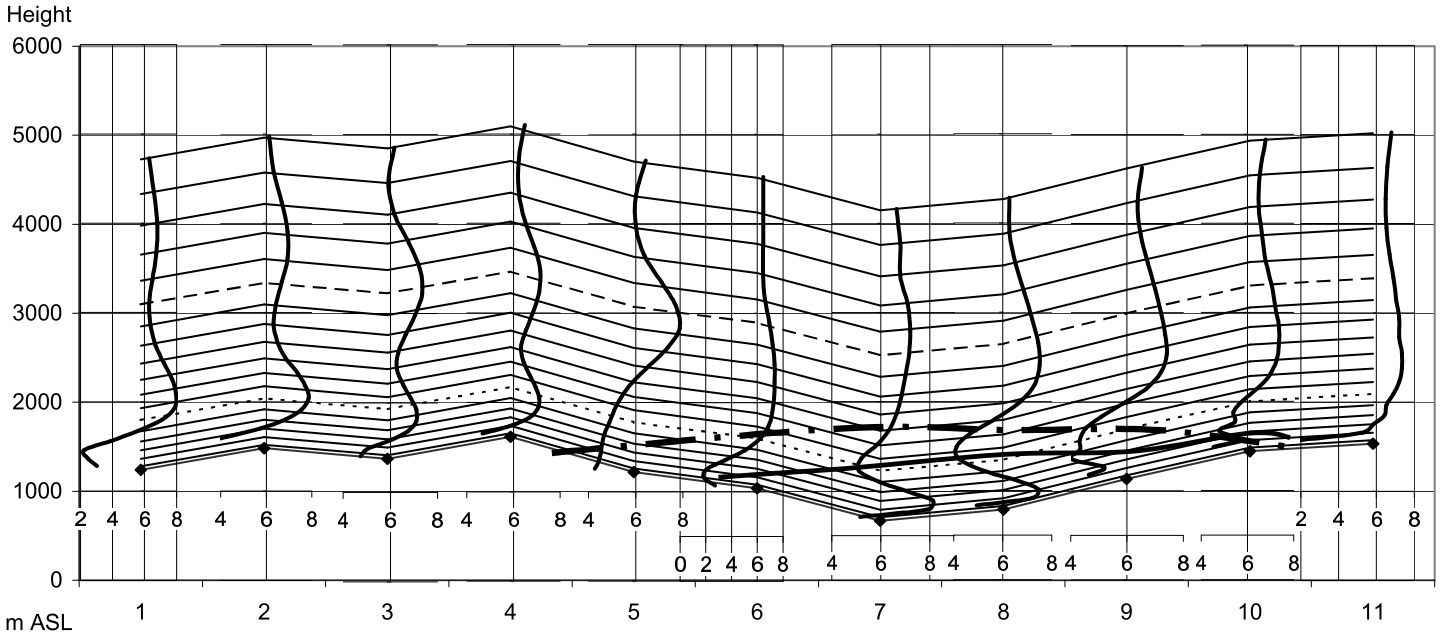

Figure 7.8: Cross-section of the Whitehorse Valley running southwest to northeast, following the southwest wind direction of the Ω_2 state simulation. The abscissa corresponds to the mesoscale grid points along baseline A-C indicated in Figure 7.5. These vertical profiles of horizontal wind speed flow from the southwest ($\pm$ 10 $^\circ$), except within the valley under the thick solid line delineating a dome of dividing streamline. Each profile is centered at 6 m s^{-1} through each of nodes 1 to 11. The vertical exaggeration is five times. The spacing between the nodes is 7.1 km (diagonal across 5-km square grid) and the heights of the lowest grid levels are 40, 125, 220, and 320 m AGL and increase gradually thereafter. The grid levels that are represented by a dotted and a dashed line are at levels 560 and 1860 m above the model surface respectively and are for reference in the text discussion.

dome, whose position identifies the height at which the dividing streamline occurs. Above the dome the wind is southwesterly, and below the wind direction is mostly south-southeasterly, following the valley. Within the dome a jet having a nose at a maximum height of 220 m (third level above node 7 and 8) above the surface is a dominant feature. Most interesting is the shape of the dome: the dome appears to be pushed up the northeast side of the valley, onto the next ridge. It would appear that the southwest wind aloft is pushing the dome up against the other side of the valley. When the simulation was repeated with a weakened stratification, the asymmetry of the dome of cold air was more marked.

Focussing our attention back to the measurements, the Whitehorse upper-air station is located near node 7, at the valley bottom, where the nose of the measured winter jet (500 m AGL) is twice the height of the simulated one (220 m AGL). From the radiosondes (see Fig. 7.3) the wind direction changes from a valley wind to a southwesterly wind at about 1700-1900 m ASL (or 1000-1200 m above the valley bottom). In the simulation, especially under a strong winter stratification, we should therefore expect that the dome of dividing streamline height should be about 1100 m above node 7 (1800 m ASL), double the height of the dome of dividing streamline height that has been simulated. Strengthening this argument, Mt Sumanik and Haeckel Hill are located near node 6 and at surface heights of 1430 and 1701 m ASL respectively. Both surface stations measured dominantly south-southeast winds (year-round, even under weaker stratification) and this would suggest that the height of the dome at node 6 ought to be at least 1000 m above the valley bottom (1700 m ASL). A suggested shape for this dome of dividing stream-

line (that is, the dividing surface as defined by measurements as opposed to by the simulation) is shown as a thick dash-dotted line in Figure 7.8.

In concluding the discussion of Figure 7.8 we remark that although the inversion height (being 1500 m higher than measured) and its intensity (typical winter lapse rate) were exaggerated in the model, the wind following the Whitehorse valley did not "fill" the valley as the measurements suggest.

7.6. Discussion

The problems arising from the Ω_2 simulation have also appeared in comparable studies simulating valley flows with cross-winds aloft. Both Bergström and Juuso (2006) and Gross and Wippermann (1987) simulated valley jets that were concentrated on the downwind side of a valley relative to the crossing wind aloft and under relatively stable conditions. Vogel et al. (1986) also carried out simulations that showed channelling with a jet maximum very close to the valley bottom and away (downstream towards the east side of the valley) from the main flow aloft in the Upper-Rhine Valley. But according to Vogel et al., when the measured wind aloft was from the west crossing the Upper-Rhine Valley the observed channelling could be found on the west side of the valley, opposite to their simulated valley wind. This was observed in a field experiment (Fiedler and Prenosil 1980) where nine weather balloon stations were placed across the Upper-Rhine Valley. As the wind aloft increased, a valley jet intensified towards the middle (horizontally and vertically) of the valley and channelling spread widely and evenly across the valley. Vogel et al. also showed that the valley channelling could reach hundreds of

metres above the mountaintops bordering the valley, on a typical September day (our calculations from their study showed, surprisingly, that $F \simeq 1.5 - 2$). Vogel et al. have shown, and this is also being demonstrated in the present study, that the simulated valley wind stream is pushed further downward and downstream relative to the wind aloft than the measurements of the same circumstance suggest.

One of the features the above models have in common with MC2 is that they use a terrain-following (or σ-) coordinate system. The coordinate transformation splits the horizontal pressure gradient into a sum of two terms, one of which involves the *vertical* pressure gradient. Near steep slopes these terms become large and a small error in computing either term can result in a large error in the total pressure gradient force (Haney 1991). Janjic (1989) tested a σ-coordinate system with a single mountain in the middle of a horizontally homogenous atmosphere at rest. The study found significant errors in the pressure gradient force that corresponded with the presence of an imposed temperature inversion. These errors were, however, restricted to points over the sloping terrain.

These errors had been less serious in low resolution modelling studies which are provided a highly smoothed topographic field. However as the grid is refined there occur regions of (locally) steep slope, such that the slope-induced errors in the representation of the horizontal pressure gradient can no longer be ignored (see Mesinger 2003, for thorough discussion). Steppeler et al. (2002) notes that for better accuracy in terrain-following coordinates one should require $\delta h < \delta z$, where δh is the change of orographic height from one horizontal grid point to the next, and δz is the vertical grid interval. Whereas in the Whitehorse domain δz = 40, 85,

and 95 m in the lowest three grid cells, δh can reach values that exceed 500 m on the steeper slopes such those at Pilot Mountain. Walko et al. (1995) suggests a rule of thumb that δh should not exceed 3 to 5 times δz, a criterion that, in the present simulations, has been violated on many slopes on the Whitehorse domain.

For finer horizontal grids Steppeler et al. (2002) proposed a z-coordinate system with an approximate finite-volume technique at the orographic boundary. Steppeler et al. (2006) tested this with measurable success in simulations of rain in the steep mountains of Europe. Although their focus was on predicting precipitation they found reduced velocity errors near mountain slopes when compared to the terrain-following system. Even though they were satisfied with the simulated mountain-lee winds compared to terrain-following simulations, they could not confirm the results due to lack of stations in the domain of interest.

The discussions above and those based on Figure 7.8 hint that when simulating at high resolution regions of steep terrain such as the Yukon, accuracy is limited by the use of the terrain-following coordinate. To progress, one might need to revert to a basic z-coordinate system. A proposed method for MC2 is a grid cell blocking approach to implement the lower boundary condition to the 3D flow around obstacles. This is currently being tested in experimental versions of the MC2 model (P. Pellerin, private communication). Eventually, this scheme will need to be tested (as here against measurements) to check whether it represents a further improvement of the AnemoScope method in complex terrain.

Based on the present study, can one attempt to generalize the main findings to eventually improve AnemoScope and future versions of the Canadian Wind Atlas?

To a limited degree, yes:

a) Only Reanalysis data from levels well above the mountaintops should be used to initialize the EOLE mode of MC2;

b) An option of having the topography of interest (when using MC2 in EOLE mode) surrounded by a high plain, in lieu of the *sea-level* plain currently used, would be useful;

c) Care must be taken in selecting the representative temperature profile, at least in the lower atmosphere, due to the large effect of stratification on the resulting airflow;

d) Assuming that the low-level stratification in the Reanalysis data is representative of that measured by the radiosondes, then one should modify the classification scheme used to define the climate macroscopic states such that the binning be based on the geostrophic wind vector (as before) and the strength of the thermal stratification, maybe in the form of a Froude number. This last parameter could replace (or be combined with) the "sign of the geostrophic wind shear" currently used.

7.7. Conclusions

Two simplified climate states were simulated using the MC2 mesoscale model in the steep mountainous terrain of the Whitehorse area. The first climate state representing the Reanalysis was shown to result in erroneous wind directions in all but

the Whitehorse Valley where the upper-air station is located. This was primarily due to the (wrong) assumption that the winds within the domain of the orographic influences are geostrophic and were incorrectly used to set the pressure gradients in the model.

A better simulation resulted when using (as boundary condition) a height constant "geostrophic" wind speed and direction that is associated with the Reanalysis (and Whitehorse radiosondes) above the mountaintops. In this case the wind vectors conformed better with observations. In conjunction with this step an attempt to reduce the downward momentum transfer was made by adjusting the temperature profile to a highly stable state that is typical of wintertime conditions. Despite the imposed stratification there remained substantially high magnitude winds on the steep mountain lee slopes that are suspected to be caused by errors due to a terrain-following grid structure.

To improve upon the MC2 simulation in deep mountainous terrain the main recommendations are: to consider a basic z-coordinate grid for the model; to reprocess the NCEP/NCAR Reanalysis by ignoring the statistics that are affected by the orography and project down geostrophic winds from aloft; and, to put more care into temperature profile selection in the lower atmosphere.

Bibliography

Bergström, H. and N. Juuso, 2006: A study of valley winds using the MIUU mesoscale model. *Wind Energy*, **9**, 109–129.

CHC&EC, 2006: *Anemoscope Wind Energy Simulation and Mapping User's Guide*. Canadian Hydraulics Centre and Environment Canada.

Fiedler, F. and T. Prenosil, 1980: Das MESOKLIP-experiment, mesoskaliges klimaprogramm in oberrheintal. Technical report, 107 pp.

Frey-Buness, A., D. Heimann, and R. Sausen, 1995: A statistical-dynamical downscaling procedure for global climate simulation. *Thoer. Appl. Climatol.*, **50**, 117–131.

Girard, C., R. Benoit, and M. Desgagné, 2005: Finescale topography and the MC2 dynamics kernel. *Mon. Wea. Rev.*, **133**, 1463–1477.

Gross, G. and F. Wippermann, 1987: Channeling and countercurrent in the upper Rhine Valley: Numerical simulations. *J. Climate Appl. Meteor.*, **26**, 1293–1304.

Haney, R. L., 1991: On the pressure gradient force over steep topography in sigma coordinate ocean models. *Journal of Physical Oceanography*, **21**, 610–619.

Janjic, Z. I., 1989: On the pressure gradient force error in σ-coordinate spectral models. *Monthly Weather Review*, **117**, 2285–2292.

Kalnay, E., M. Kanamitsu, R. Kistler, W. Collins, D. Deaven, L. Gandin, M. Iredell, S. Saha, G. White, J. Woollen, Y. Zhu, A. Leetmaa, R. Reynolds, M. Chelliah, W. Ebisuzaki, W. Higgins, J. Janowiak, K. C. Mo, C. Ropelewski, J. Wang, R. Jenne, and D. Joseph, 1996: The NCEP/NCAR 40-year Reanalysis project. *BAMS*, **77**, 437–471.

Mesinger, F.: 2003, The steepness limit to validity of approximation to pressure gradient force: Any signs of an impact. *AMS Conference Publication*.

Pinard, J. D. J.-P., R. Benoit, and W. Yu, 2005: A WEST wind climate simulation of the mountainous Yukon. *Atmosphere-Ocean*, **43**, 259–282.

Pinard, J.-P.: 2005, Wind climate of the mountainous Yukon. *New Northern Lights: Graduate Research on Circumpolar Studies from the University of Alberta*, Canadian Circumpolar Institute.

Pinard, J.-P., 2007: Wind climate of the Whitehorse Area. *Arctic*, **60**, 227–237.

Pinty, J.-P., R. Benoit, E. Richard, and R. Laprise, 1995: Simple tests of a semi-implicit semi-lagrangian model on 2D mountain wave problems. *Mon. Wea. Rev.*, **123**, 3042–3058.

Smedman, A.-S. and H. Bergström, 1995: An experimental study of stably stratified flow in the lee of high mountains. *Monthly Weather Review*, 2319–2333.

Steppeler, J., H. W. Bitzer, Z. Janjic, U. Sch attler, P. Prohl, U. Gjertsen, L. Torrisi, J. Parfinievicz, E. Avgoustoglou, and U. Damrath, 2006: Prediction of clouds and rain using a z-coordinate nonhydrostatic model. *Monthly Weather Review*, **134**, 3625–3643.

Steppeler, J., H. W. Bitzer, M. Minotte, and L. Bonaventura, 2002: Nonhydrostatic atmospheric modeling using a z-coordinate representation. *Monthly Weather Review*, **130**, 2143–2149.

Tanguay, M., A. Robert, and R. Laprise, 1990: A semi-implicit semi-lagrangian fully compressible regional forecast model. *Mon. Wea. Rev.*, **118**, 1970–1980.

Thomas, S., C. Girard, R. Benoit, M. Desgagne, and P. Pellerin, 1998: A new adiabatic kernel for the MC2 model. *Atmosphere-Ocean*, **36**, 241–270.

Vogel, B., G. Gross, and F. Wippermann, 1986: MESOKLIP (first special observation period): Observations and numerical simulation a comparison. *Boundary-Layer Meteorology*, **35**, 83–102.

Walko, R. L., C. J. Tremback, and R. F. A. Hertenstein, 1995: RAMS the regional atmospheric modeling system, version 3b, user's guide. Technical report, ASTER Division, Mission Research Corporation, Fort Collins, CO.

Walmsley, J., D. Woolridge, and J. Salmon, 1990: MS-micro/3 user's guide. Technical Report ARD-90-008, Atmospheric Environment Services, 85 pp.

Whiteman, C. D., 2000: *Mountain Meteorology*. Oxford University Press.

Yu, W., R. Benoit, C. Girard, A. Glazer, D. Lemarquis, J. R. Salmon, and J.-P. Pinard, 2006: Wind energy simulation toolkit (WEST): A wind mapping system for use by the wind-energy industry. *Wind Engineering*, **30**, 15–33.

Chapter 8

Discussion and Conclusions

The work presented here has been done primarily to advance knowledge of mountain wind climate for wind energy prospecting purposes. The second goal for this thesis has been to visualize and quantify (ie. to map) the wind climate of the Yukon's mountainous terrain, through numerical modelling. This has involved the analysis of wind field measurements from both surface and upper-air stations in the southern Yukon, the carrying out of simulations using the mesoscale model MC2, and comparison of the simulated wind fields with the measurements.

When first applied (see Chapter 5), the MC2 simulations produced spurious wind directions and excessive wind speeds. It was speculated that the cause might be misrepresentation (flattening) of the terrain by the coarse 5-km grid, and the resulting smooth surface roughness over the ice fields next to the Kluane Lake area. There were also abnormally high sea-level winds in the Reanalysis data used as input to drive MC2, and this was also identified as factor contributing to the over-speeding in the model. As a result of this study, RPN made an adjustment to their model by reducing the speed and rotating the direction of the input sea-level wind.

In Chapter 6 I made a thorough investigation of the Whitehorse region's surface station measurements and the radiosondes, in an attempt to identify what factors controlled the wind climate of the Whitehorse mountainous region. Some of the major findings that I identified were:

- The dominant southwest winds above the Whitehorse area's mountaintops are quasi-geostrophic. They were parallel to the mean pressure contours (from geopotential height maps), where the higher pressure (or height) lay to the

southeast

- When the winds aloft were perpendicular to the Whitehorse valley, the winds within the valley were clearly correlated with the pressure gradient identified from aloft

- Responding to pressure gradient, the valley winds are channelled by deep-valley walls and are ageostrophic: orographic forcing disturbs (or prohibits) geostrophic balance

- Although the dominant Whitehorse Valley winds were parallel to those of the NCEP/NCAR Reanalysis at comparable elevations, the measured winds in the valley were ageostrophic whereas those of the Reanalysis were considered geostrophic (by RPN in the Anemoscope toolkit and the Canadian wind atlas)

- When the winds aloft flowed parallel to the valley, this was associated with a valley wind that flowed along the same direction. In this scenario the dominant forcing mechanisms were downward momentum transport and forced channelling

- Deep valleys that provide sufficient orographic blocking combined with strong atmospheric stability and moderate wind speeds decouple or separate the valley winds from those aloft

- In the Whitehorse Valley the elevation of the dividing streamline in the winter, and most of the summer, is typically near the mountaintops. That is, orography plays a significant role in separation valley winds from those aloft.

- In the Whitehorse Valley the winds respond more strongly to pressure gradient. Under strong wintertime inversions a low-level jet or a gap wind will form and its maximum speed will be at about mid-height within the valley. Low-level jets also occur in the summer but they are typically lower in the valley

Based on the findings above it is evident that the Reanalysis data set used as input to the MC2 model provides problematic "geostrophic" wind directions at elevations below the mountaintops. MC2 boundary conditions require "geostrophic" winds throughout the vertical in order to establish the pressure fields. The Reanalysis, and the radiosondes, do not provide geostrophic winds below the mountaintops. At these lower elevations the geostrophic wind information for MC2 must then come from somewhere else. Based on my findings regarding pressure-driven valley flows, my recommendation is that the geostrophic winds must be projected down from fields above the mountaintops.

In the new MC2 simulations (Chapter 7) I set the lower geostrophic winds parallel and scaled to those above the mountaintops, and imposed a wintertime temperature lapse rate to reduce downward momentum transfer. This resulted in much better agreement in the wind directions between the new MC2 simulation and the measurements. However I noted that despite the imposed strong temperature inversion, the dividing streamline was too far down in the valley. I suggested that this error could be due to numerical errors associated with a terrain-following coordinate system. There was general consent by the RPN group (Dr. Robert Benoit, pers.

comm.) that this is a real possibility and this is presently being addressed in a new version of MC2.

In concluding this thesis it is clear that pressure gradient, and atmospheric stability play an important role in the wind climate of steep mountainous terrain. Mesoscale models such as MC2 show an ability to recreate some of the measured wind climate. However, when investigating the vertical structure of the winds in the model it is apparent that the model MC2 has some difficulty in simulating a horizontally stratified wind structure as the measurements suggest exists. MC2 will therefore require some further modifications before it can be reliably used to map the winds of the mountainous Yukon (and BC). The input climate tables from the Reanalysis must be re-synthesized to exclude the statistics at lower elevation that are considered affected by orography, that is, that are ageostrophic. I suggest that the terrain-following grid be changed to a z-coordinate system to reduce the possibility of numerical errors caused by steep terrain. With the new coordinate system, the temperature profiles as extracted from the Reanalysis may be appropriate as they are. Under the above modification it will be very worthwhile to (again) test MC2 in the Whitehorse terrain.